Universiteit Gent
Faculteit Wetenschappen
Vakgroep Anorganische en Fysische Chemie

Vorming van Overvloedig Aanwezig CZTS Absorptie Lagen voor Dunne Film Zonnecellen, een Nanokristal Aanpak

Formation of Earth Abundant CZTS Absorber Layers for Thin Film Photovoltaics, a Nanocrystal Approach

---

Stijn Flamée

Proefschrift tot het bekomen van de graad van
Doctor in de Wetenschappen:
Chemie
Academiejaar 2014-2015

Universiteit Gent
Faculteit Wetenschappen
Vakgroep Anorganische en Fysische Chemie

Promotoren: Prof. Dr. Ir. Zeger Hens
Dr. Ir. Dirk Van Genechten

Voorzitter: Prof. Dr. José Martins
Leescommissie: Prof. Dr. Isabel Van Driessche
Dr. Johan Paul
Prof. Dr. Phillip Dale

Universiteit Gent
Faculteit Wetenschappen

Vakgroep Anorgansiche en Fysische Chemie
Krijgslaan 281 Gebouw S3, B-9000 Gent, België

Tel.: +32-9-2644446
Fax.: +32-9-2644983

Dit werk kwam tot stand in het kader van een Baekeland Beurs van het IWT-Vlaanderen (Instituut voor de aanmoediging van Innovatie door Wetenschap en Technologie in Vlaanderen) in samenwerking met Umicore België.

Proefschrift tot het behalen van de graad van
Doctor in de Wetenschappen:
Chemie
Academiejaar 2014-2015

Dankwoord

Na bijna 10 jaar aan de universiteit, waarvan 4,5 jaar doctoreren, ben ik er eindelijk geraakt! Het is een hele belevenis geweest en een ongelofelijke ervaring! Ik heb tijdens het onderzoek van mijn doctroraat natuurlijk veel hulp gehad van een hele hoop mensen, niet enkel wetenschappelijk, maar ook op een persoonlijk vlak, allemaal met een belangrijke bijdrage, tijd voor een bedankje!

Eerst en vooral bedank ik mijn promotor, Zeger, zonder wie ik deze kans niet had kunnen grijpen. Je verschafte me een ongelofelijke hoeveelheid aan kennis, alle nodige voorzieningen en de unieke ervaring. Van mij krijg je eindeloos respect voor de manier waarop je je baan als professor aanpakt, iets waarvan ik weet dat het er weinigen zouden evenaren. Natuurlijk bedank ik ook Dirk, mijn copromotor, die me de kans gegeven heeft om mijn project in samenwerking met Umicore te kunnen schrijven en te vervolledigen. Hierdoor kreeg ik een zeer goed inzicht in de werking van industriëel onderzoek en dat was in mijn opzicht een onmisbare ervaring. Het was een verrijking om verschillende inzichten en een andere invalshoek te krijgen op het doctoraatsonderzoek.

Verder bedank ik natuurlijk alle huidige en voormalige PCN leden Pieter (de office buddy waarmee er altijd iets te beleven viel), Yolanda (het zonnetje in huis), Sofie (ex-studiegenoot en lotgeval) , Ruben, Tangi (van wie ik meer over bier geleerd heb dan wie dan ook), Antoine (met wie ik het groen op bureau in leven hield), Kim (die zorgde voor sfeer en gezelligheid) en zoveel anderen... Het zijn er zo velen om op te noemen en er zijn er gedurende die 4-5 jaar velen gepasseerd. Ik bedank jullie voor het gezelschap, de inzichten, de metingen en de vriendschap. Hierbij spreek ik sneller over vrienden dan over collegas, een unieke situatie die ik niet snel zal terug vinden in een andere werkomgeving. Het is nu aan de nieuwe leden (Jorick, Emile, Willem, Kishu, Dorian, Michael, Suzanne en wie er nog moge bijkomen) om er op zijn minst de zelfde sfeer in te behouden!

Ik bedank ook de mensen die me geholpen hebben bij mijn onderzoek te Olen, ik weet dat ik daar een beetje een vreemde eend in de bijt was en tussen jullie drukke werkschema door jullie aandacht kwam opeisen, maar des te meer appreciatie voor het hartelijk ontvangst elke keer ik passeerde, en de goeie hulp die jullie mij gegeven hebben. En hetzelfde geldt voor de mensen van de Universiteit van Luxemburg, die me gedurende enkele weken zeer goed hebben geholpen en waar ik me altijd welkom voelde!

Verder bedank ik al mijn vrienden die naast het werk waarmee ik de afgelopen 4 jaar zeer veel plezier heb beleefd. Ik bedank Laurens om in tijd en stond mij eens mee te nemen om iets te gaan drinken en voor vertier te zorgen. Miek om samen te gaan badmintonnen of te gaan lopen als ik nood had aan beweging na een volledige dag schrijven. Maarten, Kirian, Jonathan om met tijd en stond heroïsch te strijden in sport en spel, activiteiten waarvan ik hoop dat we ze nog lang kunnen uitvoeren. En ook de ex-studiegenootjes met wie ik gelukkig het contact nog niet verloren heb en blij ben op geregelde basis terug te zien.
Vanzelfsprekend mag mijn familie niet ontbreken, broer en zus, en natuurlijk mijn ouders van wie ik weet dat ik er altijd op kan rekenen, wat er ook is!
En natuurlijk , van wie ik als enige kan zeggen dat ik zonder haar dit nooit had kunnen doen, mijn vrouw, mijn Poepie, Katrien. Ik zie haar ongelofelijk graag en ik ben zeker dat we samen een mooie toekomst tegemoet gaan!

Gent, Maart 2015
Stijn Flamée

Table of Contents

List of Acronyms

A

Ac	Acetate
Acac	Acetyl Acetonate

C

CS	Copper Sulfide
CSe	Copper Selenide
CTS	Copper Tin Sulfide
CTSe	Copper Tin Selenide
CZS	Copper Zinc Sulfide
CZSe	Copper Zinc Selenide
CHNS-Analysis	Carbon Hydrogen Nitrogen Sulfide - Analysis
CIGS	Copper Indium Gallium Sulfide

D

DF	Dark Field
DLS	Dynamic Light Scattering
DMSO	Dimethyl Sulfoxide

E

EDX Spectroscopy	Energy Dispersive X-ray Spectroscopy
EG	Ethylene Glycol

F

FF	Fill Factor
FWHM	Full Width at Half Maximum

L

LED	Light Emitting Diode

M

MS	Mass Spectroscopy

N

NC	Nanocrystal
NMR	Nuclear Magnetic Resonance
NMRSTR	Nuclear Magnetic Resonance Structure Analysis
NP	Nanoparticle

O

OA	Oleic Acid
OC	Open Circuit
ODE	Octadecene
OLA	Oleylamine
OT	Octanethiol

P

PCN	Physics and Chemistry of Nanostructures

PL	Photoluminescence
PLD	Pulsed Layer Deposition
PLQY	Photoluminescence Quantum Yield
PV	Photovoltaics
PVD	Physical Vapor Deposition

Q

QD	Quantum Dot

R

RBS	Rutherford Back Scattering

S

SC	Short Circuit
SDD	Silicon Drift Detector
SILAR	Successive Ion Layer Adsorption and Reaction
STC	Standard Test Conditions

T

TCO	Transparent Conductive Oxide
TEM	Transmission Electron Microscopy
TFPV	Thin Film Photovoltaics
TGA	Thermogravimetric Analysis
TOP	Trioctylphosphine
TOPO	Tricoctylphosphine oxide

U

UV-VIS	Ultraviolet-Visible Light

V

VDWL	van der Waals

X

XPS	X-Ray Photoluminescence Spectroscopy
XRD	X-Ray Diffraction
XRF	X-Ray Fluorescence

Z

Z	Atomic Number

Nederlandstalige Samenvatting –Summary in Dutch–

Deze thesis beschrijft de synthese van nanokristallen en de toepassing ervan in dunne film fotovoltaïsche zonnecellen. In het eerste deel wordt een snelle en goedkope synthesemethode besproken voor chalcogenide nanokristallen, waarbij CdSe als model systeem wordt gebruikt. In het tweede en grootste deel wordt de toepassing van koper zink tin sulfide/selenide (CZTS(e)) nanokristallen in dunne film zonnecellen als goedkoper alternatief voor silicium gebaseerde zonnecellen beschreven.

Nanokristallen worden momenteel veelvuldig gebruikt in toepassing zoals LED schermen, foto-detectoren, foto-elektrochemische en fotovoltaïsche zonnecellen, enz. Deze toepassingen vereisen nanokristallen van hoge kwaliteit, die snel en goedkoop kunnen gesynthetiseerd worden. De meest gebruikte nanokristallen zijn de CdSe nanokristallen en deze kunnen op verschillende manieren gesynthetiseerd worden volgens de literatuur. De zoektocht naar een combinatie van een goedkope en snelle synthesemethode dat een hoge opbrengst levert is echter problematisch. In deze thesis maken we gebruik van een *hot injection* methode, waarbij we starten van een reactiemengsel dat bestaat uit cadmium of zink carboxylaat en een carbonzuur opgelost in octadeceen bij hoge temperatuur. Vervolgens wordt selenium poeder dat fijn verdeeld is in octadeceen geïnjecteerd in dit reactiemengsel, wat leidt tot de vorming van CdSe of ZnSe nanokristallen. Deze reactie is snel en eindigt binnen de 5 à 10 minuten. Daarenboven vertoont het een hoge opbrengst en leidt het tot nanokristallen met een hoge kwaliteit die een kleine grootte verdeling vertoont. In het geval van CdSe nankristallen, kan de finale grootte van deze kristallen gekozen worden door de reactiecondities aan te passen. Hierbij leidt het gebruik van kortere carbonzuren tot kleinere nanokristallen. Alle reacties kunnen onder lucht worden uitgevoerd waarbij de massa inhoud kan gaan tot 50 g/L. Hierbij is het interessant om op te merken dat de afwezigheid van een inerte atmosfeer (N_2 of Ar) de kwaliteit van het eindproduct niet verminderd. De oppervlaktechemie van de CdSe nanokristallen is identiek aan deze gerapporteerd in de literatuur, waardoor deze nanokristallen kunnen gebruikt worden als kernen waaruit CdSe/CdS kern/schil nanokristallen kunnen gegroeid worden. In ons geval is de resulterende fotoluminescente kwantumopbrengst groter dan 40%, wat vergelijkbaar is met de literatuur, wat terug impliceert dat onze methode leidt tot nanokristallen met een hoge kwaliteit. De reproduceerbaarheid van de CdSe nanokristallen synthese is getest via een geautomatiseerde syntheserobot. Dus onze synthesemethode is snel,

aanpasbaar, mogelijk in atmosferische condities en reproduceerbaar en leidt tot een hoge opbrengst van hoge kwaliteit colloïdale metaal selenide nanokristallen. Deze synthesemethode is daarom ook gepatenteerd, het pattent omvat het toevoegen van de chalcogenide precursor in poedervorm in plaats van een chalcogenide oplossing. Omwille van de kennis van deze aanpak, geloven we dat dit onderzoek kan leiden tot de verbetering van andere type nanokirstal syntheses.
We zijn echter voornamelijk geïnteresseerd in de synthese van koper zink tin sulfide/selenide (CZTS(e)) nanokristallen voor fotovoltaïsche (FV) toepassingen als een goedkoper alternatief voor de bestaande zonnecellen. Silicium wordt momenteel wereldwijd gebruikt als FV materiaal, maar het bezit een indirecte verboden zone dat leidt tot een minder efficiënt absorptie proces. Hierdoor zijn er relatief grote hoeveelheden silicium nodig voor één zonnecel. Dit leidde tot onderzoek naar andere materialen die een directe verboden zone, een hoge absorptie coëfficiënt en een verboden zone tussen 1,1 en 1,5 eV bezitten. Verschillende materialen kunnen beschouwd worden als mogelijk alternatief, namelijk CZTS(e), CdTe en koper indium gallium sulfide (CIGS). Hierbij bestaan CdTe en CIGS uit giftige en/of zeldzame elementen, waardoor CZTS(e) de ideale kandidaat is voor goedkope zonnecellen.
Binaire, ternaire en kwaternaire nanokristallen die geschikt zijn voor de fabricatie van CZTS(e) lagen voor FV toepassingen werden gesynthetiseerd startend van onze synthese voor metaal selenide nanokristallen, wat de veelzijdigheid van deze methode aantoont. Opdat CZTS(e) als zonnecel kan gebruikt worden, moet deze een p-type karakter vertonen. Dit wil zeggen dat er moet gestart worden van stabiele zink rijke nanokristallen. De gesynthetiseerde CZTS nanokristallen kunnen beschouwd worden als een mogelijke optie voor de fabricatie van dunne film FV zonnecellen. De grootte van deze nanokristallen is aanpasbaar, de opbrengst is groot en de kristallen bezitten de vereiste kesteriet kristalstructuur. De massa inhoud van deze synthese is 50 g nanokristallen voor 1 liter solvent wat bijna het dubbele is in vergelijking met de waarden gerapporteerd in de literatuur. CZTSe nanokistallen zijn niet direct een optie, aangezien deze zink arm zijn. Combinaties van binaire en ternaire nanokristallen worden preferentieel gevormd door Cu_2SnS_3 ZnS of Cu_2SnSe_3 ZnSe. Al deze syntheses vertonen een hoge opbrengst en worden eenvoudig geoptimaliseerd. De Cu:Sn ratio is in deze nanokristallen telkens 2:1 en de hoeveelheid zink kan eenvoudig aangepast worden aangezien zink geïntroduceerd wordt als aparte nanokristallen, in tegenstelling tot de CZTSe nanokristallen. Een combinatie van binaire SnS CuS ZnS nanokristallen zou mogelijk zijn indien de synthese van SnS nanokristallen geoptimaliseerd wordt en een hogere opbrengst behaald wordt.
Niet enkel de keuze van FV materiaal, maar ook de verwerking van de nanodeeltjes speelt een rol in de fabricatiekosten voor de finale FV materiaal. Hierdoor werd in dit project gekozen voor chemische oplossing depositie methodes, zoals *dropcasting*, inktjet printen en *doctor blading*, wat goedkoper is dan de veel gebruikte vacuümtechnieken. Chemische oplossing depositie methodes kunnen echter wel leiden tot structurele en elektronische defecten in de finale laag, maar het gekozen metaal chalcogenide gebaseerde materiaal bezit hiervoor een hoge tolerantie.

Voor de depositie is echter wel een inkt van hoge kwaliteit vereist. Dit betekent dat de inkt alle elementen moet bezitten die vereist zijn voor het eindmateriaal, zoals ze gesynthetiseerd zijn via de *hot injection* synthese. De gesynthetiseerde nanokristallen moeten echter ook stabiel blijven in dispersie voor een redelijke tijd. Dus voordat de gesynthetiseerde nanokristallen afgezet worden voor de fabricatie van een dunne film CZTS(e) zonnecel, werden de suspensies geanalyseerd met ^{1}H-NMR, *dynamic light scattering* (DLS) en zeta potentiaal metingen om zo de stabiliteit van deze suspensies te bepalen.
De gesynthetiseerde nanokristallen zijn sterisch gestabiliseerd in suspensie met oleylamine na synthese. Een uitwisseling van oleylamine naar kortere keten liganden of ladingsstabiliserende sulfide ionen was mogelijk. Het effect van deze uitwisseling werd geïdentificeerd en bestudeerd via ^{1}H-NMR. Hierbij hebben we aangetoond dat de oleylamine gestabiliseerde nanokristallen een dynamisch evenwicht vertonen tussen de liganden op de nanokristallen en de liganden in het solvent. Indien de liganden verwijderd worden van het oppervlak van de nanokristallen (via opzuivering) kan de resulterende inkt gedestabiliseerd worden wat kan leiden tot flocculatie. Hierdoor zijn de oleylamine gestabiliseerde inkten onstabiel in de tijd. Indien het oleylamine op de deeltjes echter uitgewisseld wordt met octaanthiol als coördinerend solvent, blijven de inkten wel stabiel in de tijd. Koolstofvrije (of ladingsgestabiliseerde) inkten kunnen gecreëerd worden door de organische liganden op het oppervlak van de nanokristallen te vervangen door sulfide anionen. DLS en zeta potentaal metingen leiden hier tot de conclusie dat deze liganduitwisseling leidt tot een stabiele inkt van geclusterde sulfide gestabiliseerde nanokristallen.
We hebben dus 3 verschillende inkten gecreëerd die geschikt zijn voor dunne film formatie: oleylamine, octaanthiol en sulfide (of koolstofvrije) gestabiliseerde nanokristal inkten. De oleylamine gebaseerde inkten vertonen een dynamisch evenwicht tussen het oleylamine en het solvent, waardoor de inkt dus een grote overmaat aan oleylamine moet bezitten opdat het over lange tijd stabiel is of dat een opgezuiverde inkt snel moet afgezet worden. Indien een inkt met overmaat aan oleylamine wordt gebruikt ontstaan kleine barsten in de film door de verwijdering van een grote hoeveelheid aan oleylamine tijdens de warmtebehandeling. De finale laag bezit dan nog steeds 20% koolstof, wat kan beschouwd worden als ongewilde contaminatie. Indien de overmaat aan oleylamine wordt verwijderd, waarbij nog minstens 80% van het oppervlak van de nanokristallen bedekt blijft, kunnen er lagen zonder barsten gevormd worden. Deze lagen zijn 1,5 μm dik na een enkele depositie en vertonen geen problemen tijdens de droogstap en warmtebehandeling. Deze behaalde dikte is hoger dan het theoretische maximum van 400 nm voor 25 nm nanokristallen. Dit kan verklaard worden door de aanwezigheid van het oleylamine dat zich gedraagt als een binder dat de stress in de film vermindert. De finale laag bezit wel nog 7,5% koolstof. Indien octaanthiol als coördinerend solvent wordt gebuikt kan in eerste instantie ook een laag van 1,5 μm afgezet worden. Als echter het thiol verwijdert wordt door de laag te verwarmen, stijgt de normale stress in de film door het verdampen van het solvent, wat leidt tot barsten in de afgezette laag. Dit kan omzeild worden via meerdere depo-

sities van 300-400 nm dikke lagen via inktjet printen. Tussentijdse verwijdering van de overmaat aan thiol via een warmtebehandeling is vereist om herdispersie in de volgende afgezette laag te voorkomen. Via meerdere deposities kan finaal een laag van 1,5 μm geproduceerd worden. De koolstofvrije inkten bestaan uit gedispergeerde 600 nm clusters van 25 nm individuele nanokirstallen. Deze clusters maken het mogelijk om een barstvrije film van 1,5 μm af te zetten tijdens een enkele depositie. Deze film is echter poreus en bestaat uit kleine gaten. Dus de drie verschillende inkten zijn geschikt om een film te vormen van 1,5 μm dikte. We konden deze stabilisatie- en depositiemethoden toepassen op de CZTS, CZTSe, Cu_2SnS_3 en ZnS nanokristal systemen wat impliceert dat deze kennis van inkt formulatie en depositie kan getransfereerd worden naar andere nanokristal systemen. In de gefabriceerde nanokristal films zijn er nog veel korrelgrenzen aanwezig tussen de aanwezige nanokristallen en deze moeten verminderd worden om excessieve recombinatie en elektron gat paar vernietiging te vermijden, opdat een geschikte CZTS(e) zonnecel kan geproduceerd worden. Hiervoor moeten deze films gedensificeerd worden via de groei van de nanokristallen dat kan geïnduceerd worden via *annealing*. De nanokristallen bezitten reed de vereiste stoichiometrie, waardoor een thermische *annealing* proces genoeg kan zijn om een dense CZTS(e) film te vormen. Een CZTSe koolstofvrije nanokristal film werd thermisch behandeld bij 450 °C, waarbij we ontdekten dat kristalgroei werd gepromoot indien vormingsgas gebruikt wordt in plaats van een neutrale atmosfeer. In neutrale atmosfeer zullen de aanwezige sulfide anionen oxideren naar sulfoxides wat kristalgroei tegen houdt. Deze sulfoxides kunnen gereduceerd worden in de aanwezigheid van H_2, waardoor de nanokristallen kunnen groeien. De kristalgroei was echter beperkt, waardoor de behandelde laag nog steeds uit nanokristallen en meerdere korrelgrenzen bestond. Om deze reden maakten we gebruik van een zwavel of selenium rijke atmosfeer tijdens de thermische *annealing* (sulfurisatie of selenisatie). Indien sulfurisatie of selenisatie wordt uitgevoerd op de CZTS nanokristal filmen merken we dat de aanwezigheid van koolstof vereist is om kristalgroei te induceren. Deze fase transformatie resulteerde in een dubbel gelaagde structuur. De bovenste laag bestond uit grote stoichiometrische CZTS(e) kristallen, terwijl een koolstofrijk granulair deel aanwezig was in de onderste laag. Het verschil tussen de oleylamine en thiol gebaseerde stabilisatie kwam tot uiting aan het oppervlak van de laag. De oleylamine gebaseerde lagen vertonen een ruw oppervlak, omwille van volume reductie van de laag tijdens de *annealing* en dus densificatie in vergelijking met de thiol gebaseerde lagen waarbij het oppervlak glad bleef. Dit effect leidde tot een beter cel efficiëntie voor de thiol gebaseerde cellen (2,3%) in vergelijking met de oleylamine gebaseerde cellen (1,5%). De koolstofvrije CZTS lagen bleven volledige nanokristal lagen na sulfurisatie of selenisatie en vertoonden daarom 0% efficiëntie.

Daar koolstofvrije lagen geen kristalgroei vertoonde werd een composiet CZTS laag behandeld via *annealing*. CZTS bezit een lagere vrije vormingsenergie in vergelijking met zijn composieten waardoor de combinatie van de composieten thermodynamisch gezien CZTS zullen vormen. De koolstofvrije Cu_2SnS_3 nanokristallen vormen grote Cu_2SnS_3 kristallen met een diameter van ongeveer 2 μm

na sulfurisatie of selenisatie. Dus we combineerden de koolstofvrije Cu_2SnS_3 met koolstofvrije ZnS nanokristallen om zo een stoichiometrische CZTS(e) film te vormen. Na sulfurisatie werd zoals voorspeld CZTS gevormd doorheen de laag, maar kristalgroei bleef gelimiteerd volgens XRD (van 12 nm tot 38 nm). Selenisatie van een Zn rijke en Cu arme compositie resulteerde in een gelimiteerde kristalgroei dat leidde tot kleine kristallen en de vorming van een granulaire Zn rijke residu. Selenisatie van een stoichiometrische laag leidde echter wel tot een optimale kristalgroei, maar omwille van volume reductie ontstonden er grote barsten in de film tijdens de *annealing* procedure, waardoor deze onbruikbaar werd voor de fabricatie van een zonnecel.

English Summary

This thesis elaborates on nanocrystal synthesis and its applications in thin film photovoltaics. First, a fast and cheap method is discussed to synthesize chalcogenide nanocrystals, using CdSe as model system. The second and main part discusses a nanoparticle approach for CZTS(e) (Copper Zinc Tin Sulfide/Selenide) thin film solar cells as cheaper alternative for Si-based solar cells.

Nowadays, nanocrystals are used in numerous applications like LED displays, photo-detectors, quantum dot solar cells, photovoltaics, etc. These application need high quality nanocrystals, preferably synthesized in a cheap and fast manner. The most widely used nanocrystals are the ones of CdSe, and they can be synthesized in various ways according to literature. However, the search to the combination of a cheap and fast method leading to high yields remained problematic. We have demonstrated that the injection of selenium powder dispersed in octadecene in a reaction mixture containing either cadmium or zinc carboxylates dissolved in octadecene and an excess of carboxylic acid initiates the formation of CdSe and ZnSe nanocrystals. The reaction is fast, running to completion within 5 min, shows a high yield even for small nanocrystals, and leads to high quality nanocrystals with low size dispersions. Moreover, in the case of CdSe, the final size of the nanocrystals can be tuned by changing the reaction conditions, where shorter chain carboxylic acids yield, for example, larger nanocrystals. The reactions can be executed under air and with solid loadings as high as 50 g/L. Importantly, the absence of a protective atmosphere during synthesis does not compromise the quality of the end product (PLQY, size distribution). In the case of CdSe, the surface chemistry of the nanocrystals is identical to what has been reported in the literature, and they can be used as cores to grow CdSe/CdS core/shell nanocrystals with photoluminescence quantum yields exceeding 40%. We argue that the combination of a fast and tunable, high yield reaction with atmospheric conditions and high solid loadings make the approach highly suited for the low cost, high volume production of colloidal metal selenide nanocrystals. This conclusion is stressed by demonstrating the reproducible synthesis of CdSe nanocrystals using the heterogeneous precursor by an automated liquid handler. Because this chalcogenide system can be considered as a model system, we believe that this research opened the door to the improvement of other types of nanocrystals synthesis.

However, we were not only interested in CdSe nanocrystals, but also in copper zinc tin sulfide/selenide (CZTS(e)) nanocrystals for photovoltaic (PV) applications as a cheaper alternative for existing solar cells. Silicon is used world-wide as a PV material, however it has the disadvantage that it contains an indirect bandgap, leading

to a less efficient absorption process and the need for a larger amount (100 nm thickness) of Si in a solar-cell, but for processing reasons between 200 and 500 nm of silicon is used. This opened the research towards materials with a direct bandgap, a high absorption coefficient and a bandgap between 1.1-1.5 eV. Different materials, like CZTS(e), CdTe and copper indium gallium sulfide (CIGS), are considered as a suitable alternative. However, only CZTS(e) consists of non-toxic earth-abundant elements, making it the ideal candidate for the production of cheap solar cells, compared to the toxic and scarce CdTe and CIGS respectively. We choose to use a particle based route instead of a molecular precursor route. Without the use of toxic and explosive solvents like hydrazine or the use of big complexing agents the solubility of molecular precursors in inks is generally low. Therefore we choose to use a particle dispersion to increase the precursor material in our ink.

The method for synthesizing CdSe nanocrystals was transferred to the synthesis of binary, ternary and quaternary nanocrystals suitable for the preparation of CZTS(e) layers for PV applications, showing the versatility of this method. In order to obtain CZTS(e) solar cells exhibiting a P-type characteristic, stable and Zn rich particles should be synthesized. The synthesized CZTS nanocrystals are a viable option to obtain the CZTS thin film PVs. These nanocrystals are tunable, show the desired crystal structure, being kesterite and the yield is high. Furthermore, the solid loading of our synthesis is 50 g/L of solvent, almost double compared to literature. CZTSe nanocrystals, on the other hand, seem less viable since these are Zn poor. Combinations of binary and ternary nanocrystals are preferably formed using Cu_2SnS_3 - ZnS, Cu_2SnSe_3 - ZnSe or ZnSnS - CuS. Most synthesis show a high yield and are easily optimized. The Cu:Sn ratio can be set at 2:1 and the Zn can be tuned as desired since the Zn is introduced through the addition of separate particles that can be added in a desired amount, in contrast to CZTSe nanocrystals. A combination of the binary particles SnS - CuS - ZnS could be possible, only if the SnS is optimized and higher yields would be obtained.

Not only the choice of PV material, but also the processing plays a role in fabrication costs of the final PV material. Hence, in this project chemical solution deposition methods, like dropcasting, inkjet printing and doctor blading, were chosen as thin film formation instead of the more expensive vacuum techniques. When switching from high vacuum deposition techniques towards wet chemical depositions a high tolerance towards structural and electronic defects in the final layer is required. Similar materials such as CIGS and CdTe have shown that the non-vacuum depositions are able to reach high efficiencies. However for deposition, a high tech ink needs to be delivered. This means that the ink must comprise the elements it needs, which have been synthesized using hot injection synthesis. Here, the synthesized nanocrystals need to remain stable in dispersion for a reasonable time. So, before these synthesized nanocrystals are deposited to prepare a thin film CZTS(e) solar cell, the suspensions were analyzed via ^{1}H-NMR, dynamic light scattering (DLS) and zeta potential measurements to determine its stability.

Our as-synthesized nanocrystals yield steric stabilized dispersion via oleylamine (OLA), but an exchange from the original stabilizer to shorter chained ligands or

charge stabilizing sulfide anions was possible. The effect of this exchange was identified and studied using ^{1}H-NMR and these results could be linked to ink stability and flocculation. We showed that OLA stabilized nanocrystals acquire a dynamic equilibrium between the ligands on the nanocrystals and the OLA ligands in the solvent. Ligand loss on the surface (due to purification) can lead to destabilization and flocculation of the ink. So, OLA stabilized inks are not long term stable. However, the inks remain stable over time, if the OLA on the nanocrystals surface is exchanged by octanethiol as coordinating solvent. C-free charge stabilized inks were created by replacing the organics on the nanocrystal surface with sulfide anions. DLS and zeta potential measurements led to the conclusion that this ligand exchange led to a stable ink of clustered sulfide stabilized CZTS.

So, three different inks were suitable for layer formation: OLA, octanethiol and carbon-free based nanocrystal inks. The OLA stabilized nanocrystals show a dynamic equilibrium between the OLA and the solvent, which means that the ink must contain a large excess of OLA to be long term stable or it must be deposited quickly after a purification step (removing the excess OLA). Using an ink with excess OLA causes small cracks and craters in the surface due to the removal of the large amount of OLA upon heat treatment, also the final layer contains nearly 20 wt% of carbon, which could be an undesired contamination. When removing the excess of OLA, but leaving the nanocrystals with at least 80% of its capping, crack-free single deposited layers of 1.5 μm can be formed. Here the drying and heat treatment posed no problem. The obtained thickness is higher than the theoretical maximum of 400 nm thickness for 25 nm nanocrystals due to the OLA that acts as a binder, reducing the stress in the film. A drawback is that the final film still contains up to 7.5 wt% of carbon. If octanethiol is used as a coordinating solvent a layer of 1.5 μm can be deposited in first instance. However, removing the thiol by heating above its boiling point, increasing the normal stress on the film, leads to cracks in the deposited layer that even peels of the substrate. This can be circumvented by multilayer deposition of 300-400 nm thin films via inkjet printing. Intermediate removal of excess thiol, via heat treatment, is required to prevent redispersion in the next deposited layer. So, again crack-free layers of 1.5 μm can be produced. The use of carbon-free stabilized inks does not exhibit any binder in the dispersion, but due to the nature of the exchange, not individual nanocrystals of 25 nm but clusters up to 600 nm are dispersed. These clusters still make it possible to deposit a layer of 1.5 μm in one deposition. When dried carefully a crack-free and carbon-free layer can be deposited although the layer appears more porous, containing small voids compared to the C-stabilized based inks. So, the three different inks are suitable for depositing a film of 1.5 μm. We were also able to apply our formulation and deposition methods to the CZTS, CZTSe, Cu_2SnS_3 and ZnS nanocrystal systems, indicating that the gained knowledge on ink formulation and film deposition can be transferred to other nanocrystal systems.

To obtain a suitable CZTS(e) solar cell, the fabricated nanocrystal films are thermally annealed to induce densification in the film via grain growth to avoid excessive recombination and carrier scattering from the boundaries between the nanocrystals. Since the nanocrystals already contain the right stoichiometry, a thermal an-

nealing process could be enough to form a dense CZTS(e) film. We treated a CZTSe C-free nanocrystal layer up to 450 °C to discover that crystal growth improved using forming gas instead of neutral atmosphere. This was explained by the oxidation of the sulfide anions in sulfoxides in a neutral atmosphere which inhibited crystal growth. These sulfoxides can be reduced in the presence of H_2, leading to a slightly increased crystallite size. However, the layer remained a nanocrystal layer with multiple grainboundaries. Therefore, we switched to a sulfur or selenium rich atmosphere during thermal annealing (sulfurization and selenization). When performing sulfurization and selenization on CZTS nanocrystal layers we discovered that the presence of C is necessary to induce crystal growth. This phase transformation resulted in a double layered structure with large sized stoichiometric CZTS(e) on top and a C containing granular layer below. A difference occurred between OLA and thiol based stabilization. OLA based layers exhibited a rough top layer since the volume reduction during the densification process was larger compared to thiol based layers for which the surface remained smooth. This effect was translated in a better cell efficiency for the thiol based cells (2.3%) compared to the OLA based cells (1.5%). C-free CZTS layers remained a complete nanocrystal layer after selenization or sulfurization and showed 0% efficiency.
Since C-free CZTS did not show grain growth, a composite layer of ZnS and CTS was annealed. CZTS has a lower free energy of formation compared to its composites thus the combination should thermodynamically favor the formation of CZTS. The C-free Cu_2SnS_3 nanocrystals showed the formation of large Cu_2SnS_3 crystals with a diameter of 2 μm upon sulfurization and selenization. Thus we combined C-free CTS with C-free ZnS to form a stoichiometric nanocrystal layer. When sulfurizing the layer, CZTS was formed throughout the layer, but grain growth was still limited as from 12 nm to 38 nm according to XRD. Selenization of the by literature preferred Zn-rich Cu-poor composition resulted in a limited grain growth leading to small crystals and the formation of a granular Zn-rich residue. Selenization on a stoichiometric layer on the other hand showed optimal grain growth. However, the stoichiometric starting layer was slightly porous, which resulted in cracking after densification due to volume reduction, making it impossible to fabricate a working device.

1 Introduction

This thesis will elaborate on nanocrystal (NC) synthesis and it applications for thin film photovoltaics. First, a fast and cheap method is discussed to synthesize chalcogenide nanocrystals, in which CdSe is used to develop the methodology. The methodology is extended towards NC synthesis for a NC approach in the fabrication of CZTS (Copper Zinc Tin Sulfide/Selenide) thin film solar cells as cheaper alternative for Si based solar cells. After synthesis, we processed the synthesized NC as a NC ink into a crack-free 1.5 μm thick film. To reduce grain boundaries and improve carrier separation we densified the NC film into a large grained crystal structure.
This project was written in 2010 as a collaboration between the PCN (Physics and Chemistry of Nanostructures) research group of Ghent University and the Functional Materials Research Group at Umicore. The expertise of the PCN group lies within nanocrystal (NC) synthesis, mainly using bottom-up approaches to synthesize quantum dots, and the subsequent characterization of these fabricated nanomaterials. Umicore, on the other hand, proved at that point to be successful in ink stabilization and thin film processing of a variety of materials.

Nowadays, NCs are used in numerous applications like LED displays, photodetectors, photovoltaics, etc. These applications need high quality NC, preferably synthesized in a cheap and fast manner. One of the most widely used NC within the visible range are the ones of CdSe. They can be synthesized in various ways according to literature [1]. However, the search for a combination of a cheap and fast method leading to high yields remained problematic. In this thesis, we

proposed an alternative approach to synthesize these NCs, via hot-injection synthesis, in a cheap and fast manner and a chemical yield near 100%. Our approach is up to 20 times faster than literature based methods, while the synthesis costs are reduced by the use of less expensive solvents, the possibility to work in atmospheric conditions and to obtain higher solid contents in solution. We believe that this research opened the door to the improvement of other types of NCs synthesis. We wanted to use the advantages of our developed method for the synthesis of chalcogenide NCs in a broader application field.

We were particularly interested in the synthesis of copper zinc tin sulfide/selenide (CZTS) NCs for photovoltaic (PV) applications as low cost alternative for existing solar cells. Silicon is used worldwide as a PV material, however it has the disadvantage that it contains an indirect bandgap, leading to a less efficient absorption process and the need for massive amounts of Si in a solar-cell. CZTS, CdTe and copper indium gallium selenide (CIGS) contain a direct bandgap, making it possible to reduce the layer thickness of the solar cell, and thus the fabrication costs. Moreover, CZTS consists of non-toxic and earth-abundant elements, making it the ideal candidate for the production of cheap solar cells, compared to the toxic and scarce CdTe and CIGS respectively.

Not only the choice of PV material, but also the processing plays a role in the fabrication cost of the device. Solution based processing is generally considered as a cheap alternative for the state-of-the-art vacuum deposition techniques since it allows roll to roll deposition. CZTS solution based processing has proven very successful, especially with hydrazine based inks. Hydrazine is a solvent that allows a high concentration of Cu , Zn, Sn and S/Se to be dissolved, but has the disadvantage of being toxic and explosive. Therefore, we chose to follow a NCs based route to fabricate inks for CZTS absorber layer fabrication.

2

CZTS: An Abundant Non-Toxic Absorber Layer

2.1 Thin Film Photovoltaics

To understand the reasoning behind our choice of CZTS we first take a look at the existing PV (photovoltaics) market. It is common knowledge that silicon is 'the' material for PVs, as it is incorporated in everyday life as solar cell panels on our rooftops. But why silicon? The most suiting answer would be: "It is abundant and contains more or less the right bandgap"' [2, 3]. The bandgap determines the possible yield of a single p-n junction solar cell. The Shockley-Queisser limit – first calculated by William Shockley and Hans Queisser – refers to the maximum theoretical efficiency of a PV module using a single p-n junction collected from the sun [4]. Schokley and Queisser found that a decent solar cell in the earth atmosphere preferably has a bandgap between 1.1-1.5 eV, with a maximum energy conversion of 33,7% at 1.34 eV.
Crystalline silicon (c-Si) has a bandgap of 1.1 eV, which is close to the maximum efficiency bandgap. However, for semiconductors materials the bandgap is either a direct or an indirect bandgap. For an indirect bandgap a shift in crystal momentum (a phonon) is required to absorb a photon. For a direct bandgap no change crystal momentum is required. The difference is visualized in Figure 2.1. The consequence is that indirect bandgaps are less efficient in the absorption of photons compared to direct bandgaps and therefore require more material to absorb a photon [5]. Crystalline silicon has an indirect bandgap, and therefore, a large

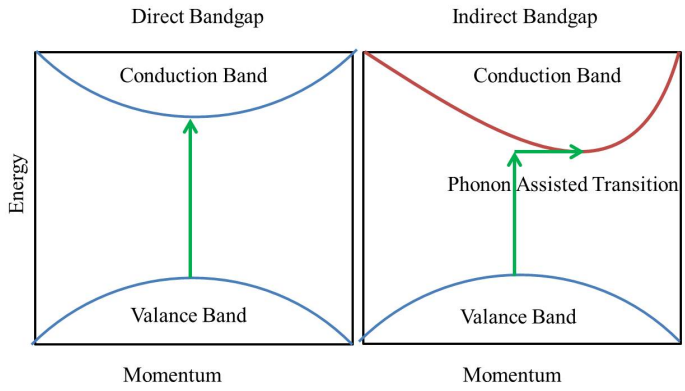

Figure 2.1: Indirect vs direct bandgap in semiconductors. Left: A direct bandgap material. Right: Indirect bandgap which requires a phonon to absorb a photon

amount of Si is necessary to build a single junction cell (up to 260 μm thickness). Silicon is very abundant (Figure 2.2a), making it a cheap resource. However, producing crystalline silicon is expensive, making the raw materials cost per watt of crystalline silicon modules relatively high [6] (see Figure 2.2b).

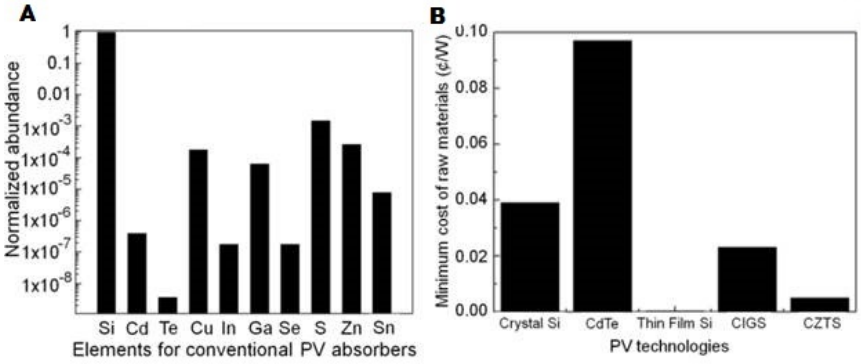

Figure 2.2: A: Relative abundance of the elements that are commonly used for solar cell production. B: Minimum cost of raw materials used per watt of solar cell power produced [7].

These disadvantages of Si rose the common interest in materials with a direct bandgap, a high absorption coefficient and a bandgap between 1.1-1.5 eV. Three materials were considered as a suitable replacement of c-Si, namely amorphous Si (a-Si), CdTe and copper indium gallium sulfide (CIGS) all displaying a direct bandgap (see Table 2.1). The use of these new materials, make it possible to re-

duce the layer thickness to 1.5 μm compared to the 260 μm required for silicon [7]. Hence, the absorber use of thin film PV (TFPV) compared to c-Si films leads to a reduction in material use of approximately 200 times. Fabricating solar cells with a thickness of 1.5 μm brings other advantages except material reduction. It could allow flexible substrate based solar cells, integrated solar cells or the fabrication of transparent solar cells (these require less then 1.5 μm films)

This TFPV technology was chosen as one of the inventions of the year by time

	c-Si	a-Si	CdTe	CIGS
Bandgap (eV)	1.1	1.7	1.5	1-1.6
Absorption Coefficient (cm^{-1})	$> 10^2$	$> 10^4$	$> 10^5$	$> 10^5$

Table 2.1: Absorption coefficient and bandgap of possible solar cell materials.

magazine in 2008 [8]. Due to this new technology, by the use of new absorber materials in Table 2.1, and the high cost and energy consumption input in manufacturing c-Si PV modules, market share of the c-Si technology has been dropping to 71%, while the TFPV technologies have been increasing rapidly by 2010 (see Figure 2.3). Up till now, three main TFPV technologies exists, CdTe, CIGS, and thin film a-Si. In 2010 they had gained a market share of 14%, 9%, and 6% respectively [9]. In fact, annual investments in new thin-film equipment exceeded $1 billion from 2007 to 2012. However, c-Si still dominates the market today, and funding for the existing TFPV technologies is dropping. For TFPV the high potential efficiency is still not reached for cheaper production methods and cheap Si modules flood the PV market. This explains the drop in shares of the TFPV after 2010 in Figure 2.3 [9]. On top of that, the CdTe TFPV technology is restricted because of the usage of the toxic heavy metal Cd and the limited supply and thus fluctuating prices of Te, making CdTe still more expensive than c-Si (see Figure 2.2a and b) [7]. The TFPV CIGS show a lower production cost compared to c-Si, but due to the respectively scarceness of In neither TFPV is able to take over the market. [10].

It became clear that TFPV modules needed a cheaper alternative. Not only in fabrication cost, but also in terms of raw materials. Starting around the late 2000s, a quaternary semiconductor compound Cu_2ZnSnS_4 (CZTS) gained an increased interest as an alternative PV material [11]. CZTS is a compound semiconductor of $(I)_2(II)(IV)(VI)_4$ with a high absorption coefficient ($\geq 10^4$ cm^{-1}) and a desirable bandgap (1.45 eV) and can therefore be considered as a suitable thin film PV material [9]. It shows similarities in material properties with CIGS, with the major advantage that the raw materials are abundant (Figure 2.2a) making them less expensive.

It became clear that TFPV modules needed a cheaper alternative. Not only in fab-

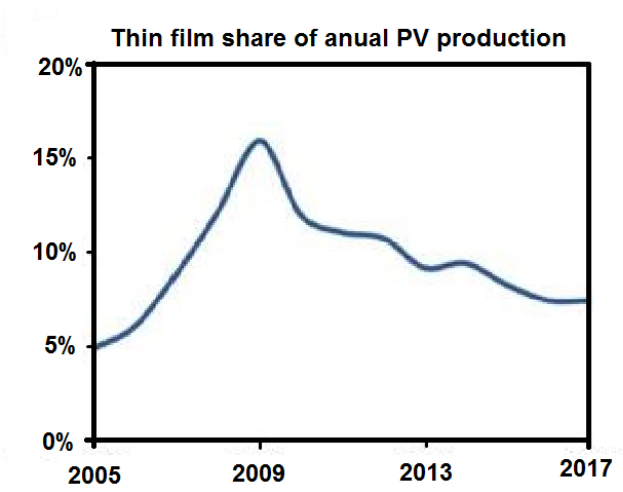

Figure 2.3: The share of TFPV annually produced on the PV market [7].

rication cost, but also in terms of raw materials. Starting around the late 2000s, a quaternary semiconductor compound Cu_2ZnSnS_4 (CZTS) gained an increased interest as an alternative PV material [11]. CZTS is a compound semiconductor of $(I)_2(II)(IV)(VI)_4$ with a high absorption coefficient ($\geq 10^4$ cm^{-1}) and a desirable bandgap (1.45 eV) and can therefore be considered as a suitable thin film PV material [9]. It shows similarities in material properties with CIGS, with the major advantage that the raw materials are abundant (Figure 2.2a) making them less expensive.

Theoretical calculations using the Shockley-Queisser limit show that conversion efficiency with a few micrometers of CZTS can be as high as 32%, comparable to c-Si. The benefit of CZTS can be proven by comparing its cost/Watt with other modules in Figure 2.2b. Hence, we can conclude that the minimum cost of raw materials for the existing PV technologies compared with CZTS, makes CZTS a cheaper alternative if an equally efficient cell could be made. Therefore, in theory, CZTS has all the right properties to be a great alternative to compete with the silicon based modules.

Note that a-Si thin film solar cells are cheaper in terms of raw material costs, but the downside of this technology is that it can not reach sufficient efficiency, due to the Staebler-Wronski effect and it shows a poor long-term stability [12], for that reason it is mainly used for small and lower power applications.

2.2 Properties of CZTS

2.2.1 Crystal Structure

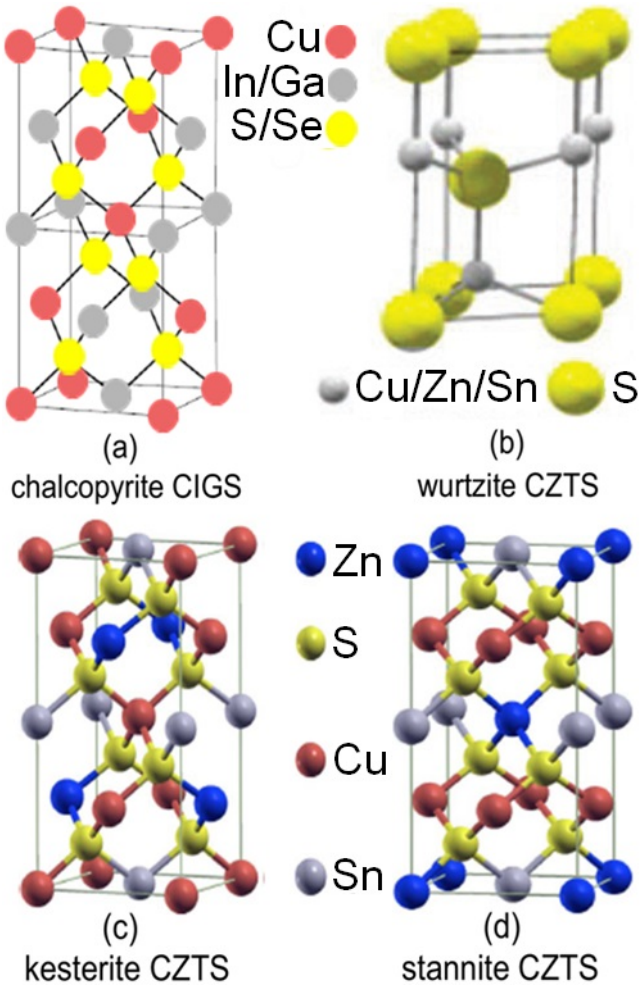

Figure 2.4: A graphical representation of the crystal structures of Chalcopyrite CIGS (a), Wurtzite CZTS (b), Kesterite CZTS (c) and Stannite CZTS (d) [9]

Generally CZTS thin films are polycrystalline, mainly consisting of the thermodynamically stable kesterite crystal structure. Kesterite (CZTS single crystal) was first synthesized in 1967 by Nitzche et al. [13], by means of a chemical vapor transport method. X-ray diffraction (XRD) analysis showed that the synthesized kesterite CZTS had a c/a close to 2 (a = 5.43 Å, c = 10.83 Å). In 1974,

an extended study of lattice parameters of a CZTS single crystal was reported by Schafer and Nitzche [14], which is generally referred to, to determine the CZTS phase. Kesterite CZTS has a similar crystal structure to chalcopyrite CIGS, in which half of the indium and/or gallium is replaced by zinc and the other half by tin (Figure 2.4a). Similar to ZnO or ZnS zincblende structures, the anions and cations in kesterite CZTS crystal are located in a tetrahedral bonding environment (Figure 2.4c). The less thermodynamically stable wurtzite CZTS phase was synthesized for the first time in 2011 by Lu et al. [15], in which wurtzite CZTS NCs were obtained through a hot injection method. A third important crystal structure for CZTS is the stannite structure (Figure 2.4d). The stannite phase is very similar to the kesterite phase – the difference lies only between a different ordering in the cation sub-lattice – which makes it difficult to distinguish between both phases in XRD analysis. Chen et al. found that the kesterite structure has a lower free energy and should be more stable than the stannite structure, which is derived from first-principle calculations. [16]. However, Scragg et al. investigated the formation of order kesterite in closer detail using using near-resonant Raman scattering. This showed that a ordered kesterite structure does not exist above 533 K. But instead a disordered kesterite structure is formed. When cooled down an ordered kesterite structure can still appear [17].

2.2.2 Optical Properties

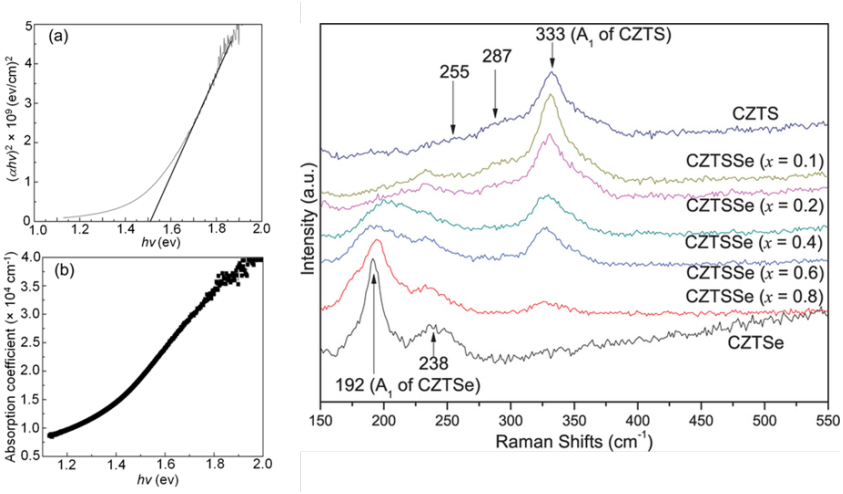

Figure 2.5: Left: the a) Typical bandgap and (b) absorption coefficients of a CZTS thin film Right: the Raman spectra of CZTS crystals with different S-Se ratios [9]

The optical bandgap of CZTS is experimentally determined to be 1.4 - 1.5

eV, depending on the used method to synthesize CZTS thin films. CZTS thin films have an absorption coefficient higher than 10^4 cm^{-1} within the energy range higher than 1.2 eV (Figure 2.5) [9].
Raman spectroscopy is a powerful characterization method to reveal Raman shift peaks in CZTS for the peaks associated with secondary phases such as Cu_xS, ZnS, Sn_xS and Cu_3SnS_4, but it is especially used to identify the presence of kesterite in the layer. The universally acknowledged peak is 336 cm^{-1} for sulfide based kesterite and 193 cm^{-1} for selenide based CZTSe [18]. If the secondary phase of Cu_2SnS_3 is present as 30% or less, it can not be discerned using XRD or RAMAN and requires other identification such as XANES [19].

2.2.3 Electrical Properties

Producing n-type and p-type semiconductors of silicon requires the introduction of atoms like phosphorus or boron in the crystal lattice. In contrary to silicon, CZTS is a self-doped material through the formation of intrinsic defects [20]. These defects are mainly vacancies (V_{Cu}, V_{Zn}, V_{Sn}, and V_S), anti-site defects (Cu_{Zn}, Zn_{Cu}, Cu_{Sn}, Sn_{Cu}, Zn_{Sn}, and Sn_{Zn}), and interstitial defects (Cu_i, Zn_i, and Sn_i). These defects typically form during growth of CZTS thin film. First-principle calculations on the defect properties of CZTS studies done by Chen et al [16] found that the formation energy of n-type doping was higher than the formation of p-type doping, making it an intrinsic p-type doped material. Conductivity of CZTS thin films comes mainly from the Cu_{Zn} anti-site defects. This is the reason why CZTS thin films are preferably Cu poor and Zn rich amongst other reasons also to avaoid other secondary phases, the formation of ZnS is relatively benign.

2.3 The Basics of a Thin Film Solar cell

2.3.1 Building a Solar Cell

A solar cell can be approached as a battery in a simple electrical circuit (Figure 2.6a) for which the battery will not work, if the solar cell is not illuminated. However, the solar cell will operate as a battery if it is activated by light (Figure 2.6b). Under illumination the solar cell will provide an electrical potential difference, leading to a flow of electrical current through the solar cell. The potential difference derived at infinite resistance is defined as an open circuit voltage, V_{OC}. In correspondence, short circuit current, J_{SC}, is the electrical current flowing in the circuit with the load at zero resistance. Figure 2.6c shows a typical current - voltage (I-V) relationship curve where the load resistance changes from zero to infinite while the solar cell is illuminated. Different parameters need to be defined to characterize different solar cells. The power delivered by the solar cell, P, is

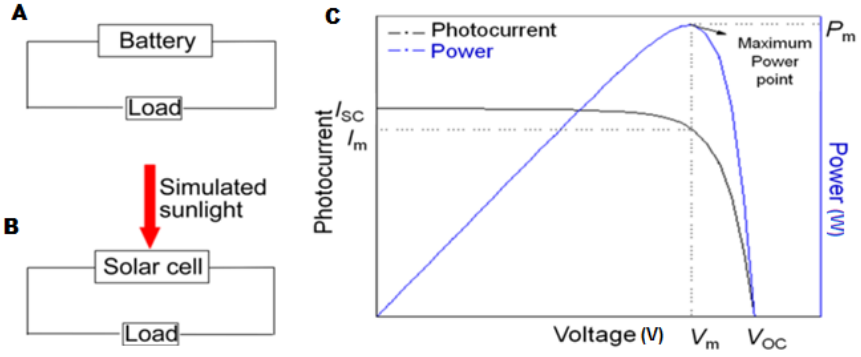

Figure 2.6: (a) Schematic basic electrical circuit, (b) schematic basic operating circuit of solar cell, (c) typical I-V curve of a solar cell. [9]

given by

$$P = IV \tag{2.1}$$

The typical P-V relationship curve is also shown in Figure 2.6. When the solar cell delivers the highest power to the external load, P reaches a maximum value. This happens at a certain condition which is defined as the maximum power and is denoted as P_m. The corresponding voltage and current are V_m and I_m, respectively.
The fill factor, FF, an important parameter to evaluate a solar cell is calculated at the maximum power and is defined as:

$$FF = I_m V_m / I_{SC} V_{OC} \tag{2.2}$$

The most important and distinct parameter for a solar cell is the conversion efficiency (μ) which describes the solar cells ability to translate solar energy into electrical energy. The conversion efficiency is defined as:

$$\mu = P_m / P_L \tag{2.3}$$

where P_L represents the power of the simulated light. Because of the fact that parameters such as J_{SC} , V_{OC} , FF, and μ are light-dependent and environment-dependent (variable at different illumination and with different light intensities), these parameters are worldwide recognized characterization condition for solar cells is the Standard Test Condition (STC). This settles that a solar cell should be tested at 25 °C under an air mass coefficient of 1.5 of the spectral illumination with an incident power density of 100 mW/cm^2.

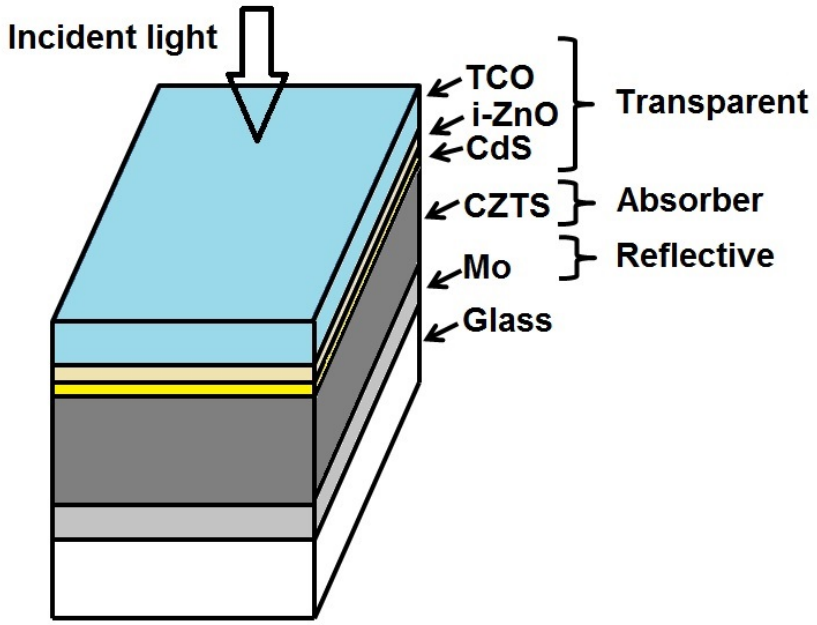

Figure 2.7: The basic build up of a thin film solar cell

2.3.2 Basic Structure of the Thin Film Solar Cell

The basic build-up of a CZTS solar cell is shown in Figure 2.7. The bottom layer exists of a molybdenum thin film with a thickness of 500 to 700 nm that is sputtered on a glass substrate, serving as a back contact. Molybdenum (Mo) is used because it has a low work function when the electron or hole has to be transferred from the CZTS to the Mo, resulting in a minimal energy loss. Mo is fairly stable in severe reactive conditions such as sulfur/selenium-containing vapor and high temperature but still a small $MoS(e)_2$ layer on the interface can be formed, increasing the work function and lowering the efficiency of the transfer of the electron into the external circuit. Therefore there is still ongoing research for an alternative back contact [21]. The absorber layer consist of a CZTS thin film which is intrinsic p-type. Optimally, the film thickness ranges from 1.0 to 2.0 μm and is deposited on the Mo layer. To form a p-n junction with the p-type CZTS, a CdS thin film of 50 to 100 nm is deposited on top of the absorber layer, which is generally performed by chemical bath deposition, this CdS layer serves as a buffer layer to prevent short circuits and to ensure electron transfer. In most cases, the surface of CZTS thin film is too rough to be fully covered by a CdS thin film. to enhance the p-n junction a 50 to 90 nm n-type intrinsic ZnO (i-ZnO) thin film is additionally coated on the CdS layer via sputtering. As a front contact a transparent conducting oxide

(TCO) film with a thickness of 500 to 1000 nm is sputtered. Finally, to electrically connect and measure the I-V property of the cell, a Ni/Al grid is deposited and connected to the Mo and the TCO.

2.4 CZTS and its Secondary Phases

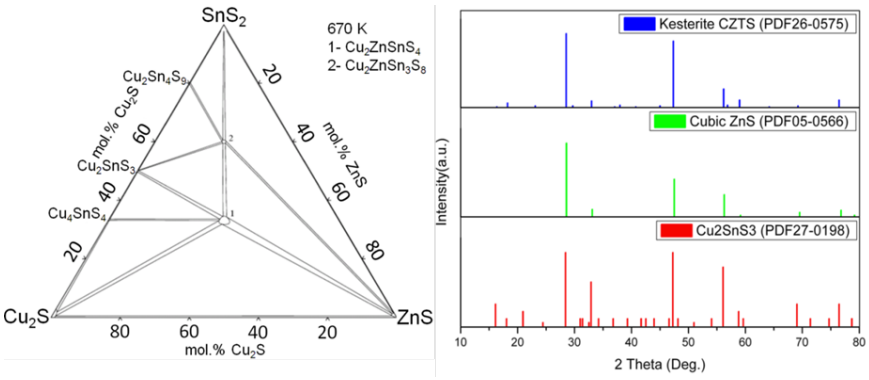

Figure 2.8: Left: Phase diagram of SnS_2-Cu_2S-ZnS system [22]. Right: Comparison of XRD peaks of CZTS, ZnS, and Cu_2SnS_3, the best know secondary phases

For the Cu_2S-ZnS-SnS_2 system, a single-phase CZTS crystal region still exists, which is very narrow according to the phase diagram in Figure 2.8. So, there is not much room to go off stoichiometry, making it a challenge to form CZTS [22]. The presence of slightly different stoichiometry immediately allows the formation of secondary phases, such as ternary and binary compounds, aside CZTS. It is clear from Figure 2.8 that one of the main routes to form CZTS starting from secondary phases is the reaction of Cu_2SnS_3 and ZnS. However, the formation of CZTS through binary phases, including Zn_xS, Cu_xS, Sn_xS, can also be applied for the growth of CZTS crystals. It is preferred that CZTS solar cells are slightly Zn-rich and Cu-poor, as explained in Section 2.2.3 . However, due to the small stoichiometric regimes in which CZTS is formed, the consequence is that secondary phases such as Cu_2SnS_3 and ZnS are also formed during growth within the Zn-rich regime. A negative attribution of these secondary phases is that they are presumed to contribute to lower efficiencies of the working solar cell. Therefore, detection of secondary phases can be an important parameter for generating a CZTS thin film. Nevertheless, detecting secondary phases using only XRD is practically impossible in CZTS and is not as straightforward as in CIGS. This is because kesterite CZTS shares multiple peaks with cubic ZnS and Cu_2SnS_3 as can be seen in Figure 2.8. To detect secondary phases Raman spectroscopy is often combined with XRD results to characterize CZTS thin films, because Raman spectroscopy allows us to

detect the important kesterite phases with a 532 nm laser. However, Raman analysis with this laser does not exclude the presence of secondary phases, because a laser of 325 nm is required to detect ZnS crystalline phases in Raman spectroscopy. Detecting the $Cu_xSn_xS_x$ phase can be more troublesome since the stoichiometry of this phase decides the peak position. Detecting pure CZTS can also be achieved using expensive, powerful synchrotron XRD or the use of extended X-ray absorption fine structure (EXAFS). [23]

2.5 Thin Film CZTS Deposition

In terms of fabricating CZTS thin film layers, we differentiate between vacuum and non-vacuum based methods. Vacuum methods are regarded as a physics approach of layer fabrication. Under vacuum conditions very controlled reactions can occur, which lead to very pure and crystalline materials. It is a technique in which atomic layer after layer can be deposited. These very controlled methods are highly desirable in the first attempts and fundamental research on making a certain material. However, the use of high vacuum and deposition in such a controlled way makes these methods slow and expensive compared to non-vacuum based methods, certainly when regarding large surface applications.
The non-vacuum based methods or the more chemical methods are considered less controlled. Here, a solution containing metals and/or NCs are deposited on a suitable substrate. Dependent on the composition of these solutions, a layer with a certain composition will be formed. The chemistry of these methods can be controlled by tuning the precursor solution, e.g. addition of organics, additives such as sodium or even an additional amount of material. The main advantage of these methods is that mostly large areas at one time can be covered. The disadvantage is that after the deposition only limited control is kept over the layer by choosing the right post layer treatment.
For materials such as CIGS and CdTe vacuum based methods have proven to be the best preforming methods in terms of resulting efficiency and are therefore regarded as ”the layer deposition-methods” [24]. However, CZTS shows a high tolerance towards structural and electronic defects in the final layer, which makes non-vacuum based methods the ideal and cheapest method for layer deposition. The best performing cell for CZTS has been fabricated using solution based processing [25].
In the sections below, the main deposition methods for CZTS will be discussed.

2.5.1 Vacuum Deposition

2.5.1.1 Evaporation

Evaporation is a well-known technique in the development of thin film solar cells. Here, a filament source is heated under high vacuum until evaporation occurs, the originating atoms travel in a straight line from the evaporation source towards a cold substrate forming a layer. In 2001, Katagiri et al. reported electron beam evaporation-deposited CZTS precursor films [11]. Additional sulfurization of the deposited film lead to the first CZTS solar cell with an efficiency of 0.66%. Evaporation involves two basic processes: evaporation and condensation of a hot source material on a substrate. For CZTS, Zn, Sn and Cu layers were sequentially deposited on Mo-coated soda lime glass substrates which were heated to 150 °C. The targeted composition ratio was decided by the thickness of metallic layers. Annealing at 500 °C in the atmosphere of N_2 + H_2S (5%) transformed the Cu/Sn/Zn stacked layers into a CZTS thin film. Variation in the different layers can be performed, such as the deposition of metal sulfides instead of metal atoms. Also the transformation process can be varied between sulfurization and selenization processes. All the reports showed that the conventional evaporation method is efficient for the development of CZTS TFPV. However, the industrial potential of thermal evaporation is limited compared to other techniques like sputtering [26].

2.5.1.2 Sputtering

Sputtering is a process in which atoms are ejected from a solid target material due to bombardment of the target by energetic particles. Depositing thin films by sputtering involves eroding a material from a ”target” source onto a ”substrate”, being a Mo coated sodium glass substrate in the case of CZTS. Sputtering allows uniform, large-area coatings, which is vital for solar cell production. Furthermore, it allows for targets and films with a large range of compositions, even non-stoichiometric, but it still requires a selenization step. However, the disadvantages of using the sputtering technique is that the conditions almost always guarantee high operating costs. As this takes place at high temperature and under vacuum (the annealing stage involving selenium vapor), the manufacturing costs are significant. Furthermore, as the components of a CZTS solar cell have different reaction rates, the reaction temperature must be set for the highest component (copper), but this high temperature affects the other three components. As such, secondary phases might be produced instead of CZTS; possible outcomes include a copper tin selenide (CTS) combination and a copper zinc selenide (CZS) version. It is currently used for the fabrication of CdTe and CIGS TFSC [27].

2.5.1.3 Pulsed Laser Deposition

Pulsed laser deposition (PLD) is a thin film deposition (specifically a physical vapor deposition, PVD) technique where a high-power pulsed laser beam is focused inside a vacuum chamber to strike a target of the material that is to be deposited (CIGS/CdTe/CZTS). This material is vaporized from the target (in a plasma plume) which is deposited as a thin film on a substrate [28]. This process can occur in ultra high vacuum or in the presence of a background gas, such as sulfur or selenium in the case of CIGS and CZTS. Without a background gas an extra selenization step is required.

2.5.2 Non Vacuum Depositions

2.5.2.1 Electrodeposition

Metal films were potentiostatically deposited at room temperature by dipping a conventional 3-electrode electrochemical cell with a platinum counter in a bath containing metal salts of $CuCl_2$, $SnCl_2$ and $ZnCl_2$ separately and also NaOH and sorbitol. A layer of Cu, Zn and Sn are deposited on the substrate, which can be done in different order and with different thickness to match the stoichiometry. The advantage is a that the manufacturing conditions are cheap. Disadvantages are that the layer is metallic and must be sulfurized or selenized to form a kesterite thin layer and that this process requires high atom mobility during the transformation of the different metallic layers to form CZTS. [29].

2.5.2.2 Sol-Gel Method

In this chemical procedure, a sol-gel formation process occurs. Here, a 'sol' (or solution) gradually evolves towards the formation of a gel-like di-phasic system containing both a liquid phase and solid phase whose morphologies range from discrete particles to continuous polymer networks. Generally, the sol is deposited on a substrate, after which the solvent is removed through drying of the layer. [30] The deposition of the sol can be performed through different techniques, e.g. spin-coating, dipcoating, inkjet printing, doctor blading, etc.
A CZTS precursor sol-gel was made by dissolving copper (II) acetate monohydrate, zinc (II) acetate dehydrate and tin (II) chloride dehydrate in a solution containing 2-methoxyethanol, deionized water and binder. Subsequently, the sol-gel was spin-coated on a Mo-coated soda lime glass substrates followed by drying at 300 °C on a hot plate. The coating and drying process were repeated several times to obtain thicker films. Again much like most solution based processes the fabrication conditions are cheap, such are the solvents and chemicals. Disadvantages are that mostly oxide films are formed and thus an additional annealing step is needed

to transform the layer in a dense crystalline film and to replace the oxygen by S or Se.

2.5.2.3 Solution based methods

For solution based methods generally atoms or ions are dissolved or coordinated in a solvent and deposited as an ink. The advantage is that stoichiometry can easily be tuned by simply dissolving more or less salt. In most cases solvents only allow limited dissolution of precursor material. But the most successful solvent in this approach has been hydrazine. Hydrazine is a volatile solvent which allows the high solubility of precursor material (Zn, Cu, Sn, S/Se salts). Without the presence of further contaminants thin films could be deposited and could be transformed into $+10\%$ efficient cells [25]. The only big disadvantage being that hydrazine is explosive and toxic.
For Solution based methods further coordinating molecules like dithio- or diselenocarbamates can be used to increase the metal salt concentration in less toxic solvents. These molecules also allow the introduction of S or Se in the layer [31]. After solution based process and a Se/S annealing step also here CZTS based absorber layers can be formed.

2.5.2.4 Nanoparticle-Based Method

CZTS nanocrystal-based approaches start with the controlled synthesis of nanocrystals and end with the deposition and post-treatment of films using the resulting inks. Compared with hydrazine-based processing, which uses the explosive solvent hydrazine during ink formation and film deposition, the preparation of CZTS nanocrystals only requires the involvement of common organic solvents and precursors. In addition, the capability of mass production of nanocrystals, together with their compatibility with ultrahigh throughput deposition techniques such as printing and casting, each of which are well established industrial procedures, enables CZTS nanocrystal based techniques for terawatt capacity module production [32].

Particles can be fabricated via 2 main approaches. The first approach is the top down approach. Particles can be formed by reducing the size of bulk material, using milling techniques, to form nanoparticles; the particles are typically insoluble, therefore difficult to process, and in the case of milling the size distribution may be large. The nanoparticles must be stabilized by organics to form a dispersion to be processed by screen printing [33]. The particles are still relatively big compared to the required layer and this results in a rough surface and low efficiency cells. A second approach is the bottom up approach. Particles originally synthesized using the hot injection method, but also alternative routes using heating up procedures and water based methods have been tried. In a typical synthesis, copper salt, zinc

salt, and tin salt are dissolved in the coordinating solvent oleylamine. The solution mixture is heated to 130 °C under inert atmosphere. The temperature is then raised to approximately 225 °C where mixture solution of sulfur and oleylamine is injected. The mixture is then cooled and purified to remove the organics from the mixture such as the excess of oleylamine. After centrifugation and decantation the particles can be redissolved to yield an already stabilized dispersion or ink. A whole range of inks and solvents can be used, together with different deposition techniques [34–36]. The synthesis allows the fabrication of CZTS and CZTSe which contain the kesterite crystal structure. High quality CZTS nanocrystals with well controlled size, shape, and chemical composition have been successfully synthesized. When starting from nanosized crystals we thus require a heat treatment for a reduction of grain boundaries by self healing and sintering in order to form a big crystalline CZTS layer. However, the kesterite crystal phase is already a very stable phase and thus can lack the driving force to transform into bigger crystallites.
Therefore also binary and ternary synthesis methods can be developed to form the desired kesterite phase. Here the particles need to sinter to form a more stable form, which could be kesterite, giving a new driving force for further densification. And of course here also an additional annealing procedure has to be performed to grow the CZTS nanocrystals into a dense crystalline CZTS thin films.
The main challenges of this technique are the topic of this thesis. In following chapters we will explore the synthesis of possible CZTS nanocrystals as thin film precursor. The formation of a nanocrystal ink and thin film deposition, and finally the transformation of the nanocrystal film into a dense crystalline CZTS film.

Bibliography

[1] C. M. Evans, L. C. Cass, K. E. Knowles, D. B. Tice, R. P. H. Chang, and E. A. Weiss, "Review of the synthesis and properties of colloidal quantum dots: the evolving role of coordinating surface ligands," *Journal of Coordination Chemistry*, vol. 65, no. 13, pp. 2391–2414, 2012.

[2] J. Perlin, *From Space to Earth: The Story of Solar Electricity*. Aatec Publications, 1999.

[3] K. Zweibel, "Thin films: past, present, future," *Progress in Photovoltaics: Research and Applications*, vol. 3, no. 5, pp. 279–293, 1995.

[4] W. Shockley and H. J. Queisser, "Detailed Balance Limit of Efficiency of pn Junction Solar Cells," *Journal of Applied Physics*, vol. 32, no. 3, 1961.

[5] J. I. Pankove, *Optical processes in semiconductors*. Courier Dover Publications, 2012.

[6] C. Wadia, A. P. Alivisatos, and D. M. Kammen, "Materials Availability Expands the Opportunity for Large-Scale Photovoltaics Deployment," *Environmental Science & Technology*, vol. 43, no. 6, pp. 2072–2077, 2009.

[7] K. L. Chopra, P. D. Paulson, and V. Dutta, "Thin-film solar cells: an overview," *Progress in Photovoltaics: Research and Applications*, vol. 12, no. 2-3, pp. 69–92, 2004.

[8] J. Caplan, "Best Inventions of 2008," *Time Magazine*, 2008.

[9] M. J. Yan and Xingzhong, "Cu2ZnSnS4 Thin Film Solar Cells: Present Status and Future Prospects," in *Solar Cells - Research and Application Perspectives Title*, 2013.

[10] W. Van Sark, G. W. Brandsen, M. Fleuster, and M. P. Hekkert, "Analysis of the silicon market: Will thin films profit?," *Energy Policy*, vol. 35, no. 6, pp. 3121–3125, 2007.

[11] H. Katagiri, N. Ishigaki, T. Ishida, and K. Saito, "Characterization of Cu 2 ZnSnS 4 Thin Films Prepared by Vapor Phase Sulfurization," *Japanese Journal of Applied Physics*, vol. 40, no. 2R, p. 500, 2001.

[12] F. Kohler, T. Zimmermann, S. Muthmann, A. Gordijn, and R. Carius, "Structural Order and Staebler #x2013;Wronski Effect in Hydrogenated Amorphous Silicon Films and Solar Cells," *Photovoltaics, IEEE Journal of*, vol. 4, pp. 4–9, Jan. 2014.

[13] R. Nitsche, D. Sargent, and P. Wild, "Crystal growth of quaternary 122464 chalcogenides by iodine vapor transport," *Journal of Crystal Growth*, vol. 1, pp. 52–53, Jan. 1967.

[14] W. Schäfer and R. Nitsche, "Tetrahedral quaternary chalcogenides of the type cu¡ sub¿ 2¡/sub¿ ii iv s¡ sub¿ 4¡/sub¿(se¡ sub¿ 4¡/sub¿)," *Materials Research Bulletin*, vol. 9, no. 5, pp. 645–654, 1974.

[15] X. Lu, Z. Zhuang, Q. Peng, and Y. Li, "Wurtzite Cu2ZnSnS4 nanocrystals: a novel quaternary semiconductor," *Chem. Commun.*, vol. 47, no. 11, pp. 3141–3143, 2011.

[16] S. Chen, X. G. Gong, A. Walsh, and S.-H. Wei, "Crystal and electronic band structure of Cu2ZnSnX4 (X=S and Se) photovoltaic absorbers: First-principles insights," 2009.

[17] J. J. S. Scragg, L. Choubrac, A. Lafond, T. Ericson, and C. Platzer-Bjrkman, "A low-temperature order-disorder transition in cu2znsns4 thin films," *Applied Physics Letters*, vol. 104, no. 4, pp. –, 2014.

[18] P. A. Fernandes, P. M. P. Salomé, and A. F. Da Cunha, "Growth and Raman scattering characterization of Cu2ZnSnS4 thin films," *Thin solid films*, vol. 517, no. 7, pp. 2519–2523, 2009.

[19] D. M. Berg and P. J. Dale, "Kesterites: Equilibria and secondary phase identification," *Copper Zinc Tin Sulfide-Based Thin Film Solar Cells*, p. 107, 2014.

[20] S. Chen, A. Walsh, X.-G. Gong, and S.-H. Wei, "Classification of Lattice Defects in the Kesterite Cu2ZnSnS4 and Cu2ZnSnSe4 Earth-Abundant Solar Cell Absorbers," *Advanced Materials*, vol. 25, no. 11, pp. 1522–1539, 2013.

[21] K. Orgassa, H. W. Schock, and J. Werner, "Alternative back contact materials for thin film cu (in, ga) se¡ sub¿ 2¡/sub¿ solar cells," *Thin Solid Films*, vol. 431, pp. 387–391, 2003.

[22] V. Tomashyk, *Quaternary Alloys Based on II - VI Semiconductors*. CRC Press, 2014.

[23] K. Hartman, B. K. Newman, J. L. Johnson, H. Du, P. A. Fernandes, V. Chawla, T. Bolin, B. M. Clemens, A. F. da Cunha, G. Teeter, M. A. Scarpulla, and T. Buonassisi, "Detection of ZnS phases in CZTS thin-films by EXAFS," in *Photovoltaic Specialists Conference (PVSC), 2011 37th IEEE*, pp. 2506–2509, 2011.

[24] M. A. Green, K. Emery, Y. Hishikawa, W. Warta, and E. D. Dunlop, "Solar cell efficiency tables (version 39)," *Progress in photovoltaics: research and applications*, vol. 20, no. 1, pp. 12–20, 2012.

[25] T. K. Todorov, J. Tang, S. Bag, O. Gunawan, T. Gokmen, Y. Zhu, and D. B. Mitzi, "Beyond 11% efficiency: Characteristics of state-of-the-art cu2znsn (s, se) 4 solar cells," *Advanced Energy Materials*, vol. 3, no. 1, pp. 34–38, 2013.

[26] H. Katagiri, K. Jimbo, W. S. Maw, K. Oishi, M. Yamazaki, H. Araki, and A. Takeuchi, "No Title," *Thin Solid Films*, vol. 517, p. 2455, 2009.

[27] K. Ito and T. Nakazawa, "Electrical and Optical Properties of Stannite-Type Quaternary Semiconductor Thin Films," *Japanese Journal of Applied Physics*, vol. 27, no. 11R, p. 2094, 1988.

[28] K. Moriya, K. Tanaka, and H. Uchiki, "Fabrication of Cu 2 ZnSnS 4 Thin-Film Solar Cell Prepared by Pulsed Laser Deposition," *Japanese Journal of Applied Physics*, vol. 46, no. 9R, p. 5780, 2007.

[29] J. J. Scragg, P. J. Dale, L. M. Peter, G. Zoppi, and I. Forbes, "New routes to sustainable photovoltaics: evaluation of Cu2ZnSnS4 as an alternative absorber material," *physica status solidi (b)*, vol. 245, no. 9, pp. 1772–1778, 2008.

[30] M. Jiang, Y. Li, R. Dhakal, P. Thapaliya, M. Mastro, J. D. Caldwell, F. Kub, and X. Yan, "Cu2ZnSnS4 polycrystalline thin films with large densely packed grains prepared by sol-gel method," *Journal of Photonics for Energy*, vol. 1, no. 1, pp. 19501–19506, 2011.

[31] Y. Cao, J. Catron, L. Johnson, M. Lu, I. Malajovich, and D. Radu, "Molecular precursors and processes for preparing copper indium gallium sulfide/selenide coatings and films," Oct. 10 2013. US Patent App. 13/885,105.

[32] V. A. Akhavan, B. W. Goodfellow, M. G. Panthani, C. Steinhagen, T. B. Harvey, C. J. Stolle, and B. A. Korgel, "Colloidal CIGS and CZTS nanocrystals: A precursor route to printed photovoltaics," *Journal of Solid State Chemistry*, vol. 189, pp. 2–12, 2012.

[33] Z. Zhou, Y. Wang, D. Xu, and Y. Zhang, "Fabrication of cu_2znsns_4 screen printed layers for solar cells," *Solar Energy Materials and Solar Cells*, vol. 94, no. 12, pp. 2042–2045, 2010.

[34] Q. Guo, H. W. Hillhouse, and R. Agrawal, "Synthesis of Cu2ZnSnS4 Nanocrystal Ink and Its Use for Solar Cells," *Journal of the American Chemical Society*, vol. 131, no. 33, pp. 11672–11673, 2009.

[35] S. C. Riha, B. A. Parkinson, and A. L. Prieto, "Solution-Based Synthesis and Characterization of Cu2ZnSnS4 Nanocrystals," *Journal of the American Chemical Society*, vol. 131, no. 34, pp. 12054–12055, 2009.

[36] A. Shavel, D. Cadavid, M. Ibáñez, A. Carrete, and A. Cabot, "Continuous Production of Cu2ZnSnS4 Nanocrystals in a Flow Reactor," *Journal of the American Chemical Society*, vol. 134, no. 3, pp. 1438–1441, 2012.

Part I

Synthesis Of Nanocrystals

3

Introduction To Nanocrystal Synthesis

3.1 Building Nanocrystals From Atoms Up

A wide variety of bottom-up syntheses of nanocrystals are based on the same basic principle first described by La Mer and Dinegar in 1950 [1]. Their findings were based on the preparation of a monodisperse sulfur hydrosol by the slow decomposition of dilute sodium thiosulfate in dilute hydrochloric acid. A hydrosol is a colloidal dispersion made of oils as well as water soluble components that generate compounds that we will call 'monomers'. These monomers are the building blocks of the colloidal particles that will be formed.
This concept is explained with the help of Figure 3.1a. When the monomers are released in solution, by means of injection or decomposition of chemicals, their concentration will initially be below the solubility limit. Thus nothing but dissolution will occur. If the monomer concentration keeps increasing the solubility will be exceeded, but even when the solubility limit is slightly exceeded, nothing will occur. Only when the 'nucleation threshold '(indicated on Figure 3.1a) is exceeded monomers will start to 'nucleate', also called the nucleation regime. This comes down to the formation of really small clusters of the final compound, or seeds, that will grow to become the final particles. At a certain amount of cluster formation, the monomer concentration will drop below the concentration of the nucleation threshold, preventing more clusters from forming. Although the monomer concentration dropped below the nucleation threshold, it is still above the solubility of the monomer. This means that the remaining monomers will be available for

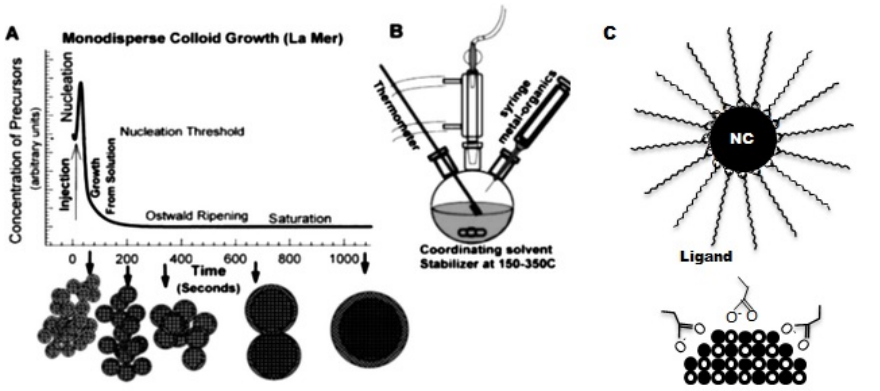

Figure 3.1: (A) A schematic view on the La Mer growth model showing the start of a particle reaction and its evolution over time. After injection the nucleation starts, followed by growth and eventually ending in ripening. (B) A visual representation of the setup used in the hot injection synthesis. A 3-neck flask with magnetic stirrer, cooler, thermometer and injection needle. (C) A visual representation of a sterically stabilized colloidal NC. [2].

the growth of the existing particles. This is the growth regime. Now, if the nucleation regime is only exceeded for a short time, only a small amount of cores will be formed. This means that still a lot of monomers are available for each core to grow bigger, resulting in a small amount of big particles. A longer exposure of the nucleation regime yields the opposite, a greater amount of cores, and less material for those cores to grow bigger. One great benefit of the growth regime is that the monomers are favorable to 'grow' on the smallest particles, resulting in a focusing of the particle size. Once the solubility of the monomers is reached the particles will stop growing and the maximum yield of the synthesis has been reached. At this point, the ripening regime starts. Thermodynamically less stable smaller particles will dissolve in favor of the bigger particles. This can be used to generate even larger particles, but has a negative outcome on the size distribution. A synthesis can be stopped at any given point depending on the desired particle size.

3.2 The Theory Applied

The La Mer model is a general picture on the formation of small, mostly nanocrystals (NCs) that can be applied in different solvents and with different chemical formulations [1]. The variant we will be using is one introduced by Murray et al. [3]. Both proposed a synthesis for sterically stabilized colloidal NCs and the method that is generally used to generate these crystals is called the hot injection method. Hot injection refers to the way the supersaturation limit of the La Mer model is

surpassed in the synthesis. A metal chalcogenide supersaturation is created by rapidly injecting a precursor (e.g. a chalcogenide) in a hot mixture (e.g. a metal salt solution). This in turn will induce nucleation followed by growth. The benefit of this technique is that many parameters can be controlled to achieve the desired product. First of all in hot injection synthesis the 'hot' refers to the temperature of the solution in which the reaction occurs. Most of the time a 3-neck flask is used with a Liebig cooler, a thermometer and an injection needle, see Figure 3.1b. Temperatures used range between 100 and 320 °C, depending on the synthesis. Thus temperature, reactants concentration, synthesis time and injection speed all have effects on the reaction speed, yield, crystal structure and final size of the product.
Furthermore, the word steric has an important meaning for this methodology. NC are kept in suspension using steric stabilization. This form of stabilization mostly uses long carbon chains that cover a NC surface, generating a repulsive effect between the NCs which is generally an entropic effect. A typical representation of a stabilized NC is shown in Figure 3.1c. Steric stabilization works best in solvents that show great affinity with the atoms on the surface of the NC. The molecule that allows this kind of stabilization is called a 'ligand'. Typical examples from the research field of NCs are trioctylphosphine, oleic acid or oleylamine [3–5]. These ligands work well in non-polar organic solvents. However, a very wide variation is available, allowing dispersion in different solvents, even polar solvents. Next to keeping the NCs in suspension, the ligands also play a vital role in most hot injection syntheses. These ligands can complex metal atoms allowing their dissolution. When forming clusters these atoms will also be present on the surface of the crystal and in some cases only on a preferred orientation of the NC. This gives them in some cases a crucial role in the formation of the NCs. This can mean that changing the ligand can have influences on the morphology and size of the NCs. However, this subject is still ongoing research and is not the main goal of this thesis.
So, all these parameters give the hot injection synthesis an exceptional combination of a precise synthesis method with a lot of versatility. This is exactly the combination we are looking for in the case of semiconductor NCs or quantum dots (QDs), because for QDs the size and the size distribution are of utmost importance. It allows synthesis of various II-VI [3, 6, 7], IV-VI [5, 8, 9] and III-V [10, 11] semiconductors with excellent control over size, shape and composition. Because the NCs are solution-processable materials (due to the ligands on the NCs) with tunable optical properties, they can be used in a wide range of possible applications. There use has been shown in photovoltaics [12], lighting and display applications [13], photo detection [14] and fluorescent labeling [15].

4

CdSe Synthesis As Synthesis Model

Back in 2010 when I finished my master thesis at the PCN group of professor Hens, cadmium selenide NCs were by far the most popular NCs emitting in the visible spectrum. Emmiting CdSe quantum dots can be used to make LEDS or can be used in biolabeling. Within the group, a lot of research had been performed on the topic of synthesis of NCs. The CdSe NCs were synthesized in 3 or 4 different ways, all for their good reasons. Wurzite CdSe formed the starting material to synthesize CdSe/CdS nanorods by seeded growth whereas zincblende CdSe NCs were typically used for the formation of CdSe/CdS core/shell quantum dots by the SILAR method. A multitude of synthesis routes has its advantage that a NC with specific properties can be obtained, but each of the methods used also has important disadvantages.

When we take a look in literature, the used Se-precursors are in most cases expensive or toxic [3]. The precursors are shown in Figure 4.1. Both the bis-(trimethylsilyl)selenide and the trioctylphosphine selenide are highly toxic and combustive in contact with oxygen and need careful handling. There are safer alternatives but those result in a slow and low yield synthesis [4]. Moreover, as the use of the CdSe NCs increased, the demand for larger quantities and hence for an up-scaling of QD syntheses has emerged over the last years [16], thus we searched for a safe and fast Se precuror. Therefore we took the opportunity to search for a synthesis using cheap precursors, a fast reaction and high yields. In this chapter we propose an alternative approach to synthesize these CdSe NCs, via hot injection synthesis, in a cheap and fast manner and a yield near 80% using a new Se precursor. We even show that the development of this new Se-precursor opened

the door to the improvement of other types of NCs synthesis (even for the CZTS family).

4.1 A Novel Selenium Precursor

The CdSe NC that have been synthesized are emitting within the whole visible spectrum and can be used in applications such as LEDS or photodetectors. The research focus concomitantly shifted to methodology development, which includes the search for optimized approaches in terms of large scale batch reactors or continues flow-line approaches but also a re-evaluation of reagents and reaction conditions. This in combination with tuneability of their size at full yield and synthesis reproducibility, which have become key issues in the CdSe NC synthesis.
The original CdSe synthesis by Murray et al. [3] made use of dimethyl cadmium and bis(trimethylsilyl)selenium or selenium dissolved in trioctylphosphine, which are all expensive chemicals that are difficult to handle (pyrophoric, oxygen sensitive) and require specific reaction conditions and safety procedures. The molecular structures are shown in Figure 4.1. Later, Qu et al. [17], showed that CdSe NCs can be synthesized using less hazardous cadmium precursors, obtained by dissolving common cadmium salts or cadmium oxide in an organic solvent using carboxylic or phosphonic acids as a complexing agent. Alternative selenium precursors on the other hand are rare. Jasieniak et al. [4] demonstrated the formation of CdSe QDs using elemental black selenium dissolved at elevated temperatures in octadecene (ODE). However, while black selenium is cheap and easy to handle, the formation of CdSe NCs based on this homogeneous ODE-Se precursor is slow and does not reach - opposite from TOP-Se based syntheses - full yield. Moreover, the limited solubility of selenium in ODE makes that a relatively high amount of solvent is needed to synthesize a given weight of CdSe NCs, a ratio we refer to as the solid loading of the synthesis. Alternative water-based syntheses have been developed as well, yet these procedures typically lead to dispersions with a larger size dispersion and have, in case numbers are given, a relatively low reaction yield. The dissolved Se in ODE shows a big batch to batch variation in the CdSe synthesis. We believe that the dissolution of Se in ODE occurs in different steps and depending on the temperature and time the Se dissolution got exposed to in a different reactivity occurs and thus leads to difficulties in reproducibility. Which is very important for these strongly size depending materials.
We propose an alternative approach to synthesize cadmium selenide NCs using a selenium precursor that combines the high reactivity of TOP-Se with the ease-of-use of homogeneously dissolved selenium. The method involves the injection of black selenium powder, heterogeneously dispersed in a carrier liquid in a reaction flask holding an inert solvent such as ODE or an other high boiling solvent, a cadmium carboxylate complex and excess carboxylic acid at elevated tempera-

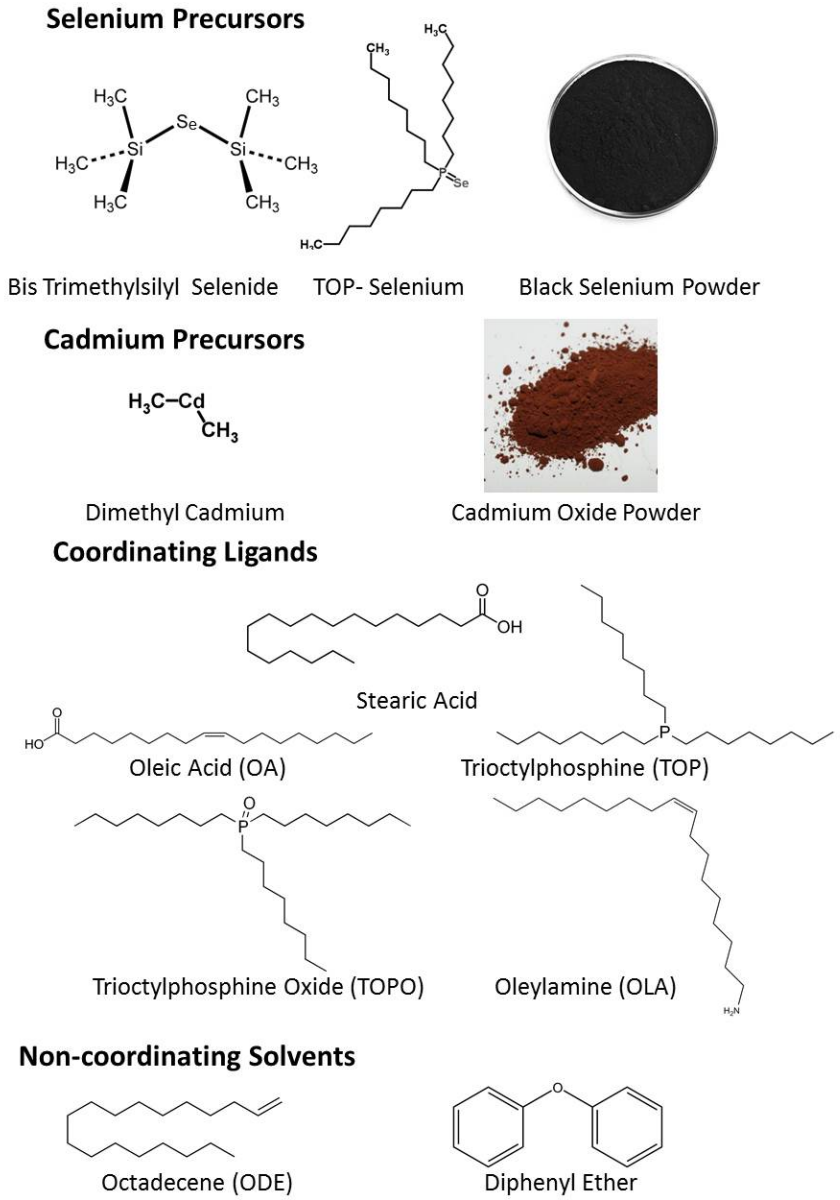

Figure 4.1: An overview of the most common precursors, ligands and solvents used in CdSe quantum dot synthesis.

ture. We show that this injection leads to the formation of CdSe NCs, with yields as high as 80-85% and reaction times as short as 5 minutes. The NC diameter obtained at the end of the reaction can be adjusted by the reaction conditions, where larger NCs are obtained by reducing the chain length of the carboxylic acids used. Furthermore, the reaction can be executed under air, without compromising the quality of the end product and 50 mg of NCs can be formed per mL of solvent. We also demonstrate that the synthesis can be reproducibly executed using an automated liquid handler, thus demonstrating the feasibility of using heterogeneous dispersions of black selenium powder for the scaled up synthesis of metal selenide NCs. Furthermore, a CdS shell is grown onto the CdSe core to reduce the dangling bounds and improve the photoluminescence quantum yield, to compare the properties of the CdSe NCs via our approach to the state-of-the-art CdSe crystals. Finally, we tested the widespread of this method, by synthesizing ZnSe via the replacement of the cadmium precursor to the zinc precursor.

4.1.1 Metal Selenide Nanocrystal Synthesis

For a standard synthesis of CdSe, we add cadmium oxide (CdO, 0.4 mmol) to 10 mL of octadecene (ODE) mixed with 1.2 mmol of oleic acid in a three neck flask (Cd1 mixture). Note that other carboxylic acids, such as dodecanoic, myristic, palmitic, stearic, behenic or oleic acid can be used as well. The amount of CdO can be varied from 0.05 mmol up to of 8 mmol, keeping the acid to cadmium ratio at 3:1 and fixing the volume of ODE at 10 mL. A cooler was placed in the central neck, while a thermometer and a top with a septum was placed in each of the side-necks. The outlet of the cooler is left open to air. After heating Cd1 mixture to 250 °C, the red CdO dissolves to form a colorless Cd carboxylate complex. We prepared the Se precursor by dispersing elemental black selenium powder ($\leq$200 mesh) in 1 mL of ODE. For the standard synthesis, we use 0.2 mmol of Se (Se mixture). The amount of Se can be varied, keeping the Cd:Se ratio between 1:1 and 1:0.05. Injection mixtures of Se that exceeds the 1:1 ratio causes to precipitate the crystals.
The synthesis of CdSe NCs will start when injecting the Se mixture in the Cd1 mixture. We set the temperature of the Cd1 mixture at the injection temperature of 270°C. The Se mixture needs to be vigorously stirred to prevent settling of the Se powder before it is loaded in a syringe and quickly injected it in the Cd1 mixture. The temperature of the reaction mixture drops to 260 °C. Upon injection, the black color of the Se precursor disappears and the color of the reaction mixtures turns from yellow to orange to red depending on the formed size of the NCs. We stop the reaction after 5-10 minutes by external thermal quenching using a water bath at room temperature followed by the injection of 10 mL of toluene.
Note that for safety reasons the synthesis is done under nitrogen atmosphere since

the flashpoint of ODE is 250 °C. The presence of oxygen has no effect on the synthesis itself, therefore no heavy flushing is required.

ZnSe NCs are synthesized in a similar way compared to CdSe, starting from zinc carbonate basic $Zn_5.2(CO_3).6(OH)$, 0.08 mmol), 10 mL ODE and 1.2 mmol of oleic acid (Zn mixture) in a three neck flask with cooler, septum and thermometer. This Zn mixture is heated to 250 °C, the dissolution of the zinc carbonate takes place, forming a colorless Zn carboxylate complex. The synthesis of ZnSe NCs starts with the injection of the Se mixture in the hot Zn mixture and proceeds as in the synthesis of CdSe. The color change is different due to the bandgap of the material and goes from colorless to yellow to orange. The reaction is again stopped after 5-10 minutes in the same way as the CdSe reaction was stopped.
The NC mixtures (either CdSe or ZnSe) are purified by adding isopropanol and methanol, each in a 1:1 ratio relative to the toluene already added when the reaction mixture was cooled after synthesis. Subsequently we centrifuge at 2000 g and decant the clear supernatant from the pellet of NCs that can be redispersed in toluene.
Prior to a second purification step, we add oleic acid in a 3:1 ratio relative to the amount of acid originally used in the synthesis to replace the original carboxylic acid on the surface of the NCs. The purification step is repeated twice using respectively 4 mL of toluene as solvent and 8 mL of methanol and non-solvent to remove all residual reaction products. Finally, the NCs are dispersed in 4 mL of toluene.

4.1.2 CdS Shell Growth

Core/shell CdSe/CdS NCs can be obtained by adapting the synthesis developed by Li et al. [18]. First we prepare a S precursor by dissolving 1 mmol of sulfur in 10 mL of ODE at 100 °C (S mixture) and a Cd precursor by dissolving 1.38 mmol of CdO in 12 mmol of oleic acid and 10 mL of ODE and heat the mixture to 250 °C until complete dissolution of the CdO (Cd2 mixture). Next, 0.68 μmole of CdSe NCs are dispersed in 1 L of hexane. The synthesis mixture is prepared by adding 1.5 g of n-octylamine and 12 mL of ODE to a three neck flask and flushing this solution under nitrogen while stirring at 100 °C for 1 hour. Afterwards, the prepared CdSe dispersion is injected in this reaction mixture, and the temperature of this reaction mixture is raised to 225 °C. A CdS shell is grown by a successive ion layer addition and reaction procedure also called SILAR.
It is possible to calculate the amount of sulfur and cadmium precursor needed to grow one additional monolayer of CdS around the NC, presuming that the crystals are monodisperse. For this, the diameter of the NCs and their amount in the reaction mixture must be known. To calculate the amount of precursor needed

by starting from the volume of the core – in the case of 2.7 nm CdSe NCs, this amounts to 10.3 nm^3 - and compare it to the volume of the NCs after adding one monolayer – growing 1 CdS shell adds 0.6 nm to the NC diameter, such that a final volume of 18.8 nm^3 is obtained for the example given. Calculate the shell volume by subtracting both volumes, yielding 8.5 nm^3 for the example given. Calculate the total shell volume required for 1 growth circle by multiplying this number with the amount of NCs in the reaction mixture. With 0.68 μmole of NCs, this amounts to a volume of 0.0033 cm^3. Divide the shell volume by the molar volume of CdS to obtain the amount of precursor needed. With a molar volume of 29.7 cm^3/mol, we obtain in the example given 0.12 mmol of Cd and S. This comes down to 1.2 mL of the solutions prepared in at the start called the S and Cd2 mixture.
To grow the shell we add 1.2 mL of the S mixture to the reaction mixture and let it react for 10 minutes. Subsequently, we add 1.2 mL of the Cd2 mixture and again let it react for 10 minutes. We alternate these injections until the desired shell thickness is grown. Note that you always use the newly obtained diameter for calculating the amount of precursor needed for the next shell. After the desired amount of shells has been formed, we stop the reaction by quenching with a water bath at room temperature and add 5 mL of toluene. Purification of the mixture can be done as described before.

4.1.3 Materials Characterization

To analyze the quality of the synthesized NCs, we applied different characterization steps.
Absorption spectroscopy is applied for a first indication of the NC diameter, size dispersion and NC concentration. To obtain the spectrum, the synthesized NCs are diluted 200 times in 3 mL of toluene. Measuring the spectrum works best using a quartz cuvette that has a clear window between 750 nm and 280 nm. For analyzing the absorption spectra, a zinc blende CdSe sizing curve is used to determine the NC diameter and size dispersion, while the extinction coefficients of zinc blende CdSe is used to determine the NC concentration [19].
X-ray diffraction (XRD) can be applied to determine the crystal structure of the NCs. An XRD sample was prepared by dropcasting a dispersion of QDs in an 80:20 hexane:heptane mixture on a silicon or glass substrate. Typically, this requires taking 200 μL of the purified NC solution. For an X-ray diffractogram we measure in the 2θ range from 20 to 60 degrees.
Transmission electron microscopy (TEM) is used to analyze the shape, diameter and size dispersion of the NCs. We prepare a TEM sample by dropcasting a NC solution on a carbon coated copper grid and let it dry. Typically, this requires 50 μL of a 200-fold dilution of the purified NC solution obtained after purification. Note that these are indicative numbers. The exact amount needed for a good NC

density on the TEM grid will depend on the size and the concentration of the NCs in the obtained dispersion.
^{1}H-Nuclear Magnetic Resonance (^{1}H-NMR) is used to monitor the ligands bound the surface of the quantum dots. The bound ligand molecules will have less rotational freedom resulting in broadening of the peaks signal, making it possible to distinguish between unbound and bound molecules onto the surface. This can be performed in combination with quantitative measurements, which allows us to determine the ligand concentration on the NCs. Experimentally this means that 1 mL of the solution as obtained after the purification is dried, followed by the redispersion of this dry residue in 1 mL of toluene-d8 to obtain a ^{1}H-NMR sample.

4.2 Metal Selenide Nanocrystals: Results

4.2.1 Time Development of the CdSe Synthesis

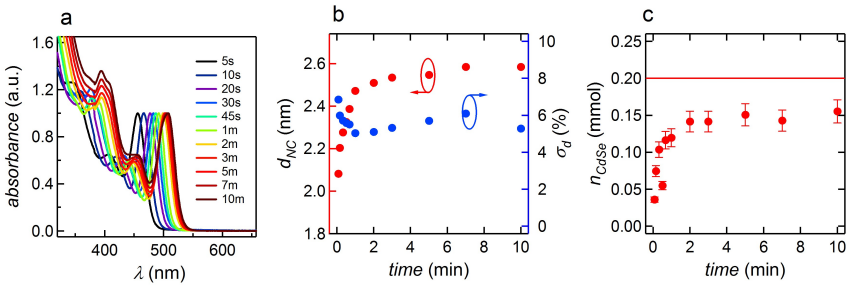

Figure 4.2: Time development of the CdSe synthesis (a) Absorption spectra recorded on aliquots taken at the time indicated after the injection of black selenium powder in mixture of cadmium oleate (0.4 mmol), excess oleic acid (0.4 mmol) and octadecene (10 mL) at 270 °C. The progressive redshift of the absorption peak of the first exciton transition is indicative of the formation and growth of CdSe NCs. (b) Time development of the CdSe NC diameter and size dispersion as calculated from the peak wavelength and the width of the first exciton transition of the respective aliquots. It can be seen that NC growth levels off after 3-5 mins of reaction time. (c) Amount of CdSe formed as a function of time. In line with the evolution of the NC diameter, a constant yield of 70-80% in this case is obtained after 3-5 minutes of reaction time. The full red line indicates the 100% yield level.

Figure 4.2 summarizes the time development of the main characteristics of CdSe QDs synthesized by injecting a standard amount of black selenium powder in a reaction mixture containing a standard amount of cadmium oleate acid and excess oleate in ODE (see protocol). The UV-Vis absorption spectra of aliquots taken between 5 seconds and 10 minutes after the injection (Figure 4.2a) show the succession of peaks and shoulders that are characteristic of CdSe QDs with a narrow size distribution. Hereby, the maximum wavelength $\lambda_{^1S_e-^1S_h}$ and the width

of the first exciton transition makes a detailed analysis of the NC diameter (d_{NC}) and the size dispersion *d* respectively possible. Whereas the absorbance at 300 nm allows for the determination of the amount of CdSe (n_{CdSe}) formed during the reaction. As shown in Figure 4.2b, the diameter of the CdSe NCs rapidly increase after injection and remain steady at 2.5-2.6 nm after 3 minutes of reaction. At the same time, the size distribution remains low, at about 5-6%, while the amount of formed CdSe levels off at 0.15 mmol, corresponding to a reaction yield of 70-80% as shown in Figure 4.2c. Similar results, with yields reaching up to 85%, are obtained when using different precursor concentrations or carboxylic acids and when working either under protective atmosphere or using a saturated hydrocarbon such as hexadecane (HDA) as an alternative solvent. To determine the unreacted selenium, XRF measurements have been performed on the supernatant obtained after separating the NCs from the reaction mixture. We find that 11.3% of the selenium added to start the reaction can be retrieved as unreacted selenium dissolved in the reaction supernatant.

4.2.2 Properties of the CdSe Nanocrystals

The main materials properties, determined using CdSe quantum dots synthesized and purified using the standard synthesis procedure with myristic acid as the carboxylic acid are represented in Figure 4.3.

The UV-Vis absorption spectrum (Figure 4.3a) shows that this results in CdSe quantum dots with a $\lambda_{^1S_e-^1S_h}$ of 543 nm, which corresponds to a diameter of 3.1 nm. This conclusion is confirmed by a TEM micrograph (see Figure 4.3b), which shows that quasi-spherical NCs are formed with an average diameter of 3.0 nm and a size dispersion of 6.7%. According to the X-ray diffractogram, these NCs have the crystal structure of zinc blende CdSe (Figure 4.3c). Similar to many other binary NCs, such as CdSe, CdTe, PbSe and PbS, the use of this black Se precursor leads to CdSe NCs that are cation rich [19, 21, 22]. This follows from the ratio of the Z^2 (Z=atomic number) corrected RBS signal (Figure 4.3d), which yields a Cd:Se ratio of 1.22.

Figure 4.3e represents the quantitative ^{1}H NMR spectrum obtained from the purified reaction product - i.e., involving a ligand exchange to oleic acid - dispersed in toluene-d8. Similar to previously published results on CdSe, PbSe and PbS NCs [19, 21, 22], the spectrum contains the broad resonances characteristic of bound oleate ligands (Figure 4.3e) next to the sharp resonance of residual toluene-d8 (†). The ratio between the integrated intensity of the resonance of the alkene protons of oleic acid at 5.6 ppm and the methyl protons at 1.0 ppm protons amounts to 2:3.3, indicating that at the most 10% of the original myristic acid ligands used in the synthesis - which only contributes to the methyl proton resonance - remain

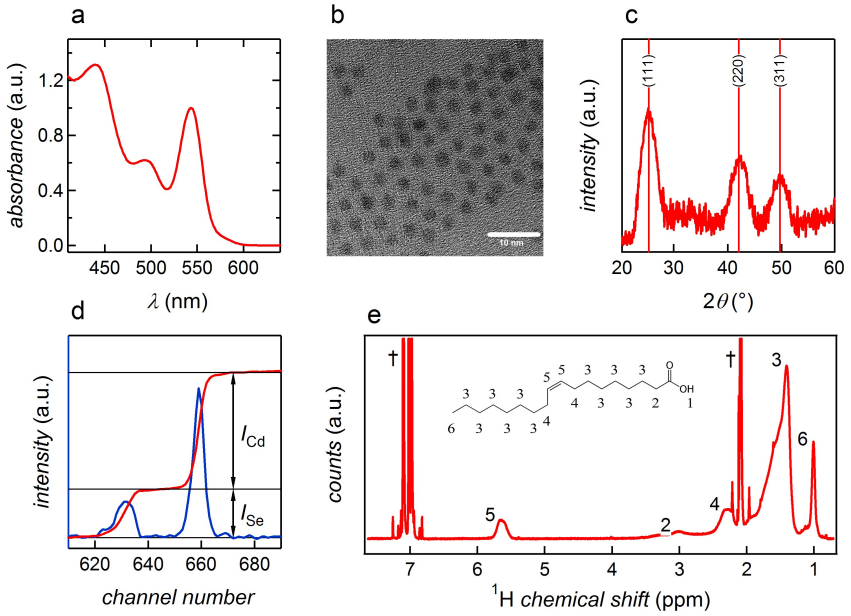

Figure 4.3: The synthesis used for the basic characterization of NC morphology, crystal structure, composition and surface chemistry has been executed under standard conditions of concentrations and temperatures, using myristic acid as the carboxylic acid. (a) absorption spectrum of the reaction product when stopping the reaction after 5 min. The position of the first exciton peak corresponds to a NC diameter of 3.1 nm. (b) Bright field TEM image. The scale bar corresponds to 10 nm. Size analysis on several micrograph pictures yields an average diameter of 3.0 nm and a size dispersion of 6.7%. (c) XRD pattern in combination with (vertical bars) the expected reflections for zinc blende CdSe. (d) Rutherford back-scattering spectrum indicating (blue) back-scattering of He^+ ions by Se and Cd, respectively and (red) the integrated intensity used to calculate the Cd/Se ratio.(e) ^{1}D-^{1}H NMR spectrum of a dispersion of purified CdSe NCs including a ligand exchange to oleic acid. Indicated are the resonances of (2-6) bound oleate and † residual toluene-d8. There is no indication of leftover free oleic acid. See Moreels et al. [20] for more details on the resonance assignment.

after the oleic acid ligand exchange step in the purification procedure. From the same quantitative experiment, we obtain a ligand density of 3.4 nm^2 based on the methyl resonance. In combination with the Cd:Se ratio as determined by RBS and the NC diameter, this yields a Cd:OA ratio of 1:2 for the cadmium atoms in excess. Hence, as previously found for CdSe NCs stabilized by oleate or phosphonate ligands, we conclude that the (positive) charge on the excess cadmium is balanced by the (negative) charge on the anionic ligands.

4.2.3 CdS Shell Growth

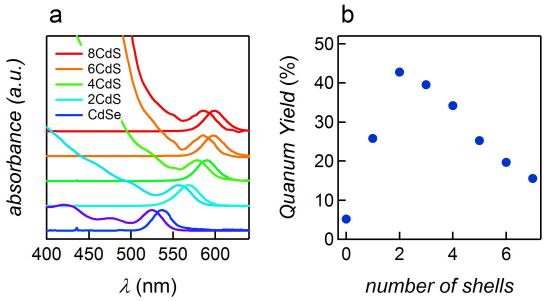

Figure 4.4: Time development of the CdSe synthesis (a) Variation of the absorbance and photoluminescence spectra of CdSe/CdS core/shell NCs, grown using a SILAR procedure starting from CdSe cores synthesized under air by the hot injection of black selenium powder. The legend indicates the number of CdS shells grown for each couple of spectra. (b) Photoluminescence quantum yield of CdSe/CdS NCs as a function of the number of shells grown.

Generally, the photoluminescence quantum yield (PLQY) of CdSe core NCs is relatively low. For CdSe QDs synthesized under air using black selenium powder, we measure typical values after purification between 5 and 10%. In line with their low size dispersion, the PL spectra are narrow (see Figure 4.4) , typically showing a full width at half maximum of about 30 nm. Like with previously synthesized CdSe NCs,the PLQY of CdSe NCs synthesized using black selenium powder under air can be enhanced by shell growth. Figure 4.4a shows the evolution of the absorption and PL spectra when a successive ion-layer adsorption and reaction (SILAR) approach is used to grow a CdS shell from initial 2.7 nm CdSe cores NCs as described in Section 4.1.1. The spectra, each taken after the completion of a single CdS layer, show the progressive red shift with increasing shell thickness characteristic of the delocalization of the conduction-band electron in the CdS shell. The PLQY quickly increases to reach a value of 40-45% when 2-3 layers of CdS are grown (see Figure 4.4b). Further growth of CdS leads to a progressive reduction of the PLQY to values of about 20% for 6 CdS layers. A similar behavior has been described for SILAR procedures using CdSe cores synthesized using a protective atmosphere and has been attributed to the enhanced strain or the occurrence of crystal defects with increasing shell thickness [23].

4.2.4 Size Tuning of CdSe Nanocrystals

For CdSe size tuning is an important parameter. Tuning the size means tuning the absorbed and emitted light. Therefore we developed 2 ways of size-tuning in our

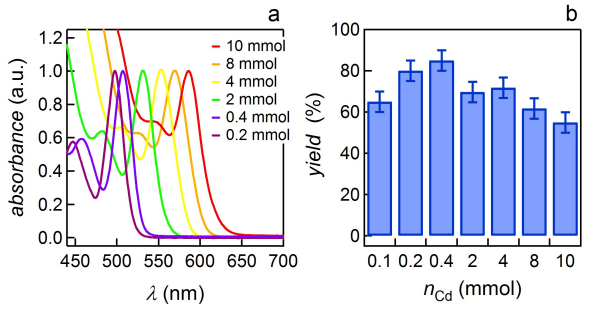

Figure 4.5: (a) Absorption spectra of different CdSe NC batches synthesized using n_{Cd} as indicated and proportionally scaling the amounts of all other reagents relative to the standard synthesis, except the solvent. In this case, oleic acid is used as the carboxylic acid. Importantly, all reactions have been stopped after 10 min of reaction time, a point at which the reaction yield and the NC diameter have reached their final value, irrespective of the precursor concentration (b) Reaction yields obtained after 10 min of reaction time as a function of n_Cd.

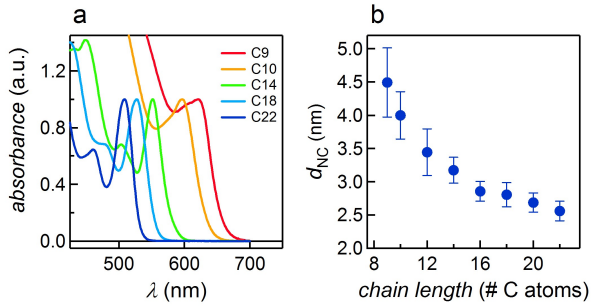

Figure 4.6: (a) Absorption spectra of different CdSe NCs batches synthesized using different carboxylic acids, as characterized by the number of carbon atoms in the aliphatic chain. For all syntheses, standard conditions of concentrations and temperature where used. (b) Variation of (marker) average NC diameter and (error bar) size dispersion as a function of the number of carbon atoms in the aliphatic chain of the saturated carboxylic acid.

CdSe synthesis method.

As shown by Figure 4.5a, increasing the concentration of all the reagents (oleic acid, CdO and Se) while keeping the reaction volume constant results in a systematic redshift of $\lambda_{^1S_e-^1S_h}$ and thus, larger NCs. Raising the amount of CdO from 0.1 mmol up to 10 mmol (and proportionally increasing the amount of OA and Se) shifts $\lambda_{^1S_e-^1S_h}$ - as recorded on aliquots taken 5 minutes after the injection - from 480 to 600 nm. However, increasing the concentration results in a deterioration of the size dispersion, and a reduction of the reaction yield (see Figure 4.5b). Never-

theless, for the highest amounts of CdO used, 50 mg of CdSe NCs are formed for each mL of solvent used, which means that the solid loading in the reaction mixture amounts to 50 g/L. Size tuning at a constantly high reaction yield is possible by changing the chain length of the carboxylic acid used. As shown in Figure 4.6a and 4.6b, changing the length of this acid chain from 22 (behenic acid) to 9 carbon atoms leads to an increase of the NC diameter from 2.5 to 4.5 nm. Also in this case, larger NCs are only obtained at the expense of a deteriorated size dispersion.

4.2.5 Expanding The Method To ZnSe NCs

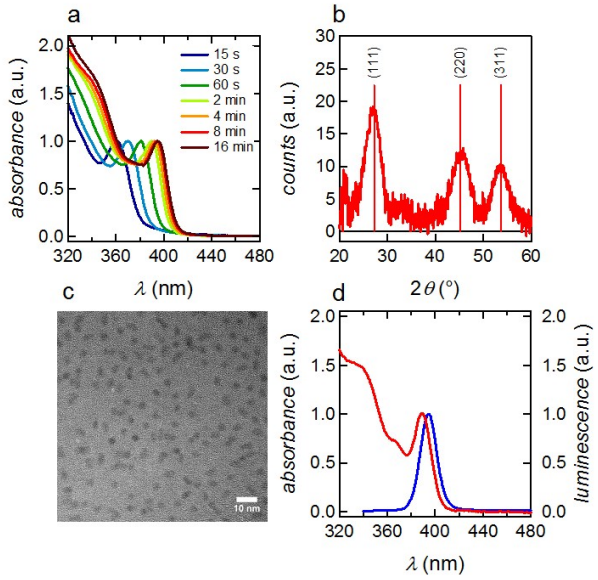

Figure 4.7: (a) Absorption spectra recorded on aliquots taken at the time indicated after the injection of black selenium powder in a mixture of zinc oleate (0.4 mmol), excess oleic acid (0.4 mmol) and octadecene (10 mL) at 270 °C. The initial progressive redshift of the absorption peak of the first exciton transition is indicative of the formation and growth of ZnSe NCs, the final spectra that start to overlap indicate a stop of growth. (b) Reflections of the crystal lattice measured with X-ray diffraction indication a zinc blende lattice. (c) Bright field TEM image of the resulting ZnSe NCs. The scale bar corresponds to 10 nm. (d) (red) Absorbance and (blue) photoluminescence spectra of ZnSe NCs synthesized under standard reaction conditions.

The value of the method would greatly increase if the precursor could be used for other material systems. A first test will be the synthesis of ZnSe NCs, in the next chapter we will explore further syntheses for the CZTS family.
Upon injection of black selenium powder in a reaction mixture containing a stan-

dard amount of zinc oleate and excess oleic acid in ODE, a process very similar to the CdSe synthesis develops. The absorption spectra shown in Figure 4.7a are now indicative of the formation of ZnSe NCs that grow larger with increasing reaction time. The overlap of the absorption spectra with reaction times longer than 4 minutes in the synthesis indicates that d_{NC} reaches a constant value within 5-10 minutes. Moreover, the yield of the reaction, as determined by analyzing the supernatant after a first purification of the reaction mixture, amounts to $\approx 90\%$, i.e., similar to what is achieved with CdSe NCs. As shown by Figure 4.7b, the reaction results in the formation of zinc blende ZnSe NCs with clear reflections resembling the (111), (220) and (311) planes. For this particular example, an average diameter of 3.4 nm was determined from TEM imaging as seen in Figure 4.7c, however it should be noted that not all NCs appear as quasi-spherical on the TEM micrograph. Figure 4.7d shows the absorbance and corresponding photoluminescence spectra of ZnSe NCs synthesized using the standard reaction conditions. The PL spectrum features the narrow photoluminescence of the ZnSe band gap transition - red shifted by 5 nm relative to the absorbance maximum - with no indication of trap emission at longer wavelengths.

4.3 Metal selenide Nanocrystals: Discussion and Conclusion

4.3.1 Comparison to Other Synthesis Methods

The need for robust and scalable hot injection methods for the production of high quality colloidal NCs has been addressed by various authors. This involves issues of synthesis methodology and that of final product cost, especially in view of large volume applications such as photovoltaics or lighting. In this respect, a number of authors have raised the issue of phosphine-based chalcogenide precursors, which are toxic, expensive, oxidation sensitive and may show important batch to batch variations of purity. In the case of selenium precursors, most alternatives boil down to a precursor that is based on the dissolution of elemental selenium in an organic solvent such as octadecene, diesel or paraffin. Either used in a hot injection or a heating up procedure, the use of black selenium homogeneously dissolved in organic solvents results in a relatively slow reaction with a limited reaction yield. For comparison, Figure 4.8 summarizes the synthesis development of a typical CdSe NC synthesis using such a dissolved ODE-Se precursor as originally proposed by Jasieniak et al. [24]. The absorption spectra (Figure 4.6a) already indicate that the NC growth stage is considerably longer for this reaction since the spectra keep shifting to longer wavelengths even after 50 minutes. This concurs with a relatively slow increase of the chemical reaction yield up to $\approx$35% after 50 minutes. A similar slow reaction is obtained by Yang et al. when heating

up a mixture of black selenium and cadmium myristate in ODE. However, in our approach a CdSe yield of 80-85% with a steady diameter is achieved with the black Se precursor within 5-10 minutes.

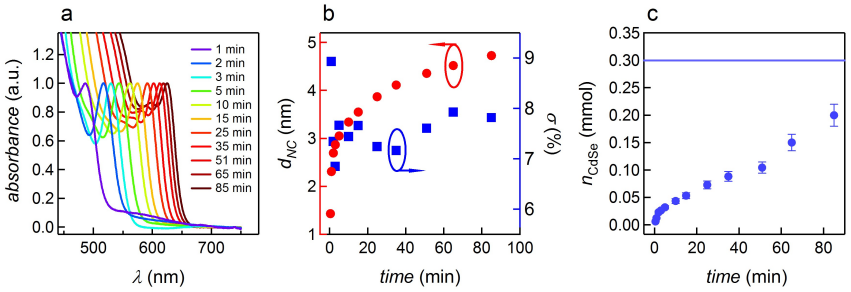

Figure 4.8: (a) Absorption spectra recorded on aliquots taken at the time indicated after the injection of black selenium (0.3 mmol) homogeneously dissolved in octadecene (3 mL) in a mixture of cadmium oleate (0.4 mmol), excess oleic acid (2.4 mmol) and octadecene (7.75 mL) (injection/growth temperature: 260/235 °C). The black selenium was dissolved in ODE by heating at 190 °C for 150 min. The spectra are normalized at the first exciton peak absorbance. (b) Time development of (red circles) average NC diameter and (blue squares) size dispersion as obtained from the absorption spectra. (c) Time evolution of the amount of CdSe formed, relative to the amount of Se injected, as determined from UV-VIS absorption spectroscopy.

4.3.2 Prospects in Up-scaling

For scaling up, the combination of a slow reaction and a limited reaction yield is problematic, in particular for the synthesis of NCs with small sizes. Using a reaction as the one shown in Figure 4.8, typically obtained by stopping the reaction in an early stage, where the reaction yield is low. A far more interesting approach is to use a fast, high yield reaction and size tunability of the NCs via the reaction conditions. This is exactly what the black Se precursor as introduced here offers. The reaction runs to completion within 5-10 minutes and the as-synthesized NCs reach a constant diameter in the same time span. Moreover, we find that for our developed method the final NC diameter can be tuned by changing the carboxylic acid used in the reaction or by changing the precursor concentrations. However, while for small sizes, extremely narrow size dispersions are obtained, the size tuning methods only yield larger NCs at the expense of the size dispersion. This remains a limitation of the proposed technique.

An important cost factor in solution-based synthesis is the volume of solvents needed to produce a given amount of material. For the syntheses described here, we translate this into the solid loading of the reaction mixture, i.e., the weight of

the NCs versus the volume of the solvent. With the homogeneous dissolved ODE-Se precursor, the limited solubility of selenium in the organic solvent restricts the solid loading. Typical values found in literature amount to 8 g/L. In the case of the black Se precursor, the ODE is only a carrier for the powder, and the synthesis can be performed under conditions where 5 mmol of selenium is injected using only 1 mL of ODE as a carrier. With the highest precursor amounts shown in Figure 4.5, over 0.5 g of CdSe is obtained using 11 mL of solvent. The resulting solid loading of 50 g/L is about 10 times higher than what is typically reported for TOP-Se or ODE-Se based syntheses for zinc blende CdSe NCs.

As discussed above, the use of a heterogeneous ODE-Se precursor offers several

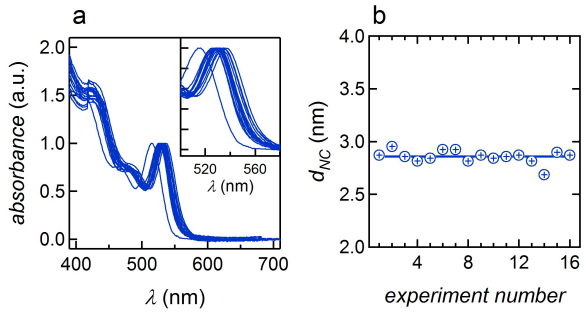

Figure 4.9: (a) Normalized UV-VIS absorption spectra of 16 CdSe NC dispersions obtained by executing the previously described synthesis using an automated liquid handler. The reaction is carried out by injecting 0.27 mL of ODE containing 0.027 mmol of black selenium powder in a vial filled with 2.7 mL ODE containing 0.054 mmol of cadmium oleate kept at 250 °C. (b) The NC diameter as a function of experiment number as calculated from the absorption spectrum. The full line indicates the average diameter of 2.87 nm.

advantages in the case of CdSe and ZnSe NCs in terms of scaling up. The reaction does not use phosphines, it is fast and tunable, has a high reaction yield even for small NCs and it can be run under air with little use of solvents. Although heterogeneous precursors have been used before for the synthesis of colloidal NCs by hot injection, most notably for the formation of PbS, the question remains as to whether they can be used for the reproducible synthesis of large quantities of colloidal NCs. Indeed, a critical step in the method involves the injection of the black selenium precursor under the form of an unstable dispersion of selenium powder in octadecene. This appears as an ill controlled step since selenium powder may stick to the vial used for precursor preparation or the syringe used in the injection. To prevent this, the selenium precursor is vigorously shaken up to the moment of injection. Note that in case of upscaling towards larger volumes the autoignition point of ODE can become a problem. The autoignition point is set at 250 °C and since temperatures up to 270 °C are reached it is highly recommended to work in

neutral atmosphere. An other solution could be the use of a different solvent with a higher autoignition point.

4.3.3 Automated Reproducibility

To show that this approach leads to a well-defined, reproducible synthesis protocol, we used an automated liquid handler under ambient atmosphere to run the same CdSe synthesis based on the injection of black Se 16 times. Figure 4.9 shows the absorption spectra of the dispersions thus obtained, together with dNC as a function of the synthesis run. Disregarding the single outlier, the NCs have a batch-to-batch average diameter of 2.87 nm with a standard deviation of 0.04 nm, i.e., 1.4%. Although no attempts have been made to optimize the automated procedure, this result is in between the 2.5% and 0.25% batch-to-batch variation reported for the manual and automated synthesis of CdSe NCs using a homogeneous TOP-Se precursor, respectively. Hence, the automated precision handling of a heterogeneous precursor is clearly possible.

4.4 Conclusions

In this chapter we have proven that CdSe NCs can be synthesized in a fast, cheap and reproducible manner with yields near 100%. Our approach is up to 20 times faster than literature based methods, while the synthesis costs are reduced by the use of less expensive solvents, the possibility to work in atmospheric conditions and the possibility to work with higher solid contents in solution. Because this chalcogenide system can be considered as a model system, we believe that this research opened the door to the improvement of other types of NCs synthesis. Also in the case of chalcogenide nanoparticles for TFPV, we can use this heterogeneously dispersed chalcogenide precursor. We will explore if the method next to Cd and Zn, also works for Cu and Sn based NCs.

5

Synthesis of all CZTS(e) Precursors

In this chapter we will explore syntheses for NCs that can be used as printable precursors for the formation of thin film CZTS(e) solar cells. The as-synthesized NCs will be dispersed in an ink to prepare a thin film of CZTS(e) with the correct composition after an annealing process in a S or Se rich atmosphere. These precursor NCs can comprise out of quaternary selenide or sulfide NCs of the CZTS(e) materials family ($Cu_2ZnSnS(e)_4$), or a combination of binary ($CuS(e)_2$,ZnS(e) and $Sn(Se)_2$) and ternary ($Cu_2SnS(e)_3$, $Cu_2ZnS(e)_2$ and $ZnSnS(e)_2$) sulfide or selenide NCs. We believe that the use of chalcogenide based nanocrystals has an advantage over metallic or oxide based precurors. Using these chalcogenide NC ensures us

	Sulfides	Selenides
Binary	CS	CSe
	TS	TSe
	ZS	ZSe
Ternary	CTS	CTSe
	CZS	CZSe
	ZTS	ZTSe
Quaternary	CZTS	CZTSe

Table 5.1: The CZTS matrix of NCs that can be synthesized and used for the later formation of CZTS thin films

that we will not have problems with the removal of oxygen or the introduction of chalcogenide since it is already present in the layer. An overview of the potential presursor NCs can be found in Table 5.1.

Katagiri et al. were the first to publish the fabrication of thin film CZTS solar cells by means of expensive vacuum deposition in 2001. In a more extended paper published in 2009, they showed that the ratio of elements in the CZTS solar cell has a significant influence on the device performance. Zinc rich and copper poor absorber layers showed higher resistivity, which improves the solar cell performance. This publication quickly opened the general interest in CZTS(e) solar cell fabrication, and in particular the use of precursor NCs because of the possibility to dramatically decrease production costs compared to expensive vacuum deposition. Within the same month two publications appeared on the fabrication of CZTS(e) NCs for solar cells. Guo et al. started from the hot injection method where NCs were synthesized using oleylamine (OLA) as a coordinating solvent, copper and zinc acetylacetonate ($Cu(Acac)_2$, $Zn(Acac)_2$) and tin acetylacetonate bromide ($Sn(Acac)_2Br_2$) as metal salts and sulfur dissolved in OLA as a sulfur precursor (OLA-S). Steinhagen et al. used the heating up approach from a similar mixture, but the $Zn(Acac)_2$ and the $Sn(Acac)_2Br_2$ got replaced by Zn acetate ($Zn(Ac)_2$) and $SnCl_2$ respectively.
However, these synthesized CZTS(e) NCs remained Zn poor. Our intent was to synthesize Zn rich CZTS(e) NCs, by means of hot injection synthesis, similar to Guo et al., using also $Cu(Acac)_2$ but different Sn or Zn salts. The sulfide or selenide NCs were synthesized using sulfur dissolved in OLA or black selenium in a carrier liquid developed in Chapter 4.1 of this thesis respectively. In this chapter the possibility of the formation of CZTS(e) NCs with various compositions is shown. Moreover, we will show that most of the sulfide and selenide NCs can be synthesized keeping the predefined goals as low reagent cost, high solid load synthesis, no need for protective atmosphere, purification cost and waste management.

5.1 Synthesis of Quaternary Compounds

5.1.1 Synthesis of CZTS

The synthesis of the CZTS NCs used for solar cell fabrication has been adapted from a synthesis published by Guo et al [25]. A solution of $Cu(Acac)_2$ (5 mmol), $Zn(Ac)_2$ hydrate (2.5 mmol) and $Sn(Cl)_4.5H_2O$ (2.5 mmol) in 20 mL of OLA was heated to 260 °C and flushed to remove the present H_2O. Afterwards, the sulfur precursor is injected, using 10 mmol of grained sulfur powder (fine powder will dissolve faster) in 5 mL of OLA (OLA-S). After injection, the temperature drops

to 240 °C and the reaction is stopped after 30 minutes. An equal amount of toluene (or other nonpolar solvent) is added to the reaction mixture, to prevent the mixture from solidifying and to simplify the purification. This final mixture is purified by a precipitation and redispersion step. First, the ethanol is added to the mixture as non-solvent, causing precipitation. This precipitate, retrieved after centrifugation, can be redispersed in toluene or other nonpolar solvents (e.g. hexane, dodecane). In Figure 5.1 A flow chart of the synthesis is shown.

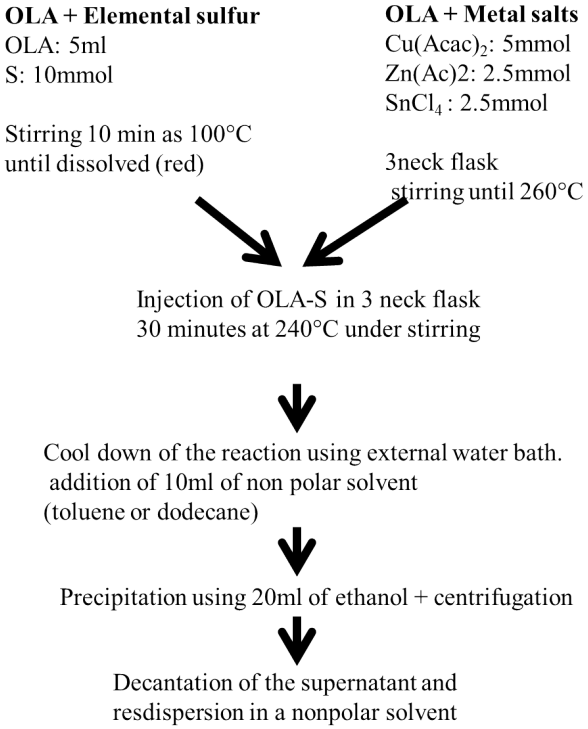

Figure 5.1: A flow chart of the CZTS synthesis

The reaction mixture can be upscaled from 20 mL to 500 mL of volume, in order to produce a sufficient amount of NCs for ink formulation. This involves the use of 100 mmol of Cu, 50 mmol of Zn and 50 mmol of Sn salt in 500 mL of OLA and the use of 200 mmol S in 50 mL of OLA. Reaction time and purification remained the same.

The TEM micrograph in Figure 5.2a shows that the CZTS procedure results in polydisperse NCs with an average diameter of 11.5 nm (see Figure 5.2a). Re-

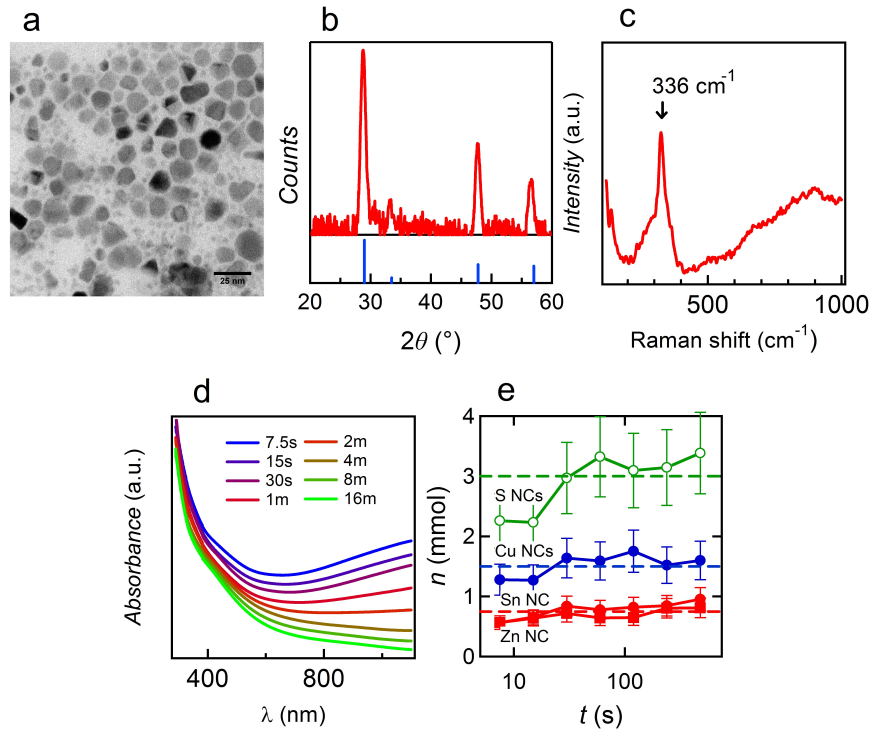

Figure 5.2: (a) TEM micrograph of CZTS NCs formed by the injection of OLA-S into a solution of Cu, Zn and Sn salts in oleylamine after 16 min of reaction time (see text). Scale bar: 25 nm. (b) X-ray diffractogram of the CZTS NCs thus formed. The vertical lines indicate the most important reflections of chalcopyrite based CZTS. (c) Raman shift of the CZTS NCs, indicating that the chalcopyrite based structure is kesterite. (d) Normalized absorption spectra of aliquots taken at the indicated time after the S injection. The different spectra are offset for clarity. (e) Time development (log t) of the amount of (green circles) S, (blue dots) Cu, (red squares) Sn and (red circles) Zn in the precipitate after the second, size selective precipitation step of the respective aliquots.

flections in the XRD diffractogram recorded on these NCs coincide with the reflections of a chalcopyrite based structure of CZTS (see Figure 5.2b). However, XRD does not suffice to confirm that kesterite CZTS is formed, since some of the binary compounds also have chalcopyrite-like crystal structures, leading to reflections that coincide with the CZTS reflections and so does stannite. Therefore, Raman spectroscopy with a green laser (532 cm^{-1}) was performed on the NCs. Here, we notice a peak at 336 cm^{-1}, which corresponds to kesterite, indicating the presence of the CZTS kesterite crystal structure (see Figure 5.2c). The detection of secondary phases in such small crystallites in nearly impossible, and therefore

we are not certain that they are absent.
The development of the reaction was followed by analyzing aliquots taken during the reaction. These aliquots were analyzed via absorption spectroscopy for optical and quantitative analysis, while XRF was used for elemental analysis. Absorption spectroscopy on these aliquots leads to the conclusion that CZTS is not immediately formed, since a broad absorption band is still present in the NIR after 4 minutes of synthesis. This absorption band can be appointed to CuS formation at the beginning of the reaction, leading to a broad plasmon resonance peak (see Figure 5.2d) [26]. XRF spectroscopy on the aliquots shows that at the start of the reaction a relative equal amount of all elements is consumed (see Figure 5.2e), meaning that next to CuS NCs also Zn and Sn react with S as a complex or even as NCs. During the reaction, the amount of Zn and Sn incorporated increases and the CuS plasmon resonance peak decreases, indicating the formation of the CZTS NCs. After 16 minutes the plasmon resonance peak completely disappeared, yielding stoichiometric CZTS NCs with a Cu_2ZnSnS_4 ratio. The yield of the synthesis was determined using absorption spectroscopy to be 85%.
The stoichiometry of the CZTS NCs is easily adjusted by using the desired stoichiometry in metal salts at the beginning of the synthesis. Since preferably zinc rich and copper poor CZTS NCs are used for solar cells applications, we used a 20% Zn excess and a 10% Cu deficit, resulting in Zn rich and Cu poor NCs.
It is worth mentioning that if the initial copper precursor ($Cu(Acac)_2$) is changed to other copper salts, like $CuCl_2$ or $Cu(Ac)_2$, a black precipitate without dispersable NCs is obtained after synthesis. Hence, the use of $Cu(Acac)_2$ seems to be desirable. A reason for this behavior is still unknown.

5.1.2 Synthesis of CZTSe

We extended the method developed for the synthesis of CZTS NCs with minor changes to the formation of selenide based kesterite $Cu_2(Zn,Sn)Se_4$ (CZTSe) NCs. A solution of $Cu(acac)_2$ (3 mmol), $Zn(Ac)_2 2H_2O$ (2.5 mmol) and $SnCl_4 5H_2O$ (1.5 mmol) in 10 mL of OLA was heated to 260 °C under vigorous stirring, after which 3 mmol of Se powder is injected using 2 mL of OLA as a carrier liquid, which is similar to the method in Section 4.1. After the injection, the temperature drops to 240 °C and the reaction is stopped after 30 minutes. The final product is purified by successive precipitation/redispersion steps. Here, we first use ethanol as the non-solvent and the toluene-OLA mixture as the solvent, followed by two more precipitation/redispersion steps using ethanol and toluene as the respective non-solvent and solvent.

The TEM micrograph in Figure 5.3 shows that the CZTSe procedure results in relatively polydisperse NCs with irregular shapes and typical dimensions in the 10-30 nm range. The reflections in the X-ray diffractogram recorded on these NCs

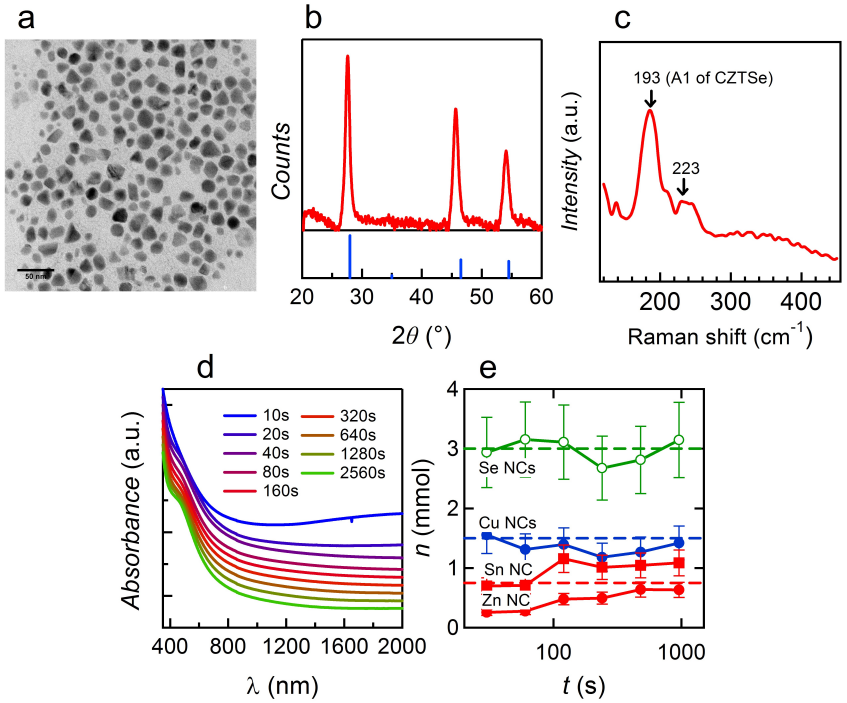

Figure 5.3: TEM micrograph of CZTSe NCs formed by the injection of Se powder into a solution of Cu, Zn and Sn salts in oleylamine after 32 min of reaction time (see text). Scale bar: 50 nm. (b) X-ray diffractogram of the CZTSe NCs thus formed. The vertical lines indicate the most important reflections of chalcopyrite CZTSe. (c) Raman shift of the CZTSe NCs, indicating the presence of kesterite. (d) Normalized absorption spectra of aliquots taken at the indicated time after the Se injection. The different spectra are offset for clarity. (e) Time development of the amount of (green circles) Se, (blue dots) Cu, (red squares) Sn and (red circles) Zn in the precipitate after the second, selective precipitation step of the respective aliquots.

correspond to those of kesterite $Cu_2(Zn,Sn)Se_4$. However, binary structures show a similar crystal structure which overlap in the XRD pattern (similar as for the CZTS NCs). Therefore, again Raman spectroscopy was performed, which indicated the presence of Se based kesterite. No other phases could be detected. The development of the reaction was again followed by the analysis of aliquots taken during the reaction. Absorption and XRF spectroscopy on these aliquots lead to the conclusion that CuSe is formed first, with the plasmon resonance of CuSe as its characteristic fingerprint, after which first Sn followed by Zn is incorporated in the NCs. During the reaction, the amount of Zn and Sn incorporated rises and the plasmon resonance of the CuSe disappears. The final NCs contain a slight

Zn deficit (see Figure 5.3e). Attempts of increasing the zinc content failed. For CZTSe a zinc poor crystal structure is probably the most stable form. This has also been seen in literature for different CZTSe NCs syntheses [27]. The yield of the synthesis was determined using absorption spectroscopy as 70%.
It should be noted here that the synthesis of CZTSe is performed with a deficit of Se, because an excess of Se causes immediate precipitation of the formed NCs. Therefore, only half of the Se is used compared to the metal atoms present. This does not seem to have and effect on the final composition

5.2 Synthesis of Binary Compounds

5.2.1 Synthesis of ZnS

The ZnS NCs are synthesized similar to the ZnSe quantum dots mentioned in Section 4.2.1. A solution of $[ZnCO_3]_2$ - $[Zn(OH)_2]_3$ (0.4 mmol) and oleic acid (6 mmol) in 6 mL of octadecene (ODE) was heated to 280 °C, leading to bubble formation due to dissolution of the Zn salt, leading to CO_2 and H_2O. Simultaneously, sulfur powder (0.4 mmol) is dissolved in 4 mL of ODE at 100 °C. The sulfur mixture is injected to the zinc mixture, after which the temperature drops to 260 °C and the reaction is stopped after 15 minutes. The final product is purified by successive precipitation/redispersion steps, using ethanol as non-solvent and toluene as solvent.

Small monodisperse ZnS NCs are obtained after synthesis with a zinc blende

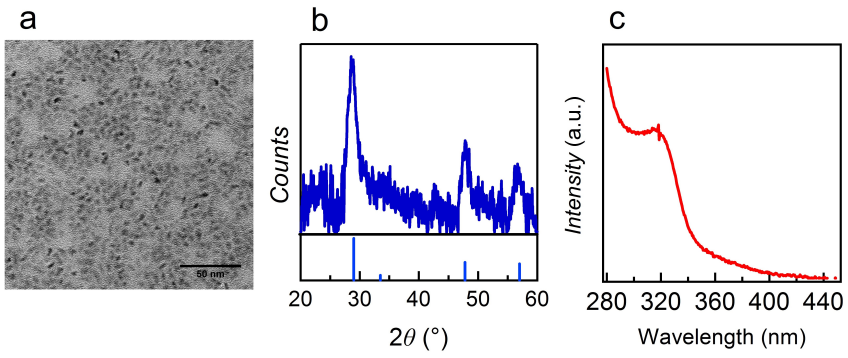

Figure 5.4: (a) TEM micrograph of ZnS NCs formed by the injection of S dissolved in ODE into a solution of Zn-oleate and ODE after 15 min of reaction time (see text). Scale bar: 50 nm. (b) X-ray diffractogram of the ZnS NCs thus formed. The vertical lines indicate the most important reflections of Zinc blende ZnS. (c) Normalized absorption spectrum of ZnS, showing a first exciton peak which is a result of quantum confinement.

crystal structure and a diameter of 2-3 nm, according the TEM micrograph and X-ray diffractogram (Figure 5.4a and b). This result is very similar compared to the selenide synthesis described in Section 4.2.1 of this thesis. The ZnS NCs absorb light starting from 330 nm and show pinkish trap emission under UV light. The yield of the synthesis was determined using the absorption coefficient as 85%.
The ZnS NCs can also be synthesized using the CZTS synthesis method, using oleylamine as a coordinating solvent, $Zn(Ac)_2$ as a Zn source and OLA-S as a sulfur source. The NCs formed through this method are almost identical (similar NC size and same crystal structure) to the ones described above using ODE and OA. The yield of the synthesis was slightly lower to 70%.

5.2.2 Synthesis of ZnSe

The synthesis and results have been discussed in Section 4.2.1.

5.2.3 Synthesis of CuS

The CuS NCs are synthesized similar as the CZTS NCs, by removing the tin and the zinc from the reaction mixture. Here, a solution of $Cu(Acac)_2$ (5 mmol) in 10 ml of OLA is heated to 220 °C, giving rise to light brown solution. The OLA-S precursor (2.5 mmol S in 2.5 mL OLA) is injected. We kept the temperature at 220 °C and stopped the reaction after 15 minutes. The final product is purified once via a precipitation and redispersion step, using ethanol as non-solvent and toluene as solvent.
The TEM micrograph shows that this approach results in polydisperse NCs with an average diameter of 15 nm (Figure 5.5a). The reflections in the X-ray diffractogram corresponds to the hexagonal covellite CuS structure (Figure 5.5b). The presence of a covellite crystal structure indicates the presence of Cu^{2+}. This is in contrast to the tetragonal chalcopyrite structures where Cu(I) is found, which is the desired oxidation state for copper in CIGS and CZTS materials. TEM-EDX measurements confirmed a Cu:S ratio of one (see Figure 5.5d), again indicating the presence of Cu^{2+}. The final product after synthesis was not dark brown as we expected, but dark green. The latter is due to the plasmon resonance of CuS that mainly absorbs in the infrared but tails in the visible light (red), rendering the NCs dark green as can be seen in the absorption spectrum in Figure 5.5c. The yield of the synthesis was determined as 80% using absorption spectroscopy. Attempts to synthesize Cu_2S NCs by reducing the S content in the synthesis was not possible, even when the synthesis was executed with a Cu:S ratio of 4:1, which still yielded covellite CuS. Although the Cu precursor is the same as in the CZTS synthesis, OLA does not seem to be a strong enough reducing agent to reduce the Cu(II) to Cu(I) in this synthesis. As bulk material Cu_2S is only synthesized under

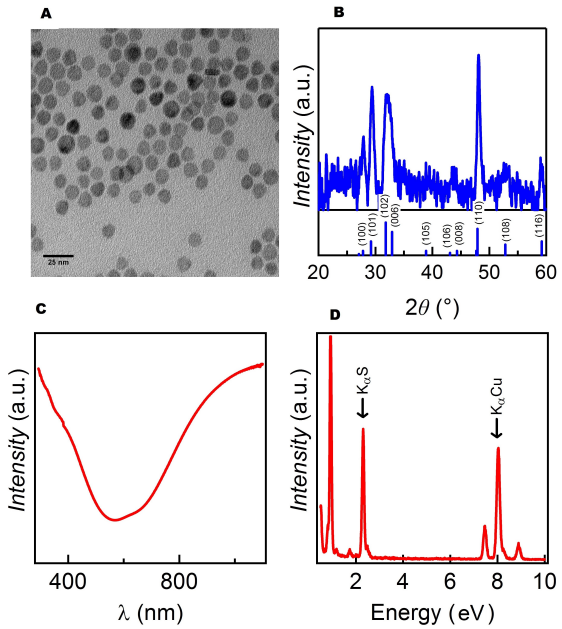

Figure 5.5: (a) TEM micrograph of CuS NCs formed by the injection of S dissolved in OLA into a solution of Cu(Acac)$_2$ and OLA after 15 min of reaction time (see the text). Scale bar: 25 nm. (b) X-ray diffractogram of the CuS NCs thus formed. The vertical lines indicate the most important reflections of covellite CuS. (c) Normalized absorption spectrum of CuS, showing a plasmon resonance feature in the near IR.(d) TEM-EDX spectrum of the CuS NCs under TEM showing a 54% S to 46% Cu ratio.

high pressures. But the addition of stronger reductive such as sodium borohydride might reduce the Cu(II) to Cu(I) [28].

5.2.4 Synthesis of Cu_2Se

Here, we extended the method for the synthesis of CuS NCs, by only changing the chalcogenide precursor from OLA-S to a dispersion of black Se powder in OLA. Here, the Cu:Se ratio is intentionally kept at two, because higher Se amounts will cause precipitation during the reaction. So, a solution of Cu(Acac)$_2$ (5 mmol) in 10 ml of OLA is heated to 220 °C. A mixture of black Se (2.5 mmol) 2.5 mL in OLA is injected. We kept the temperature at 220 °C and stopped the reaction after 15 minutes. The final product is purified once by a precipitation and redispersion step, using ethanol as non-solvent and toluene as solvent.

The TEM micrograph indicates that the resulting NCs are slightly polydisperse and have an average diameter of 10 nm (see Figure 5.6). The X-ray diffractogram

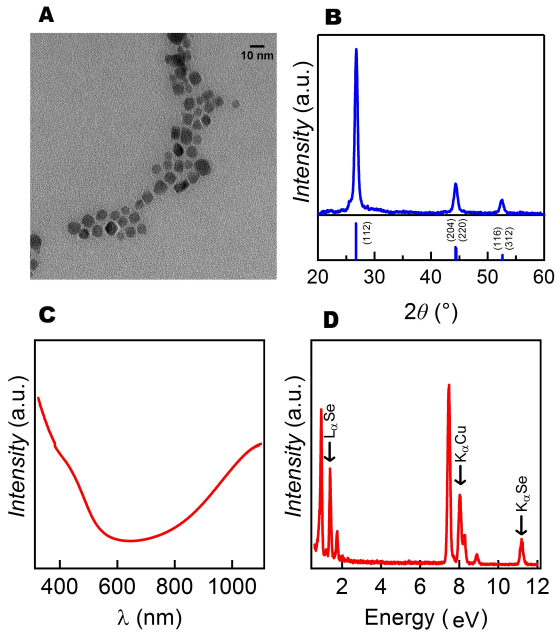

Figure 5.6: (a) TEM micrograph of Cu_2Se NCs formed by the injection of black Se with OLA as a carrier liquid into a solution of $Cu(Acac)_2$ and OLA after 15 min of reaction time (see text). Scale bar: 10 nm. (b) X-ray diffractogram of the Cu_2Se NCs thus formed. The vertical lines indicate the most important reflections of chalcocite Cu_2Se. (c) Normalized absorption spectrum of CuSe, showing a plasmon resonance feature in the near IR.(d) TEM-EDX spectrum of the CuSe NCs under TEM showing a 36% Se to 64% Cu ratio.

shows that the crystals retain the chalcocite Cu_2Se structure, meaning that in this case Cu(II) is reduced to Cu(I) during synthesis. The resulting Cu_2Se NCs also have a green appearance, similar to the CuS crystals. The absorption spectrum in Figure 5.6c shows the presence of a plasmon resonance. The Cu_2Se NCs consist of 64% Cu and 36% Se according to TEM-EDX measurements. The yield of the synthesis was using absorption spectroscopy determined as 65%.

5.2.5 Synthesis of SnS

The synthesis for SnS NCs proceeds similar as the CuS synthesis. Here, $SnCl_2$ (4 mmol) was brought into 10 mL of OLA and heated to 200 °C. However, the Sn salt does not completely dissolve and instead an ochre turbid mixture is formed. Nevertheless, the OLA-S precursor (4 mmol S in 4 mL OLA) is injected in the Sn mixture. The reaction is stopped after 15 minutes. The final NCs are purified by successive precipitation and redispersion steps, using ethanol as non-solvent and

toluene as solvent.

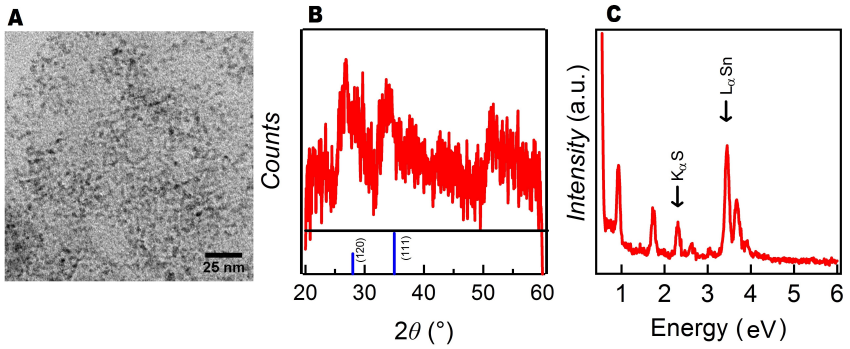

Figure 5.7: (a) TEM micrograph of SnS NCs formed by the injection of OLA-S into a solution of $SnCl_2$ and OLA after 15 min of reaction time (see text). Scale bar: 25 nm. (b) X-ray diffractogram of the SnS NCs thus formed. The vertical lines indicate the most important reflections of zinc blende based SnS. (c) TEM-EDX spectrum of the SnS NCs under TEM showing a 35% S to 65% Sn ratio.

A turbid black mixture is obtained after synthesis. The turbidity remains after purification, moreover the formed NCs precipitate after time. This makes these NCs impossible to use for CZTS(e) preparation, because stable NCs suspensions are required. However, the turbid black precipitate can be removed by means of centrifugation, yielding a clear solution. The TEM micrograph of this clear solution indicates that small NCs of 2-3 nm are obtained after synthesis (Figure 5.7a). The X-ray diffractogram shows a very low signal which could corresponded to orthorombic SnS (Figure 5.7b). The SnS NCs show a 35% S to 65% Sn ratio according to TEM-EDX measurements. A clear S deficit is present, this can be due to the fact that the NCs are very small and have a Sn-rich surface. The yield of the synthesis was determined with XRF as 14%.

5.2.6 Synthesis of SnSe

The synthesis for SnSe NCs proceeds similar as the SnS synthesis, only changing the chalcogenide precursor. $SnCl_2$ (4 mmol) was brought into 10 mL of OLA and heated to 200 °C, in which the Sn salt does not completely dissolve. A mixture of black selenium powder (2 mmol) in 4 mL of OLA was injected in the Sn mixture at 200 °C . The reaction is continued for 15 minutes and the resulting NCs are purified by successive precipitation and redispersion steps, using ethanol as non-solvent and toluene as solvent.

Also here, a turbid black mixture is obtained after synthesis. This turbidity again remains after purification, and the formed NCs precipitate after time. This makes

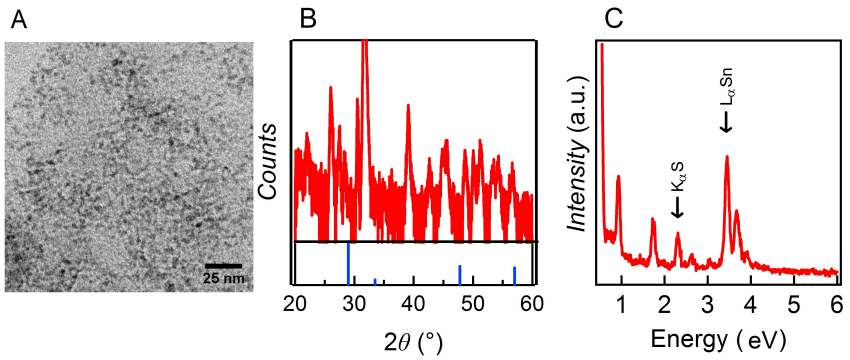

Figure 5.8: (a) TEM micrograph of SnSe NCs formed by the injection of black Se with OLA as a carrier liquid into a solution of $SnCl_2$, and OLA after 15 min of reaction time (see text). Scale bar: 25 nm. (b) X-ray diffractogram of the SnSe NCs thus formed. The vertical lines indicate the most important reflections of zinc blende based SnSe. (c) TEM-EDX spectrum of the SnSe NCs under TEM showing a 30% Se to 70% Sn ratio.

also these NCs undesirable for CZTS(e) preparation, because stable NCs suspensions are required. However, the turbid black precipitate can again be removed by means of centrifugation, yielding clear solutions. The TEM micrograph of this clear solution indicates that small NCs of 2-5 nm are obtained after synthesis (Figure 5.8a). The X-ray diffractogram shows a very low signal which could corresponded to orthorhombic SnS (Figure 5.8b). The TEM-EDX measurements show again a clear deficit in the chalcogenide (Se). The yield of the synthesis was determined using XRF as 30%.

5.3 Synthesis of Ternary Compounds

The synthesis of copper tin sulfide NCs is extensively discussed in literature, because it can have multiple possible applications as a semiconductor and it can even be considered as an alternative for CZTS [29]. These copper tin sulfide NCs can be synthesized in different stoichiometries. For our application, we wanted to develop it as Cu_2SnS_3 so that we can combine it with an equal amount of ZnS to obtain CZTS for solar cell applications.
Copper zinc sulfide and zinc tin sulfide or selenide on the other hand are materials that are practically not mentioned in literature. However, we tried to synthesize these materials by means of hot injection synthesis, similar as the methods described above.

5.3.1 Synthesis of $Cu_2SnS(e)_3$

CTS and CTSe NCs are synthesized starting from a solution of $Cu(Acac)_2$ (5 mmol), $SnCl_4$ hydrate (2.5 mmol) in 10 mL of OLA, which is heated to 240 °C. Subsequently, the desired chalcogenide precursor is injected. This chalcogenide precursor is an OLA-S precursor (7.5 mmol S in 4 mL OLA) or a black Se precursor (4 mmol) in 2 mL of carrier liquid (ODE or OLA). The reaction is stopped after 15 minutes reaction at 240 °C. The final product is purified once via a precipitation and redispersion step, using ethanol as non-solvent and toluene as solvent. Similar results are obtained for the CTS and CTSe procedure. Both pro-

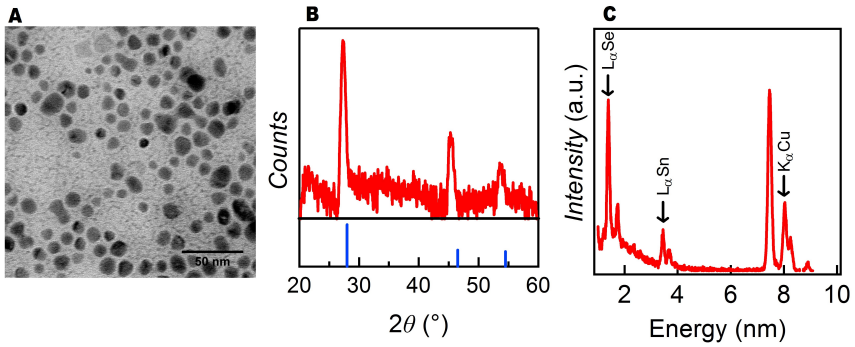

Figure 5.9: (a) TEM micrograph of CTSe NCs formed by the injection of Black Se with OLA as a carrier liquid into a solution of Cu(Acac)$_2$, SnCl$_4$ and OLA after 15 min of reaction time (see text). Scale bar: 50 nm. (b) X-ray diffractogram of the CTSe NCs thus formed. The vertical lines indicate the most important reflections of zinc blende based CTSe. (c) TEM-EDX spectrum of the CTSe NCs under TEM showing a 50% Se to 33% Cu and 16% Sn ratio.

cedures lead to crystalline NCs with an average diameter of 15 nm as determined from the TEM micrographs in Figure 5.9a and 5.10a. The crystal structures are chalcopyrite-like as deducted from the XRD reflections (Figure 5.10b and 5.9b). TEM-EDX measurements shows that the preferred stoichiometry (50% Se, 33% Cu and 16% Sn) was achieved in the case of the sulfide NCs (see Figure 5.10). However, the selenide NCs contain 43% Se, 38% Cu and 19% Sn, rendering them off-stoichiometric in selenium. But the selenide NCs do exhibit the desired Cu:Sn ratio of 2:1 (Figure 5.9). The yield of both syntheses were determined using XRF spectroscopy as 85% for CTS and 65% CTSe.

5.3.2 $Cu_2ZnS(e)_2$

Before we synthesize $Cu_2ZnS(e)_2$, we take a look at literature if the structure possibly exists. For a structure that can represent copper zinc sulfide we have to take a

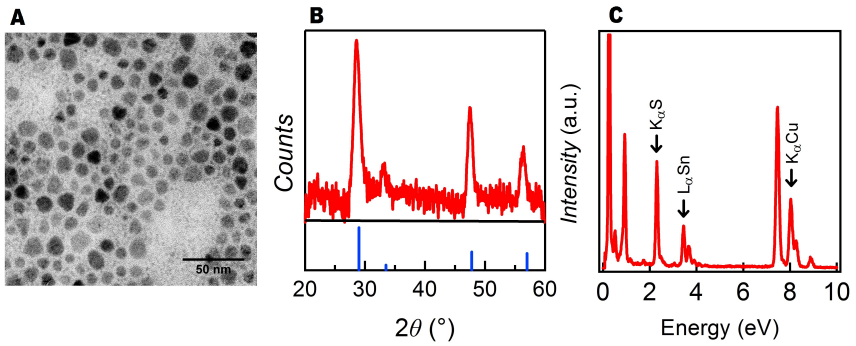

Figure 5.10: (a) TEM micrograph of CTS NCs formed by the injection of OLA-S into a solution of Cu(Acac)$_2$ and OLA after 15 min of reaction time (see the text). Scale bar: 50 nm. (b) X-ray diffractogram of the CuSe NCs thus formed. The vertical lines indicate the most important reflections of zinc blende based CTSe. (c) TEM-EDX spectrum of the CTSe NCs under TEM showing a 43% Se to 38% Cu and 19% Sn ratio.

look at the crystal structure of idaite. This structure originally contains copper and iron, but the iron is easily replaced by zinc. When a replacement occurs the crystal is showing a composition of Cu_3ZnS_4, where Zn replaces the original Fe [30].
We started from a solution of Cu(Acac)$_2$ (3 mmol) and $ZnCl_2$ (1.5 mmol) in 10 ml of OLA heated to 240 °C. Subsequently, the desired chalcogenide precursor is injected. This chalcogenide precursor is an OLA-S precursor (3 mmol S in 3 mL OLA) or a black Se precursor (1.5 mmol) in 2 ml of carrier liquid (ODE or OLA). The reaction is stopped after 30 minutes reaction at 240 °C. The final product is purified via a precipitation and redispersion step, using ethanol as non-solvent and toluene as solvent.

However, redispersion of the CZS NCs was difficult, because only a small fraction redispersed while the main fraction precipitated as a black powder. The TEM micrograph of the NCs shows agglomerated NCs with an average diameter of 25 nm (Figure 5.11a). The X-ray diffractogram (Figure 5.11b) shows the reflection of CZS, similar to the reflections of CZTS and CTS, or thus the chalcopyrite family and not the idaite family as found in literature. The CZS NCs consists of a Cu:Zn ratio of one, according to XRF measurements (Figure 5.11c). However, these CZS NCs are undesirable for CZTS solar cell fabrication, due to the unstable NC dispersion. The yield of the CZS NCs was determined using XRF as 18%. XRF ratio determination between Cu:Zn showed a 55:45 ratio, indicating that more Zn had reacted compared to copper. The absorption spectrum showed no sign of CuS present.
On the other hand for the CZSe NCs dispersion the color was clearly green, indicating that mainly CuSe NCs are actually formed from the CZSe procedure. This

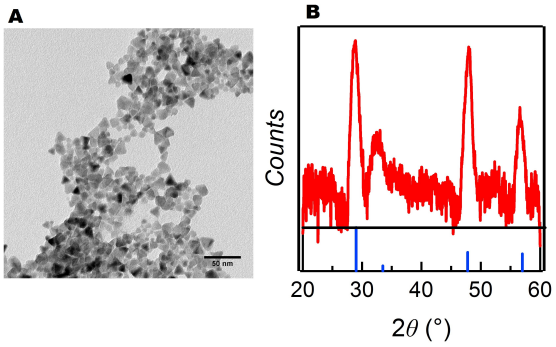

Figure 5.11: (a) TEM micrograph of CZS NCs formed by the injection of elemental S dissolved in OLA in a solution of $Zn(Acac)_2$ and $Cu(Acac)_2$ and OLA, stopped after 15 min of reaction time (see the text). Scale bar: 25 nm. (b) X-ray diffractogram of the CZS NCs thus formed.

was confirmed by XRF measurements on the supernatant and NCs during purification. The supernatant mainly consists of Zn, while the NCs barely contain zinc. Thus our attempt for copper-zinc-selenide ended up in formation of CuSe and unreacted zinc.

5.3.3 $ZnSnS(e)_3$

The synthesis approach for $ZnSnS(e)_3$ is similar to the synthesis developed for CZTS NCs. A solution of $Zn(acac)_2$ (1 mmol) and $SnCl_4$ (1 mmol) in 10ml OLA is heated to 200 °C. The mixture remains slightly turbid. Subsequently, the OLA-S precursor (3 mmol of S in 3 ml OLA) or black Se (1.5 mmol in 2 ml carrier liquid) is injected and the reaction is stopped after 15 minutes. The final product is purified via a precipitation and redispersion step, using ethanol as non-solvent and toluene as solvent.

Only faint TEM micrographs are obtained for the mixtures from the ZTS(e) procedure. Both procedures render NCs with a low contrast and a maximum diameter of 2 nm (Figure 5.12a and 5.13a). The X-ray diffractogram recorded on the mixture obtained from the ZTS procedure seems to match the ZTS structure described in literature [31], although the reflections are very broad, indicating that the formed NCs are crystalline and small or amorphous (Figure 5.12b). The X-ray diffractogram recorded on the mixture obtained from the ZTSe procedure also show very broad reflection, again indicating that the formed NCs are crystalline and small and/or amorphous (5.13b). However, because no literature was found on ZTSe material, the reflections cannot be compared. When both ZTS(e) mix-

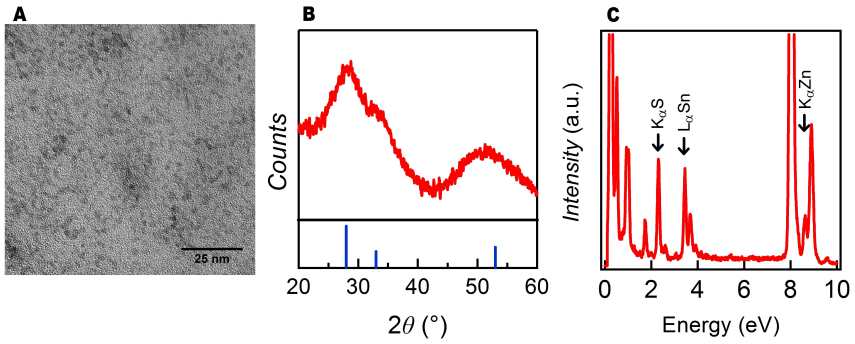

Figure 5.12: (a) TEM micrograph of ZTS NCs formed by the injection of OLA-S into a solution of $Zn(Acac)_2$ and $SnCl_4$ OLA after 15 min of reaction time (see the text). Scale bar: 25 nm. (b) X-ray diffractogram of the ZTS NCs thus formed. Reflections are very broad indicating the (c) TEM-EDX spectrum of the ZTS NCs under TEM showing a 38% Se, 35% Sn and 26% Zn ratio.

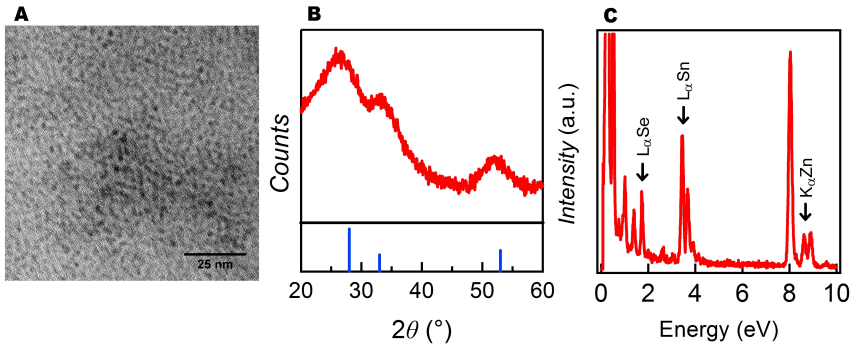

Figure 5.13: (a) TEM micrograph of ZTSe NCs formed by the injection of Black Se with OLA as a carrier liquid into a solution of $Zn(Acac)_2$ and $SnCl_4$ OLA after 15 min of reaction time (see the text). Scale bar: 25 nm. (b) X-ray diffractogram of the ZTSe NCs thus formed. Reflections are very broad indicating the (c) TEM-EDX spectrum of the ZTSe NCs under TEM showing a 20% Se, 62% Sn and 18% Zn ratio.

tures are stored for 2 weeks, a gel-like structure is formed. Yet, it remains unclear whether our mixture consists of a network of ZTS(e) molecules or NCs. TEM-EDX measurements on both ZTS(e) mixtures show that for ZTS a Sn:Zn ratio of one is obtained, while for ZTSe a Zn deficit is present in the mixture. This makes the ZTSe undesirable for our CZTS(e) solar cell fabrication, as only Zn rich CZTS(e) material will lead to better performance of the solar cell. The yield of both syntheses were determined using XRF as 50% for ZTS and 45% ZTSe.

Material	d_{TEM}	Crystal	Yield	Stoichiometry
CZTS	20-25nm	Kesterite	High	Tunable
CZTSe	20-25nm	Kesterite	High	Zn Poor
CuS	10-15nm	Covelite	High	1:1
Cu_2Se	10-15nm	Chalcocite	Medium	2:1
ZnS	2-5nm	Zinc Blende	High	1:1
ZnSe	2-5nm	Zinc Blende	High	1:1
SnS	2-5nm	Unknown	Low	S Poor
SnSe	2-5nm	Unknown	low	Se Poor
CTS	10-15nm	Chalcopyrite	High	Tunable
CTSe	10-15nm	Chalcopyrite	High	Tunable
CZS	15-20nm	Chalcocite	Low	Zn rich
CZSe	10-15nm	Chalcocite	Medium	No Zinc
ZTS	2-5nm	Unknown	High	Sn rich
ZTSe	2-5nm	Unknown	Medium	Sn rich

Table 5.2: The synthesized CZTS components and their properties. We show their diameter measured using TEM. We used XRD to determine the crystal structure. Yield was determined using XRF measurements, low means 10-50%, medium is 50-80% and high means 80-100%. Stoichiometry was determined using TEM-EDX.

5.4 Conclusion

Our synthesis method seems to be versatile and allows us to synthesize most of our matrix of CZTS NCs and composites. These components are listed in Table 5.2.

It is clear that NCs without copper are significant smaller then copper rich NCs, indicating that $Cu(Acac)_2$ has a big influence on the crystal growth in the synthesis. The CZTS(e) synthesis showed that CuS(e) is formed first and is used as a matrix to incorporate the Zn or the Sn. It is also obvious that when sulfides are used, we have no trouble tuning the stoichiometry in the NCs, but selenide NCs have clear trouble incorporating the Zn in their matrix.
So, the following conclusions can be made from our results. The synthesized CZTS NCs are a viable option to obtain the CZTS thin film photovoltaic. These NCs are tunable, the yield is high and they already retain the desired crystal structure. Furthermore, the solid loading of our synthesis is almost double compared to literature and exists of 50 g NCs for 1 liter of solvent [25]. CZTSe NCs, on the other hand, seem less viable since they are Zn poor and CZTS(e) solar cells are preferably Zn rich to achieve the p-type characteristic. Forming stoichiometric CZTS(e) using binary NCs seems possible, although the yield of the Sn sulfide and selenide NCs is low. Combinations of binary and ternary NCs are preferably formed using CTS and ZnS. Both syntheses show a high yield and are easily opti-

mized. The Cu:Sn ratio can be set at 2:1 and the Zn can be tuned as desired since the Zn is introduced through the addition of separate NCs that can be added in a desired amount.

The precursor made of CZTSe NCs showed a zinc deficit on quaternary NCs, this problem would be solved using CTSe and ZnSe NCs since we can make it Zn rich by simply adding more ZnSe.

Furthermore we can combine the strange ZTS NCs with CuS NCs. This gives a combination in which we can obtain a Sn rich layer since ZTS is Sn rich. An additional Zn should be added to obtain the desired stoichiometry

The combination of SnS and CZS will be less desired. Here, the SnS proved to have a low yield, so does the CZT. Also the ratio of the CTS is not optimal. The Se are to Zn-poor.

The optimal combinations are given as :

- CZTS
- CTS + ZS
- CTSe + ZSe

Other combinations have downsides from a synthesis point of view and are not optimal to achieve the right stoichiometry. A combination of the binary NCs SnS + CuS + ZnS could be possible if the SnS is optimized and higher yields would be obtained.

Although our particles form a dispersion after synthesis and purification, we still have to transform the dispersion in an ink. Fabrication of an ink means tuning the NC dispersion in such a way it fits the requirements to form a quality film, which will be the topic of the next chapter.

References

[1] V. K. LaMer and R. H. Dinegar, "Theory, Production and Mechanism of Formation of Monodispersed Hydrosols," *Journal of the American Chemical Society*, vol. 72, no. 11, pp. 4847–4854, 1950.

[2] N. A. Frey, S. Peng, K. Cheng, and S. Sun, "Magnetic nanoparticles: synthesis, functionalization, and applications in bioimaging and magnetic energy storage," *Chemical Society Reviews*, vol. 38, no. 9, pp. 2532–2542, 2009.

[3] C. B. Murray, D. J. Norris, and M. G. Bawendi, "Synthesis and Characterization of Nearly Monodisperse Cde (E = S, Se, Te) Semiconductor Nanocrystallites," *Journal of the American Chemical Society*, vol. 115, no. 19, pp. 8706–8715, 1993.

[4] J. Jaseniak, C. Bullen, J. van Embden, and P. Mulvaney, "Phosphine-free synthesis of CdSe nanocrystals," *J. Phys. Chem. B*, vol. 109, pp. 20665–20668, 2005.

[5] J. Liu, H. Yu, Z. Wu, W. Wang, J. Peng, and Y. Cao, "Size-tunable near-infrared PbS nanoparticles synthesized from lead carboxylate and sulfur with oleylamine as stabilizer," *Nanotechnology*, vol. 19, no. 34, p. 345602, 2008.

[6] W William Yu and X. Peng, "Formation of high-quality CdS and other II-VI semiconductor nanocrystals in noncoordinating solvents: tunable reactivity of monomers.," *Angew. Chem. int. Ed.*, vol. 41, pp. 2368–2371, 2002.

[7] T. Trindade, O. C. Monteiro, P. O'Brien, and M. Motevalli, "Synthesis of PbSe nanocrystallites using a single-source method. The X-ray crystal structure of lead (II) diethyldiselenocarbamate," *Polyhedron*, vol. 18, no. 8-9, pp. 1171–1175, 1999.

[8] M. S. Neo, N. Venkatram, G. S. Li, W. S. Chin, and J. Wei, "Size-Dependent Optical Nonlinearities and Scattering Properties of PbS Nanoparticles," *Journal of Physical Chemistry C*, vol. 113, no. 44, pp. 19055–19060, 2009.

[9] T. N. Xu, H. Z. Wu, J. X. Si, and P. J. McCann, "Optical transitions in PbTe/CdTe quantum dots," *Physical Review B*, vol. 76, 2007.

[10] O. I. Micic, C. J. Curtis, K. M. Jones, J. R. Sprague, and A. J. Nozik, "Synthesis and Characterization of Inp Quantum Dots," *Journal of Physical Chemistry*, vol. 98, no. 19, pp. 4966–4969, 1994.

[11] M. A. Malik, P. O'Brien, S. Norager, and J. Smith, "Gallium arsenide nanoparticles: synthesis and characterisation," *Journal of Materials Chemistry*, vol. 13, no. 10, pp. 2591–2595, 2003.

[12] A. J. Nozik, "Quantum dot solar cells," *Physica E-Low-Dimensional Systems & Nanostructures*, vol. 14, no. 1-2, pp. 115–120, 2002.

[13] J. M. Caruge, J. E. Halpert, V. Wood, V. Bulovic, and M. G. Bawendi, "Colloidal quantum-dot light-emitting diodes with metal-oxide charge transport layers," *Nature Photonics*, vol. 2, no. 4, pp. 247–250, 2008.

[14] G. Konstantatos, I. Howard, A. Fischer, S. Hoogland, J. Clifford, E. Klem, L. Levina, and E. H. Sargent, "Ultrasensitive solution-cast quantum dot photodetectors," *Nature*, vol. 442, no. 7099, pp. 180–183, 2006.

[15] X. Michalet, F. F. Pinaud, L. A. Bentolila, J. M. Tsay, S. Doose, J. J. Li, G. Sundaresan, A. M. Wu, S. S. Gambhir, and S. Weiss, "Quantum Dots for Live Cells, in Vivo Imaging, and Diagnostics," *Science*, vol. 307, no. 5709, pp. 538–544, 2005.

[16] J. Park, K. J. An, Y. S. Hwang, J. G. Park, H. J. Noh, J. Y. Kim, J. H. Park, N. M. Hwang, and T. Hyeon, "Ultra-large-scale syntheses of monodisperse nanocrystals," *Nature Materials*, vol. 3, no. 12, pp. 891–895, 2004.

[17] L. Qu, Z. A. Peng, and X. Peng, "Alternative routes toward high quality CdSe nanocrystals," *Nano Letters*, vol. 1, no. 6, pp. 333–337, 2001.

[18] J. J. Li, Y. A. Wang, W. Z. Guo, J. C. Keay, T. D. Mishima, M. B. Johnson, and X. G. Peng, "Large-scale synthesis of nearly monodisperse CdSe/CdS core/shell nanocrystals using air-stable reagents via successive ion layer adsorption and reaction," *Journal of the American Chemical Society*, vol. 125, no. 41, pp. 12567–12575, 2003.

[19] R. K. Capek, I. Moreels, K. Lambert, D. De Muynck, Q. Zhao, A. Vantomme, F. Vanhaecke, and Z. Hens, "Optical Properties of Zincblende Cadmium Selenide Quantum Dots," *Journal of Physical Chemistry C*, vol. 114, no. 14, pp. 6371–6376, 2010.

[20] I. Moreels, B. Fritzinger, J. C. Martins, and Z. Hens, "Surface Chemistry of Colloidal PbSe Nanocrystals," *Journal of the American Chemical Society*, vol. 130, no. 45, pp. 15081–15086, 2008.

[21] I. Moreels, K. Lambert, D. De Muynck, F. Vanhaecke, D. Poelman, J. C. Martins, G. Allan, and Z. Hens, "Composition and size-dependent extinction coefficient of colloidal PbSe quantum dots," *Chemistry of Materials*, vol. 19, no. 25, pp. 6101–6106, 2007.

[22] I. Moreels, Y. Justo, B. De Geyter, K. Haustraete, J. C. Martins, and Z. Hens, "Size-tunable, bright, and stable PbS quantum dots: a surface chemistry study," *Acs Nano*, vol. 5, no. 3, pp. 2004–2012, 2011.

[23] Y. Chen, J. Vela, H. Htoon, J. L. Casson, D. J. Werder, D. A. Bussian, V. I. Klimov, and J. A. Hollingsworth, ""Giant" multishell CdSe nanocrystal quantum dots with suppressed blinking," *Journal of the American Chemical Society*, vol. 130, no. 15, pp. 5026–+, 2008.

[24] J. Jasieniak, C. Bullen, J. van Embden, and P. Mulvaney, "Phosphine-free synthesis of cdse nanocrystals," *The Journal of Physical Chemistry B*, vol. 109, no. 44, pp. 20665–20668, 2005.

[25] Q. Guo, H. W. Hillhouse, and R. Agrawal, "Synthesis of Cu2ZnSnS4 Nanocrystal Ink and Its Use for Solar Cells," *Journal of the American Chemical Society*, vol. 131, no. 33, pp. 11672–11673, 2009.

[26] J. M. Luther, P. K. Jain, T. Ewers, and A. P. Alivisatos, "Localized surface plasmon resonances arising from free carriers in doped quantum dots," *Nature materials*, vol. 10, no. 5, pp. 361–366, 2011.

[27] W. Hao, G. Wei, S. Yijing, Y. Zhi, and Z. Yafei, "Hot-injection synthesis and characterization of quaternary Cu 2ZnSnSe 4 nanocrystals," *Materials Letters*, vol. 64, no. 13, pp. 1424–14261426, 2010.

[28] *Chemistry of the Elements*. Elsevier Science & Technology Books, 1996.

[29] N. R. Mathews, J. Tamy Benítez, F. Paraguay-Delgado, M. Pal, and L. Huerta, "Formation of Cu2SnS3 thin film by the heat treatment of electrodeposited SnSCu layers," *Journal of Materials Science: Materials in Electronics*, vol. 24, no. 10, pp. 4060–4067, 2013.

[30] A. H. Clark and R. H. Sillitoe, "Cuprian sphalerite and a probable copper-zinc sulfide, Cachiyuyo de Llampos, Copiap{ó}, Chile," 1970.

[31] Y. Oh, S. Bag, C. D. Malliakas, and M. G. Kanatzidis, "Selective Surfaces: High-Surface-Area Zinc Tin Sulfide Chalcogels," *Chemistry of Materials*, vol. 23, no. 9, pp. 2447–2456, 2011.

Part II

From Ink Stability to Layer Formation

In this part of the thesis we will describe the processing of our crystals into an ink and the fabrication of our absorbing solar cell layer. The goal of our solar cell layer will be to absorb light and transform the energy in an electrical potential. To achieve a reasonable efficiency we prefer to absorb 95% of the incoming light. Then how thick must the layer be? We can calculate the required thickness of the layer using the Beer-Lambert law:

$$I = I_0 e^{-\mu \ell}$$

In this formula I_0 is the intensity of the original light, I is the intensity at distance ℓ in the layer, and μ is the absorption coefficient. If we start from the idea that 95% of the light has to be absorbed and that the light passes the layer twice due to reflection on the molybdenum substrate we find that the layer requires a thickness of 1.5 μm with an absorption coefficient of $> 10^{-4}$.
We choose to form a layer using colloidal processing by using a nanocrystal (NC) containing ink. A distinguished feature of all colloidal systems is that the contact area between colloids and the dispersing medium is large. Therefore interparticle interactions strongly influence the suspension behavior [1]. We must develop an ink using CZTS NCs, a colloidal system with solid suspended crystals. The purpose of the ink will be to deposit an absorber layer, without contaminants, a smooth surface, crack-free and a with a thickness of 1.5 μm after densification.
In this part we will study the fabricated NC inks, their behavior and their final influence on the formed film. In a first chapter the inks will be studied on a nanoscale level, exploring the surface of the crystals. We will study different steric stabilizers attached to the surface of our previous synthesized NCs. The main purpose of this steric stabilizer is to keep the crystals stable in suspension by preventing them from aggregating. To identify and quantify which entity is attached on our crystal surface, ^{1}H-NMR can help. Additionally to the use of steric stabilizers, we will explore charge stabilized NCs, which might allow us to make a carbon free ink.
In a second chapter we will explore the influence of the stabilization on the dispersion, namely what is the effect of the steric or the charge stabilizer. Typically dynamic light scattering (DLS), rheology and dark field (DF) microscopy measurements are performed. These measurements can help us to determine the behavior of the crystals in the ink.
In a final and third chapter we will explore the deposition of the film, we know the properties of our ink and we will explore their influence on layer formation. We focused on wet film deposition and drying. The obtained thin films were analyzed by scanning electron microscopy for a nanoscale look on the film quality. In this part we will use CZTS quaternary NCs as a model system. To test our finding we will extend the system towards the combined system of CTS and ZS NC inks. Although we were able to synthesize more combinations to form CZTS using binary and ternary NC, we did not have the time to study all combinations and limited

ourselves to the most promising systems.

6

Stability of CZTS Nanocrystal Colloids

6.1 Basic Elements of Colloidal Stability

A colloidal dispersion or colloid is a heterogeneous system in which one substance is dispersed as fine particles in a second substance, called the dispersed phase and the dispersing medium, respectively. This subdivision results in a very high contact area between both phases. The concomitant free energy increase makes that colloidal dispersions are typically not thermodynamically stable as compared to a state in which the dispersed particles have aggregated to form a single lumped structure. In this respect, colloid stability concerns preventing aggregation to maintain a colloid in a metastable state. This typically involves the careful engineering of the physico-chemical properties of the particle/dispersing medium interface. A general characteristic of a stable colloid is that the particles remain truly dispersed, i.e., they do not settle under the action of gravity. For a solid material dispersed in a liquid medium this implies that the particles, depending on their density, should have dimensions below 100-1000 nm. With dimensions up to a few tens of a nanometer at best, the NCs described in the previous part fit into this category and the printable CZTS inks we aim for will be in essence colloidal dispersions of CZTS nanocrystals.

6.1.1 Colloidal Stability and Interparticle Forces

Colloidal particles show Brownian motion, hence they collide frequently with each other [2]. This already shows that the stability of colloids will be determined by the interparticle interaction potential. Typically, the overall interaction is seen as the sum of an attractive and repulsive part. Whenever the attractive interactions dominate, the particles will coalesce, and the lack of colloidal stability will eventually lead to the settling of large aggregates. When repulsive forces dominate, colliding particles will tend to rebound, thus avoiding aggregation and ensuring colloidal stability. All dispersed colloidal particles show to some extend attractive Van der Waals (VDWL) interactions, so without the presence of repulsive forces colloidal particles will attract each other and aggregate. In other words, additional repulsive forces are required to counteract the VDWL attractions [1]. As with molecules, different types of VDWL interactions exists, namely Keesom interactions (permanent dipole/permanent dipole interactions), Debeye interactions (permanent dipole/induced dipole interactions) and Londen interactions (induced dipole/induced dipole interactions). London interactions are typically the most important since they are always present because it does not require the existence of permanent polarity. VDWL interactions are always attractive forces that range between 0.2 an 10 nm in influence range. To overcome these attractive interactions the repulsive counterpart should be at least as strong and comparable in range as the attractive interaction [3]. A counter interaction for the VDWL force can come from following mechanisms:

- An electrical double layer (electrostatic or charge stabilization).
- Adsorbed or chemically attached molecules that provide steric hindrance (steric stabilization).
- Free polymer in the dispersion medium (structural or depletion stabilization).

6.1.2 Electrostatic Stabilization

Coulomb repulsion offers a first possibility to counteract the attractive VDWL interactions. Colloidal particles can for example acquire a negative charge by the preferential adsorption of anions. Of course, such a negatively charged particle will attract positive counterions, which will form an electric double layer and shield the charge on the particle. Colloidal stability can result from the repulsion of the double layers of two approaching particles. Since the dispersion medium should dissolve ions well – they are involved in both the charging of the particles and the formation of the counter charge – electrostatic stabilization works best in polar solvents.

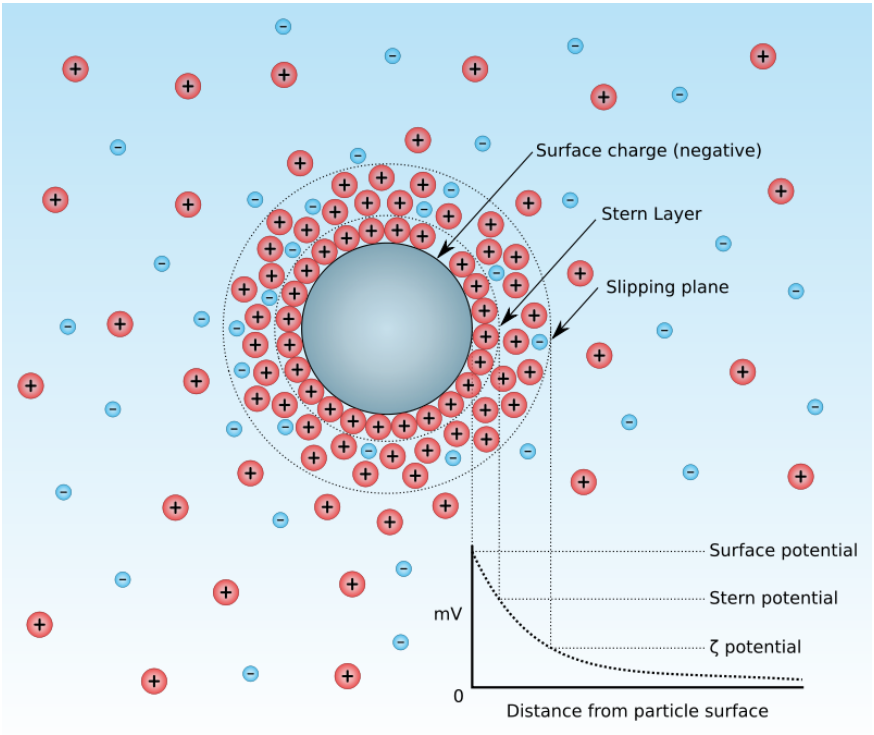

Figure 6.1: Diagram showing the ionic concentration and potential difference as a function of distance from the charged surface of a particle suspended in a dispersion medium [4].

Figure 6.1 represents a negatively charged particle surrounded by a layer of positive counterions. One sees that the counterions surrounding the charged particle have been organized in different layers. First, the Stern layer, consists of ions attracted to the particle up to their distance of closest approach. A second is a diffuse layer in which the drift of ions towards the particle is balanced by their diffusion away from the particle. An important concept in this respect is the so-called slipping surface, an imaginary surface that separates ions that move together with the colloidal particle from ions that are stationary with respect to the dispersion medium. The potential at this surface is known as the zeta potential (ζ-potential) and is often used as an indicator of colloidal stability. Its absolute value is linked to the repulsive Coulomb interaction between two approaching colloidal particles and flocculation will be prevented if it is sufficiently high. Hence, colloids with a high zeta potential (positive or negative) are stabilized by the charge on the colloidal particles, while colloids with a low zeta potentials tend to form aggregates. A zeta-potential lower then $\approx$ 40 mV will mostly lead to coagulation and floccu-

lation. Good repulsion will start from 40 mV, but only when reaching values of 60 mV, perfect long-term colloidal stability is ensured. Note that a zeta potential can be positive or negative, depending on the charge on the particle.

6.1.3 Steric Stabilization

Steric stabilization of colloidal particles is achieved by attaching (grafted or chemisorbed) molecules to the surfaces of the particles, which are mostly long chained organic molecules [5]. These molecules will add a repulsive term to the interparticle interactions and thus promote colloidal stability. As shown in Figure 6.2, different molecular architectures can stabilize a colloid. A first involves homopolymers, which are long chained molecules that tail over the surface (see Figure 6.2a). An alternative is provided by diblock copolymers (see Figure 6.2b), where one side of the polymer chain has a specific affinity for the particle surface, while to other end shows affinity for the solvent. The same principle is applied in Figure 6.2c, which depicts a comb-like copolymer which is anchored on the particle by a polymeric backbone. Finally, Figure 6.2d depicts a surface functionalized by short chained molecules or ligands that bind with an anchoring group to the particle surface and expose a their tail to the dispersing medium.

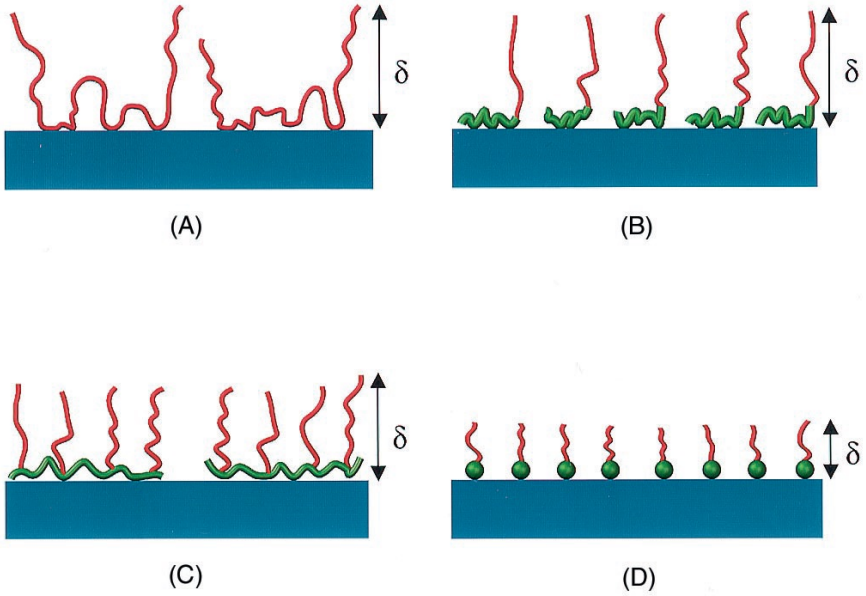

Figure 6.2: (a) Homopolymers (b) Diblock copolymers (c) comblike copolymers (d) functional short chained dispersant or ligands [1]

In general, colloidal stability can be discussed in terms of the free energy

change ΔG due to interparticle interaction, an approach that is particularly convenient to understand the principles of steric stabilization. If interparticle interaction leads to an immediate free energy reduction ($\Delta G < 0$ for all interparticle distances), flocculation or coagulation will result. On the other hand, if the free energy initially increases when two particles come closer, aggregation can be prevented and a stable colloid can be obtained.

An important contribution to the free energy of two approaching particles is the replacement during their approach of ligand-solvent interactions by ligand-ligand interactions. This can be better analyzed by expressing the Gibbs free energy change as a combination of enthalpic and entropic contributions:

$$\Delta G = \Delta H - T\Delta S$$

Consider first a situation where the ligand-solvent and ligand-ligand interactions are identical. This would involve, for example, particles stabilized by polymers or ligands that expose an aliphatic chain to an apolar dispersing medium. In that case, the approach of two particles hardly induces any enthalpy change and ΔG will be solely determined by the change in entropy ($\Delta G = -T\Delta S$. In this respect, the steric hindrance between the ligands grafted on both particles can limit their freedom of motion and the concomitant entropy reduction prevents the approaching particles from sticking together. In that case, the colloid is said to be sterically or entropically stabilized.

On the contrary, in solvents where the replacement of ligand-solvent by ligand-ligand interactions leads to an enthalpy reduction ($\Delta H < 0$), steric stabilization can be countered by the tendency of the system to reduce the ligand-solvent interfacial area. A typical example involves a particle with ligands exposing aliphatic chains to a polar dispersing medium. Aggregation will result and the dispersion medium is called a non-solvent for the colloidal particles. Inducing aggregation by the addition of a non-solvent to a stable colloidal dispersion is an often used method to separate colloidal particles from the dispersing medium.

6.1.4 Depletion Interaction

Depletion interaction of colloidal particles is imparted by macromolecules (polymers) that are free in solution. When particles approach to distances shorter than the length of the macromolecules, they cannot enter the solvent region separating the two approaching particles and osmotic forces will also drive the solvent out of this region, thus causing particle flocculation (so called depletion flocculation). However, when the macromolecule concentration increases, the same phenomenon can actually lead to colloidal stability. Indeed, when the interparticle distance exceeds the macromolecule dimensions, the concentration of macromolecules in the region in between the particles will be the same as at other places in the dispersing

medium. When the interparticle distance is reduced, the macromolecule will be forced out of the region in between the particles. The splitting up of the dispersing medium in regions with low and high macromolecule concentration raises the free energy of the colloidal dispersion, which results in an effective repulsion between the two particles that stabilizes the dispersion. Importantly, depletion interaction reduces the solvent content of the dispersed medium. It is therefore an ideal approach in situations where the solvent content needs to be kept low and the final application can support a high concentration of macromolecules.

6.1.5 Total Colloidal Interactions

Formally, the total interparticle interaction can be written as the sum of the different interaction potentials discussed in the previous sections:

$$V_{tot} = V_{VDWL} + V_{elect} + V_{steric} + V_{dep} \tag{6.1}$$

Here, V_{VDWL} represents the attractive interactions, whereas V_{elect}, V_{steric} and V_{dep} represent the electrostatic, steric and depletion interactions, respectively. Depending on the balance between these interactions, three main states can be distinguished for a colloid, namely dispersed, weakly flocculated and strongly flocculated as schematically represented in Figure 6.3.

The dispersed state is attained when interparticle repulsion leads to a free energy barrier considerably larger than k_bT. In that case, two approaching particles will be kept apart in a metastable state the attractive VDWL forces cannot overcome. Weak flocculation results from a delicate balance between interactions, where the attractive interactions dominate at longer distances yet are countered by repulsive interactions at shorter distances. This can result in a shallow, secondary free-energy minimum (well depth = 2-20 k_bT) and the colloidal dispersion will be marginally stable with the particles weakly flocculating. The local minimum also means that an equilibrium distance exists in the suspension for the particles. Finally, if the attractive forces dominate over the repulsive interactions for the whole range of interparticle distances, particles will come to their distance of closest approach, leading to a strongly flocculated dispersion.

6.1.6 Steric Stabilization Versus Electrostatic Stabilization

As will be made clear in this chapter, we have the possibility to stabilize the colloidal NCs used here either by steric hindrance or by charge. In view of the envisage application, for which a dense and preferably contamination-free film of colloidal NCs is needed, depletion stabilization is out of scope since it requires high concentration of polymers. Below, some key points that mark the differences between the 2 other methods have been listed, paying special attention to the influence they may have on the NC ink.

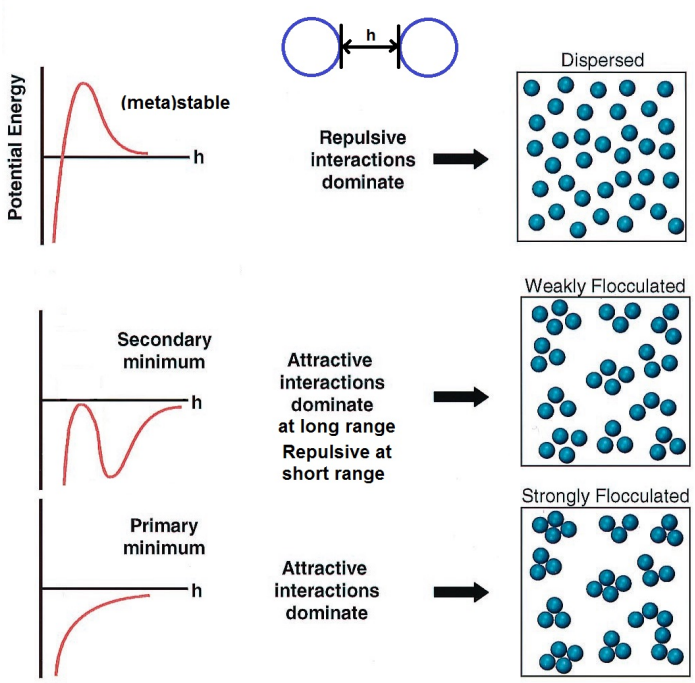

Figure 6.3: Schematic illustration of the relationship between the total interparticle potential energy and the resulting suspension structure. When repulsive attractions dominate a (meta)stable dispersion occurs. When attractive VDWL interactions dominiate at long range but at short range repulsive forces dominate a secondary minimum occurs and this results a weakly flocculated system. When the attractive forces dominate a primary minimum is achieved and the system flocculates. [1]

6.1.6.1 Presence of Electrolytes

Electrostatic stabilization involves a double layer of counterions. Some of these counterions can be unwanted in the final layer, such as Na^+, Cl^- and K^+, ..., while others such as Cu^+, Zn^{2+} or S^{2-} can be of use. Counterions that can decompose into volatile species upon drying or heating, such as NH_4^+ can also be of interest. However, dispersion based on such counterions can prove less stable over time due to loss of those counterions.

6.1.6.2 Presence of organics

Steric stabilization requires steric stabilizers grafted or chemisorbed on the surface. Clearly, this implies that these molecules will be present in the as-deposited layer. Yet, if we aim for a layer that can conduct electric current, removal of as much polymers and organics as possible is necessary. Therefore, short chain ligands

molecules with a relatively low boiling point are preferred over long ligands or polymers. Often used ligands such as oleic acid or oleylamine have boiling points of around 300 °C. This is below the temperature necessary to transform the NC layers, enabling most organic contamination to be removed by a heat treatment. However, the evaporation/pyrolysis of OLA or oleic acid might leave C residues, the molecules are adsorbed onto the NC surface which might decrease evaporation. Removal of these organics should be studied for each separate system. Therefore, we look into the use of shorter chained molecules (e.g. octanethiol (OT)). Shorter chained molecules evaporate at lower temperatures this which can result in a lower contamination of the final layer.

6.1.6.3 Reversibility of Flocculation

The coagulation of charge-stabilized particles (induced for example by the addition of extra electrolyte) is usually irreversible. Particles sticking together after having overcome the double layer repulsion are unlikely to separate again. In contrast, flocculation of sterically stabilized dispersions (induced for example by the addition of a non-solvent) tends to be reversible. Once the non-solvent is replaced by a solvent, colloidal stability is restored, even if the aggregated particles have been completely dried. This process of flocculation with a non-solvent can be used advantageously to purify NC reaction mixtures. Hence, the use of successive non-solvent/solvent additions, will play an important part in the practice of ink formulation we will use.

6.2 Coordination Chemistry of Hot Injection Made Colloidal Nanocrystals

6.2.1 Introduction

Different synthetic routes can be followed to synthesize CZTS NCs, yet the hot injection or heating-up based approaches in apolar media used here stand out because of two major advantages. As demonstrated in the first part of this thesis, the synthetic method is extremely versatile in terms of materials that can be made. Moreover, it leads to a reaction product that is a dispersion of sterically stabilized NCs, where the NCs are coordinated with functional organic molecules we call ligands. In the synthesis used for CZTS NCs, this ligand is oleylamine (OLA). We have introduced the wording *grafted* to describe the binding of polymers to the surface of colloidal particles to ensure colloidal stability. For the functional organic molecules like OLA, we will use the term *bound* instead. In this regard, we will consider each NC to be a giant molecule stabilized by ligands, a term originating from coordination chemistry. In coordination chemistry a ligand coor-

dinates to a metallic species (in this case NC) by sharing electrons. A systematic description of ligands is possible by the bond classification scheme introduced by Green, where ligands are referred to as X-type or L-type depending on the number of electrons the ligand supplies to the NC-ligand bond (one or two, respectively) to form a electron pair bond [6].

6.2.2 The Basic Nanocrystal-Ligand Classes

Various detailed studies on metal chalcogenide or pnictide NCs synthesized in nonpolar media using hot injection or heating up approaches, including CdSe, [7] CdTe [8], PbS, [9] PbSe [10] and InP [11, 12], have shown that the classification of ligands as L-type, X-type or Z-type depending on the number of electrons the NC-ligand bond takes from the NC (0, 1 and 2, respectively) to form a 2-electron bond is a convenient approach [13, 14]. In combination with the need to form charge-neutral NCs in nonpolar environments, this results in two extreme classes. The first describes NCs where the formal charge on the cations and anions is balanced for binary NCs, this corresponds to the bulk stoichiometry and which are passivated by L-type ligands (NC-L_n). The second are NCs that have a net formal charge that is balanced by the opposite charge on X-type ligands. Typically, this involves NCs having an excess of metal cations, stabilized by ligands with a formally negative charge - denoted here as NC(MX_x)$_n$ - although the opposite situation of an anion rich NC with positively charged ligands could also be possible. Remarkably, all detailed, quantitative studies addressing stoichiometry and ligand binding published so far showed as-synthesized and purified NCs behaving according to the NC(MX_x)$_n$ class, where X-moieties correspond to, e.g., carboxylates or phosphonates [7, 9, 15]. L-type ligands such as amines or phosphines on the other hand typically exhibit a dynamic adsorption/desorption equilibrium [9, 12], suggesting that the NC-L_n class results in labile NCs that do not withstand repetitive sample purification.

6.2.3 Practicle Implications of the Ligand Binding Motif

The presence of X- or L-type ligands can have an effect on further purification (i.e. removal of residual reagents or reaction products) of the NCs. The removal of X-type ligands will strip ionic entities from the NC. The limited dielectric screening of the resulting charge in nonpolar media makes that this desorption reaction is strongly inhibited. For L-type ligands on the other hand, ligand desorption leads to the removal of neutral moieties from the NC. Hence, only the NC-ligand binding energy needs to be overcome, which makes L-type adsorption/desorption much more common in non-polar solvents. In this respect, Moreels et al. [9] showed for example that OLA stabilized PbS NCs will not withstand repetitive purifications since the dynamic equilibrium between OLA on the NCs and OLA in the solvent

leads to a progressive ligand loss during purification:

$$NC - OLA \rightleftharpoons NC + OLA$$

Dierick et al. [16] on the other hand found that the L-type ligands present on the surface of copper indium sulfide (CIS) NCs are much less likely to leave the surface then in the case of PbS NCs and well purified dispersions of CIS NCs stabilized by OLA could be obtained. They attributed this finding to the high activation energy of OLA desorption from CIS NCs. Therefore, a non equilibrium coverage of CIS NCs by OLA - and thus colloidal stability of CIS/OLA dispersions - could be maintained for days. This point was proven by comparing results of

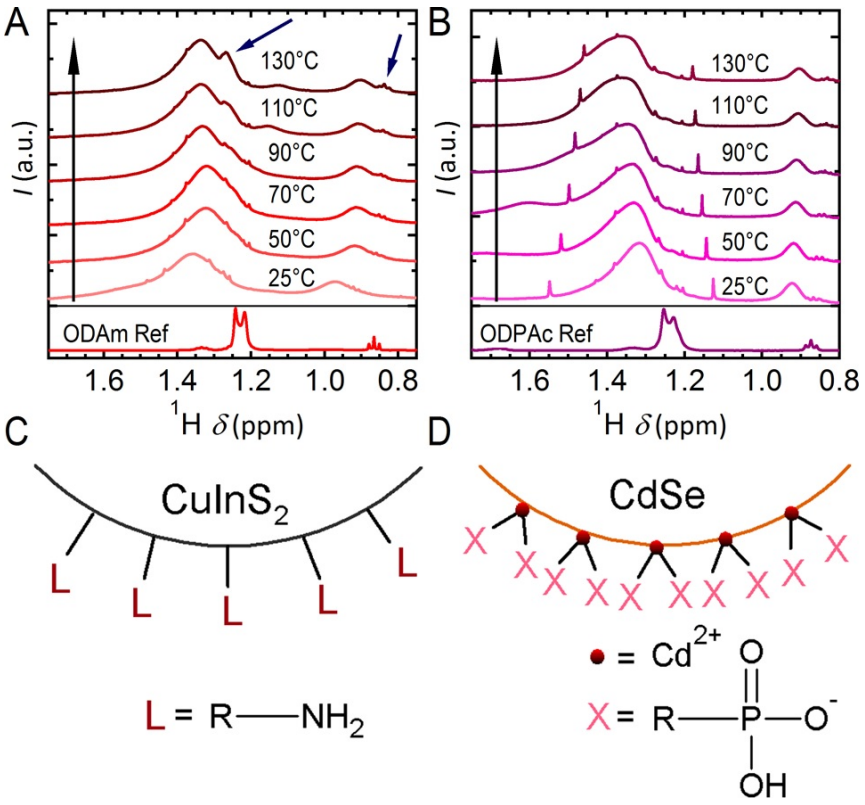

Figure 6.4: In situ heating-up NMR experiments in 1,2-dichlorobenzene-d_4 showing the effect of increased temperature on the alkyl region of CIS NCs capped with octadecylamine (ODAm) (A) and the alkyl region of CdSe NCs stabilized by octadecylphosphonic acid (ODPAc)(B). Arrows in blue emphasize the appearance of sharper resonances. (C-D) Schematic representation of the CIS NC and CdSe NC surface. Reference (ref) spectra of both octadecylamine and octadecylphosphonic acid at 25 °C in 1,2-dichlorobenzene-d_4 are added on the bottom for comparison. [16]

in-situ NMR heating up experiments of X-type bound phosphonic acid ligands on CdSe [17] with L-type OLA ligands on CIS NCs (Figure 6.4). As expected, they found that for the X-type ligand no ligands were released from the surface (6.4b) while the occurence of additional sharp resonances at elevated temperature in the case of CIS stabilized by octadecylamine (blue arrows in Figure 6.4a) points towards the progressive release of ligands. Here, the observation that reducing the sample temperature only leads to a partial readsorption of the ligands was seen as an indication of a kinetically hindered adsorption/desorption process.

6.3 Stabilization of As-Synthesized CZTS Nanocrystals

6.3.1 Experimental

CZTS NCs have been synthesized according to the protocols discussed in Section 5.1.1. After synthesis, the NCs are precipitated using ethanol as the non-solvent and the NC pellet obtained after centrifugation of the unstable colloid is redispersed in toluene. In first instance, a 5 w% NC dispersion is made, to which an extra 5 w% of OLA is added (these initial samples will be referred to as CZTS NCs with an excess of OLA). All subsequent purification steps are done using ethanol as the non-solvent for precipitation, followed by centrifugation, decantation of the supernatant and redispersion in toluene. These purification steps were repeated up to 4 times, resulting in samples denoted as CZTS OLA 1x up to 4x, respectively. For each cycle, the same amount of non-solvent was used and a 5 w% dispersion was formed by redispersion. NMR samples were prepared by evaporating the solvent using an airflow and the resulting dry NCs were redispersed in deuterated toluene. All measurements were performed as fast as possible after sample preparation (typically within half an hour) on a Bruker 500 MHz NMR spectrometer installed at the Nuclear Magnetic Resonance and Structural Analysis Group of Ghent University.

6.3.2 Results and Discussion

Since OLA is the only ligand used for the CZTS NCs synthesized as described in part 2 of this thesis, they are most probably stabilized by OLA, which supposedly binds as an L-type ligand. To confirm this, we used ^{1}H-NMR spectroscopy since this enables us to study the organic molecules on the surface of the NC. 1D ^{1}H-NMR spectroscopy allows for a first distinction between bound and unbound species by the spectral width of the respective resonances. Indeed, ligands attached to a NC will tumble and rotate more slowly as compared to free, unbound ligands, which leads to the broadening of their proton resonances [12].

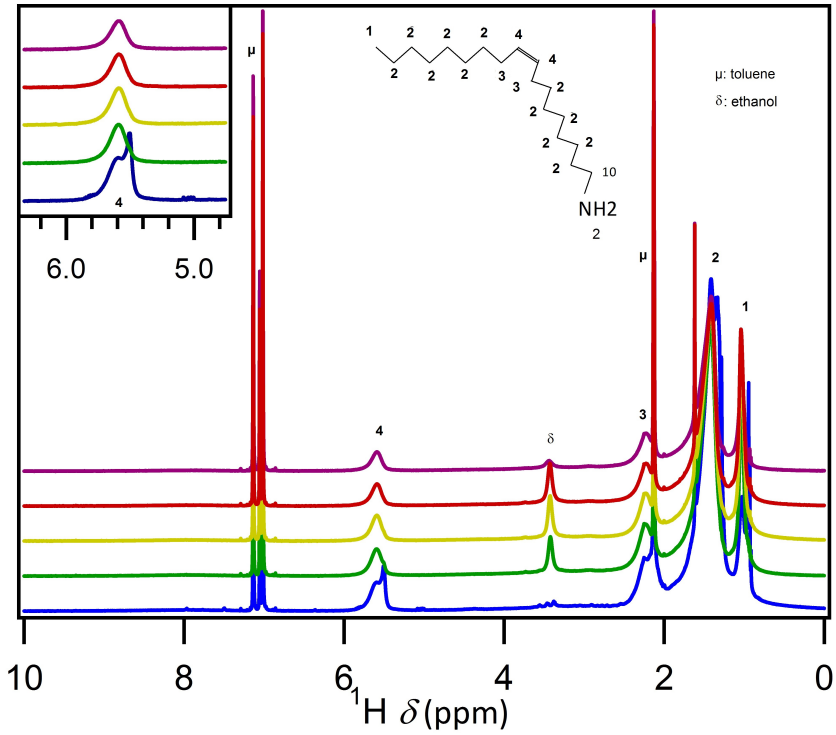

Figure 6.5: A series of 1H-NMR spectra of OLA on CZTS NCs. Red graph represents OLA NCs after synthesis with a small excess of OLA present. The other graphs are constituent purifications of the same sample measured quantitatively. The inset shows the peak of the double bound used to calculate the concentration of OLA in on the NC surface.

In Figure 6.5 the ^{1}H-NMR spectra of the OLA purification series is shown. The blue graph represents the redispersed sample after synthesis with an excess of OLA. The proton resonances which can be attributed to OLA are broadened, with respect to the unbound OLA signal, indicating that OLA is bound to the NC surface. Importantly, the resonances of the alkene protons from the OLA carbon chain yield a resonance at about 5.5 ppm that shows no overlap with other resonances, either coming from different OLA protons or from residual solvent or contaminants. We can detect a small residual peak on the broad peak at 5.5 ppm in Figure 6.5, this indicates a small amount of free or unbound OLA . This is due to the fact that OLA will not evaporate by drying the sample with an airflow thus the excess OLA will still be present when redispersing the NCs in toluene.

By recording the NMR spectra under quantitative conditions, we could es-

timate the concentration of bound OLA from the integrated area of the alkene proton resonance. In addition, we combined the CZTS volume fraction in the NMR sample – as obtained using absorption spectroscopy – with the distribution of nanocrystal diameters as obtained from the analysis of 200 CZTS NCs on TEM micrographs. For this, an effective diameter distribution was determined by relating the projected surface area of the different NCs to an effective NC diameter, which is the diameter of a sphere yielding the same projected surface area. From this, average nanocrystal surface area per nanocrystal volume could be determined, which yields in combination with the ligand concentration a nominal ligand density – nominal since the CZTS nanocrystals were assumed to be spherical for this analysis. Importantly, although this nominal value can only be an approximation to the true ligand density, it correctly measures changes in ligand density provided the same nanocrystal dispersion is used throughout the different analyses.

Purification step	Ligands/nm^2
After Synthesis	3.8
1 time	3.7
2 times	3.2
3 times	2.8
4 times	2.2

Table 6.1: The amount of ligand present on the NC surface after a constituent amount of purification steps.

In practice, when subtracting the signal coming from the unbound OLA, we obtain a ligand density of 3.8 nm^{-2} for CZTS NCs with an excess of OLA. As shown in table 6.1, purification leads to a progressive loss of $\approx 15\%$ of the bound OLA present prior to each purification step. This provides us with a first indication that, although initially stable NC dispersion can be made, OLA can be stripped of the NC surface by a mere purification scheme at room temperature. After 4 purification steps, resulting in an overall ligand loss of about 40%, the CZTS nanocrystals are hard to redisperse. Probably, the reduced ligand coverage makes that the interparticle attractive forces start to dominate the steric hindrance provided by the remaining ligands. Moreover, issues with colloidal stability were not limited to excessively purified samples. In fact, each sample without an excess of OLA started to form a gel-like network or even nanocrystal precipitates over time. This indicates that CZTS nanocrystals tend to lose ligands up to a point where the colloidal stability is compromised, even if the initial ligand density appears sufficiently high. This was confirmed by further NMR-measurements, which shows that 2 times purified samples have a remaining ligand density of only 2.4 nm^{-2} after 10 days of storage, with the remainder of the originally bound ligands appearing now as freely dissolved ligands. We thus conclude that a substantial fraction of ligands

was stripped of the NCs upon storage.

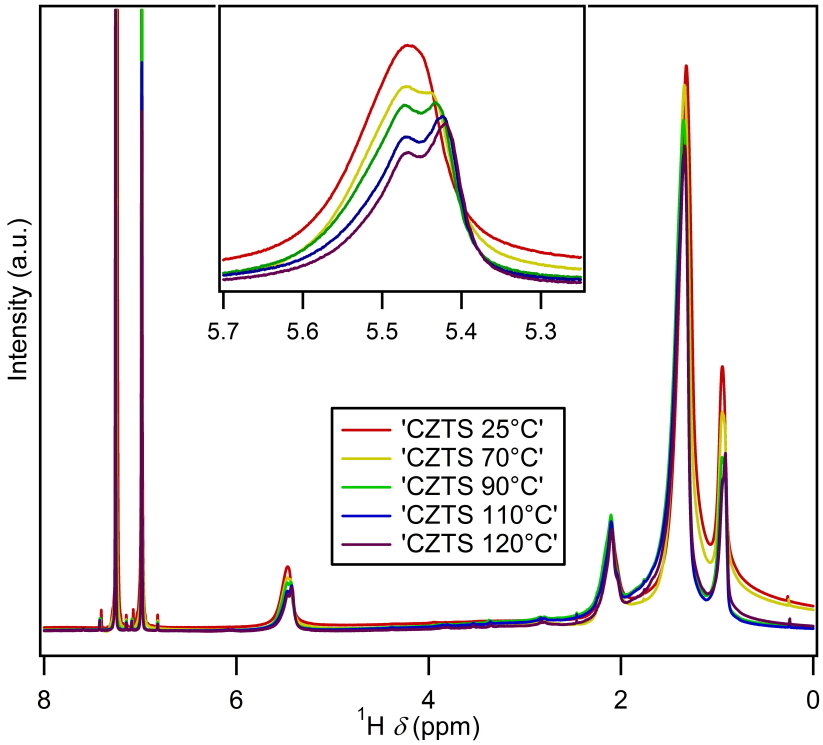

Figure 6.6: A freshly purified sample of CZTS NCs was dissolved in 1,2-dichlorobenzene-d_4 for in-situ heating NMR. The displayed spectra are 1D ^{1}H-spectra at different temperatures. The inset shows the characteristic double bound peak which has been integrated to quantify the spectra. The broad peak splits in 2 when heated, releasing unbound OLA giving rise to the sharper peak on the broad peak.

Possibly, a relatively high activation barrier for desorption prevents the rapid establishment of a dynamic equilibrium between bound OLA on the surface of CZTS NCs and free OLA in the solvent. This hypothesis we tested by recording the NMR spectrum of a CZTS sample while heating the suspension in-situ in the NMR spectrometer. As shown in Figure 6.6, heating indeed results in a ready release of free OLA, at temperatures lower than reported by Dierick et al. in the case of CIS nanocrystals [16]. Indeed, a clearly sharper resonance appears on top of the initial broad resonance of the OLA alkene protons (inset of Figure 6.6). When integrating this resonance and assuming that no OLA is lost from the sample, we estimate that up to 40% of the originally bound OLA has desorbed at a temperature of 120 °C. This is a significantly higher number then in the case of

CIS NCs, which suggests that the activation energy for OLA desorption is smaller with CZTS nanocrystals.

6.3.3 Conclusions

Based on the NMR study, it can be concluded that OLA is bound to the surface of the NCs but that desorption is possible even at room temperature. After 10 days at room temperature, the amount of desorbed OLA amounts to 40% of the originally bound. Although it remains unclear whether this is already a situation of thermodynamic equilibrium, it indicates that CZTS/OLA dispersions should be used shortly after their initial preparation unless an excess of OLA is added to the dispersion to maintain the originally high ligand coverage of the NC surface. This can be a disadvantage since the excess OLA will end up in CZTS NC films and will have to be removed in a later stage to form a thin film for solar cell applications.

6.4 Ligand Exchange to Coordinating Solvents

6.4.1 Thiols as Coordinating Solvent

As discussed in the previous section, an excess of OLA is needed to ensure long term colloidal stability of CZTS NC dispersions. This however is undesirable as it will increase the carbon content of the CZTS nanocrystal film to be eventually formed. A first alternative is the exchange of the original OLA ligands for other ligands. Here, the binding motif of both ligands plays a crucial part since, as indicated graphically in Figure 6.7a, L-type ligands can be exchanged for other L-type ligands and X-type of X-type while the replacement of an L-type ligand by an X-type ligand poses problems. However, a mere replacement of a first L-type ligand for a second will most likely lead to an new dynamic equilibrium between bound and free moieties, which does not really solve to original problem.

An elegant (but we should admit smelly) solution in this respect is the replacement of amines by thiols. Thiols have been shown to bind as L-type ligands, for example to CdSe and CIS NCs [16, 19]. Moreover, they can also be used as a solvent. This will push the adsorption/desorption equilibrium in the direction of full coverage of the NCs surface, thus increasing the shelf life of the CZTS NC dispersions and possible improving colloidal stability. Alkanethiols can be found with many different aliphatic chains, where shorter chain thiols have a lower boiling point – favorable to remove it from the NC film by mild thermal annealing – yet may only provide limited colloidal stability. We therefore choose octanthiol (OT) as a compromise. It has a boiling point of 200 degrees, which should lead to its removal from the NC film at modest annealing temperatures while C8 chains already tend to provide sufficient steric hindrance to stabilized nanocrystal dispersions. Moreover, the relatively low vapor pressure makes that OT has a smell less

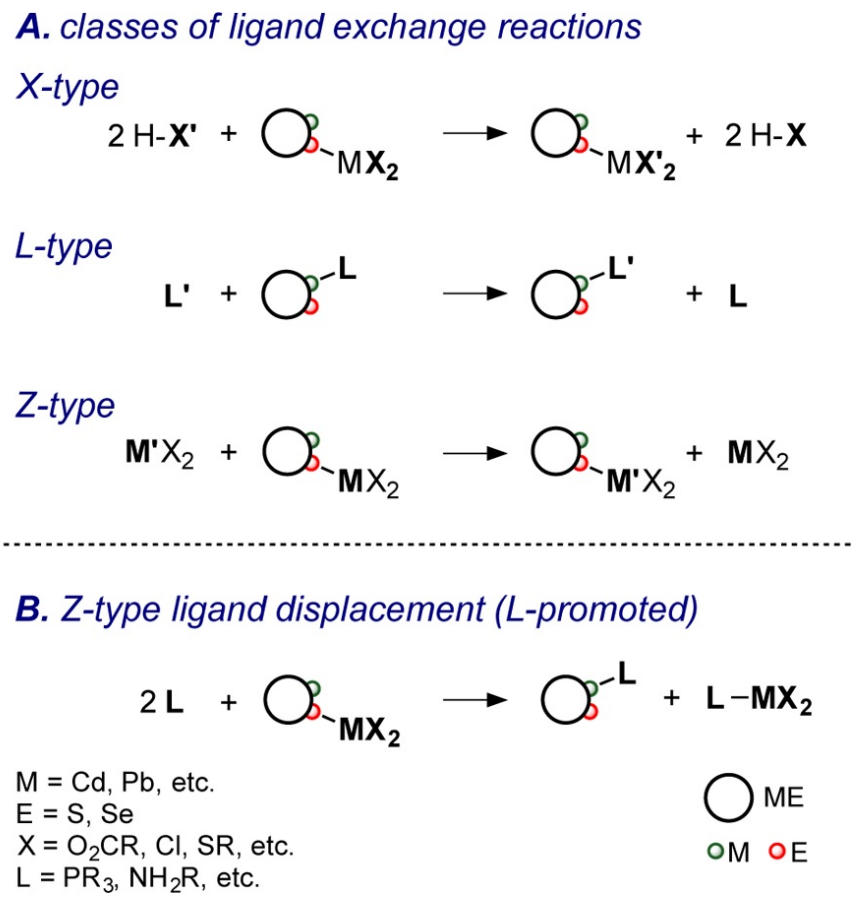

Figure 6.7: (A) Example Surface Ligand Modifications of Metal Chalcogenide NCs, Including X-, L-, and Z-Type Exchange (B) and Z-Type Ligand Displacement [18]

penetrating than, e.g., butane or hexanethiol (although it should still be handled under the fume hood).

6.4.2 Experimental

To test the viability of stabilizing CZTS NC dispersion using alkanethiols as a coordinating solvent, we exchanged OLA covered CZTS NCs by redissolving them in OT. For this, NCs are precipitated with ethanol and simply redispersed in OT. Slight heating has been applied to overcoming the desorption activation energy. Again, NMR samples were made by precipitating the NCs, drying them with an air flow and redispersing them in deuterated toluene. We fabricate 3 samples by precipitation and redispersion in OT 3 consecutive times. Again, it must be stressed

that the measurements were performed within half an hour after sample preparation since we used nanocrystals dispersed in deuterated toluene in stead of OT for the NMR measurements.

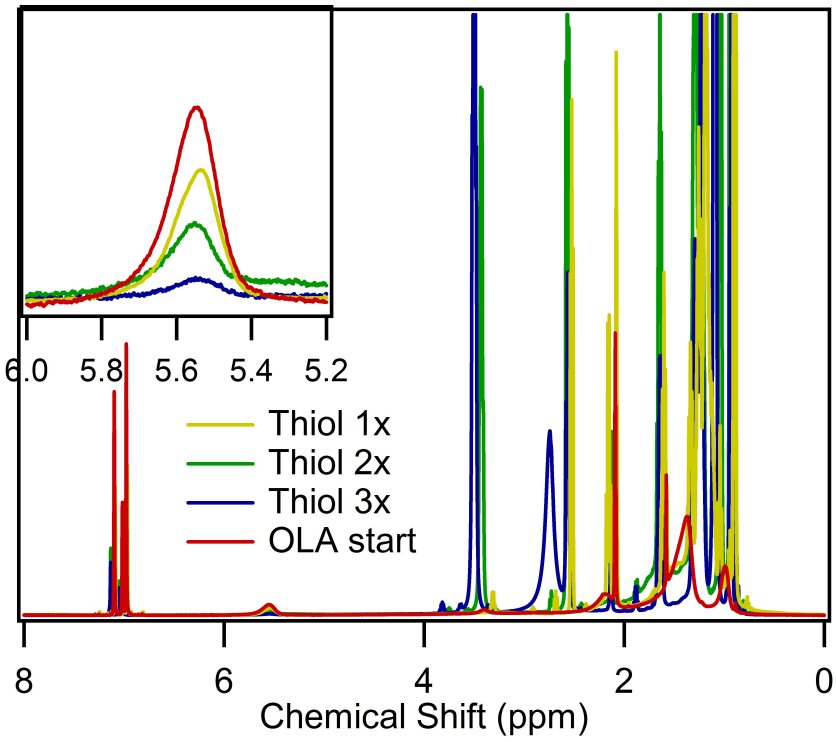

Figure 6.8: Red: OLA on CZTS NC after 1 purification step. yellow green and blue: constituent thiol ligand exchanges of CZTS NCs with an exchanging time of 30 minutes at 60 °C.

6.4.3 Results and Discussion

Results of the experiments intended to exchange the original OLA ligands for OT are shown in Figure 6.8. Again, we can use the distinctive resonance of the OLA alkene protons at 5.5 ppm to quantify the OLA loss. On the first exchange, we notice that 30% of the OLA has been removed from the surface. The two additional exchange steps each remove yet another 30% of the original amount of OLA until less then 10% of OLA remains after 3 exchange steps. As compared to the precipitation/redispersion steps where we stripped off ≈15% of OLA during each step, OLA removal is much more effective in this case. This may be due to the applied

heating, which facilitates the desorption of OLA, or to the possibility of replacing OLA by OT.

Quantifying the surface coverage of the CZTS NCs by thiols is difficult since free thiol is persistently present in solution. However, when dispersed in OT, one can presume that all available L-type binding sites are occupied by OT. This would mean that all nanocrystals are well passivated, resulting in a long term stable colloidal dispersion. In indication that this conclusion holds comes from an experiment in which a CZTS/OT dispersion was centrifuged after 10 days of storage. This operation did not result into any deposition of CZTS NCs at the bottom of the centrifuge tube, something which typically occurs in the case of CZTS/OLA dispersions.

6.4.4 Conclusion

We can conclude that we successfully exchanged the OLA coverage of CZTS NCs for octanethiol, which can be used as a coordinating solvent. We have chosen to replace OLA by shorter and more volatile thiols in the hope that the eventual CZTS film will have a lower residual carbon content. Importantly, CZTS/OT colloids proved to be stable over longer times, probably due to the large excess of OT in the dispersion.

6.5 Formulation of Nanocystal Dispersions with Carbon-Free Stabilizers

6.5.1 Anions as Charge Stabilizing Agents

In 2009 an old concept of stabilization was introduced for the stabilization of colloidal nanocrystals synthesized in apolar solvents. In first instance, tin chalcogenide complexes were used as a stabilizing agent capable of removing the organic ligands of as-synthesized nanocrystals such as CdSe quantum dots and charge-stabilizing the resulting nanocrystals in polar media [20]. Later, the same approach was demonstrated for a wide range of metal-free inorganic ligands, which were often small anions such as S^{2-}, HS^{-}, Se^{2-}, HSe^{-}, Te^{2-}, HTe^{-}, $TeS_3{}^{(2-)}$, OH^{-}, and NH^{2-}. [21]. In practice, the ligand exchange procedure is executed by means of a liquid/liquid two-phase system, in which the nonpolar phase contains the as-synthesized nanocrystals and the polar phase the carbon free ligands, typically as part of a dissolved salt such as $(NH_4)_2S$ or Na_2S.

For NCs of the CZTS family, we first explored this exchange procedure for CdSe NCs synthesized using oleic acid as the steric stabilizer. When the two-phase system is mixed (hexane/DMSO), a fast transfer of the NCs from the organic

phase to the polar phase occurs. We use sodium sulfide as a salt for the charge stabilization in the polar phase . This transfer involves the release of oleic acid from the ZnSe surface, the absorbing a counter ion (sodium), and replacing the oleate with sulfide anions. The sodium oleate shows more affinity with the toluene fraction and stays in this top phase. The NCs, now surrounded by charged molecules, transfer towards the polar phase. The oleate molecules providing 1 electron to the particle can be classified as X-type ligand, donating 1 electron. If we exchange the X type for a Z-type sulfide ligand can lend one of his 2 free electrons to bind on the NC. The free electron of the oleate molecule can bind the sodium atom released from the sodium sulfate. An example is shown in Figure 6.7. The top phase (hexane) containing CdSe NCs stabilized using organic ligands is mixed with a second phase (DMSO) containing sodium sulfide. After mixing the 2 phases the organic ligands are still present in the top phase, but the NCs have transferred and are now in the polar solution surrounded by sulfide anions.

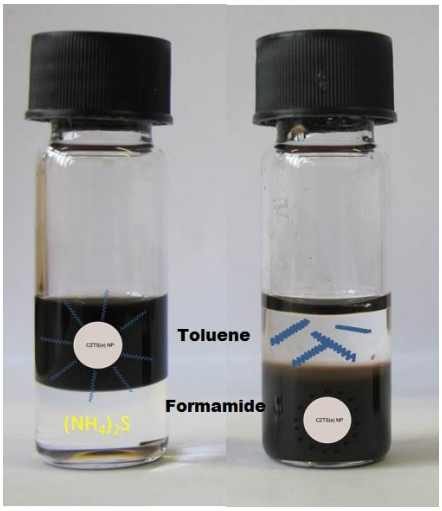

Figure 6.9: a CdSe example of phase exchange on NCs using ammonium sulfide .

6.5.2 Phase Exchanging CZTS Nanocrystals

The same experiment as discussed in the previous section has been performed using the CZTS NCs. A dispersion of CZTS NCs dispersed in toluene with OLA ligands was vigorously stirred with a formamide mixture containing sodium sulfide (see Figure 6.10). While the transfer of CdSe occurred almost instantaneously, the transfer of CZTS NCs is much more sluggish. Even after one hour, the toluene phase remained black and apparently no CZTS NCs had transferred to the for-

mamide phase. However, this situation changed after stirring the 2 phase system for 24 hours. In this case, the CZTS NCs accumulate after gentle centrifugation at the interface between both phases (see Figure 6.10). This situation seems to suggest that part of the OLA is still present on the surface of the NCs – keeping the NCs out of the polar phase – while sulfide anions started to adsorbe at the CZTS surface.

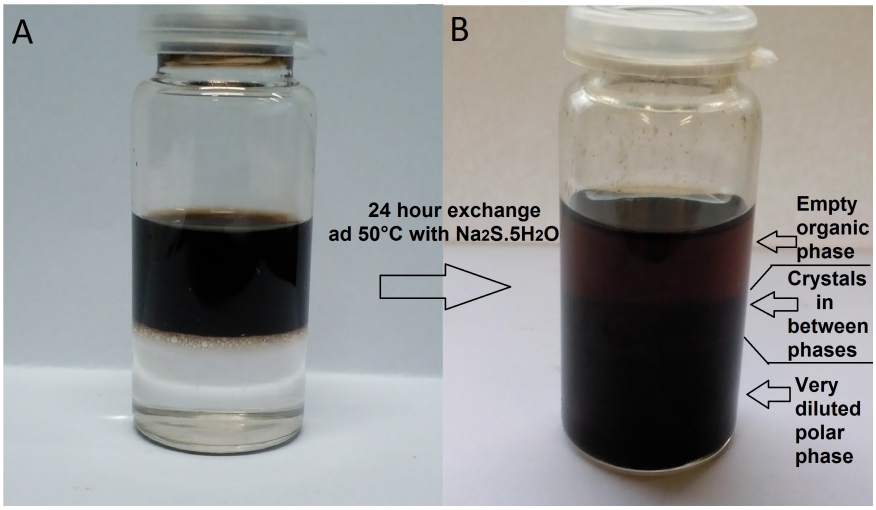

Figure 6.10: A: a picture of CZTS NCs toluene as a top phase and formamide containing sodium sulfide in the bottom phase. b: The same mixture after 24 hours of exchanging.

We attribute this markedly different behavior to the difference in surface chemistry between the CdSe and the CZTS NCs used. In the case of ZnSe NCs, the formation of sodium or ammonium oleate provides a ready pathway to exchange surface adsorbed oleate moieties for sulfide. CZTS NCs on the other hand are passivated by L-type OLA ligands. Opposite from oleate ligands, their exchange for sulfide ions cannot be driven by salt formation and the transfer of CZTS NCs to the polar phase can only be accomplished after the autodesorption of the original OLA ligands in the nonpolar phase. Clearly, this process can lead to intermediate situations where the NCs accumulate at the polar/nonpolar interface. Knowing this, we developed a new exchange procedure aimed at removing OLA as much as possible from the CZTS NC surface. This involves the repetitive heating of the toluene-based CZTS dispersion to 100 °C, followed by NC precipitation using cold ethanol, centrifugation, decantation and the redispersion of the pellet obtained in toluene. This procedure is repeated until the resulting CZTS NCs pellet fails to redisperse in toluence, which we attribute to the excessive loss of OLA. To the obtained NC pellet, we subsequently added a mixture of DMSO, ammonium sulfide mixture (colored dark blue) and toluene, which was left stirring for 10 hours at a

temperature of 50 °C. The resulting dispersion could be destabilized by addition of isopropanol and the NC pellet obtained after centrifuation and decantation could be dispersed in DMSO.

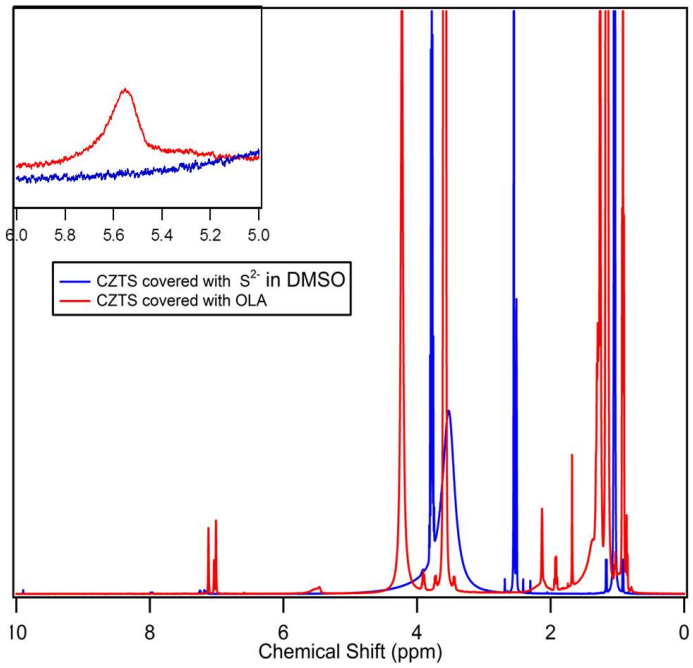

Figure 6.11: An Overlap of a ^{1}H-NMR spectrum of CZTS NCs with OLA and A ^{1}H-NMR spectrum of CZTS NCs in DMSO

We looked for further inside in the effect of the proposed procedure on the surface chemistry of the CZTS nanocrystals using solution NMR and elemental analysis. Figure 6.11 compares the ^{1}H-NMR of the original OLA stabilized CZTS NCs in toluene-d_8 (see Section 6.3) with the resulting charge stabilized NCs in DMSO-d_6. The spectrum of the OLA covered CZTS NCs (red) mainly features resonance of residual toluene and OLA. The spectrum of the CZTS NCs in DMSO on the other hand shows a broad resonance pertaining to traces of water and sharp resonances of isopropanol and residual DMSO. However, no traces of OLA can be detected, which confirms that the proposed process leads to the complete removal of the original OLA ligands. To further analyze these results, we used CHNS analysis to determine the carbon content in a dried precipitate of the DMSO ink. It follows that these residues only contain 0.47 wt% carbon on the total sample weight is left, this compared to the 34,5 wt% of carbon on a non-exchanged precipitate. Indicating that the organic steric stabilizers have been removed. It thus appears that apart from DMSO residues, this precipitate is in essence carbon-free.

After phase transfer to DMSO, the CZTS NCs are supposed to be charge stabilized by the adsorption of sulfide anions to the CZTS surface. This assumption is confirmed by the analysis of the zeta potential, which amounts to -67 mV. This indicates that the repulsive interactions are sufficiently strong to prevent aggregation of the CZTS NCs and thus ensure colloidal stability.

6.5.3 Conclusion

Based on an understanding of the CZTS NC surface chemistry, we have developed a process enabling the transfer of as-synthesized NCs from an nonpolar to a polar phase. The process is designed to desorb as much as possible the original L-type ligands (OLA) and eventually replace them by sulfide anions. This results in charge stabilized CZTS dispersions in DMSO, in which the NCs exhibit a strongly negative zeta potential.

7

The Behavior of Nanocrystal Inks

7.1 Introduction: Ink Flow Behavior

In the previous chapter, we studied dispersion stability at the level of the individual NCs and the chemistry of the NC surface using mainly ^{1}H-NMR. We found that dispersing the CZTS NCs in apolar mixtures with an excess of OLA or in pure thiols leads to CZTS NCs with surfaces fully covered by ligands. However, this full surface passivation is lost during long-term storage – at least in the case of OLA – and after repetitive purification steps. In this chapter, we will study the effect of the CZTS ligand and ligand coverage on the overall behaviour of the NC dispersion or ink, where a central question is at what point the attractive interactions start dominating and compromise the ink stability.

As explained before, steric or electric stabilization is supposed to counteract the attractive interactions between NCs, resulting in a dispersed, weakly flocculated or strong flocculated dispersion. A convenient way to address the overall ink stability and the underlying interparticle attraction/repulsion balance is to study the rheological properties of the ink. During rheological measurements, the flow behavior of the ink in response to an applied stress is monitored. The dispersion stability and the structure of possible aggregates can be derived, e.g., from the dispersion flow viscosity (η) as a function of the shear rate. This dependence directly reflects interparticle interactions in a colloidal dispersion, where depending on the interparticle interaction different types of flow behavior occur [1].

The three most important flow behaviors are shown in Figure 7.1. These cor-

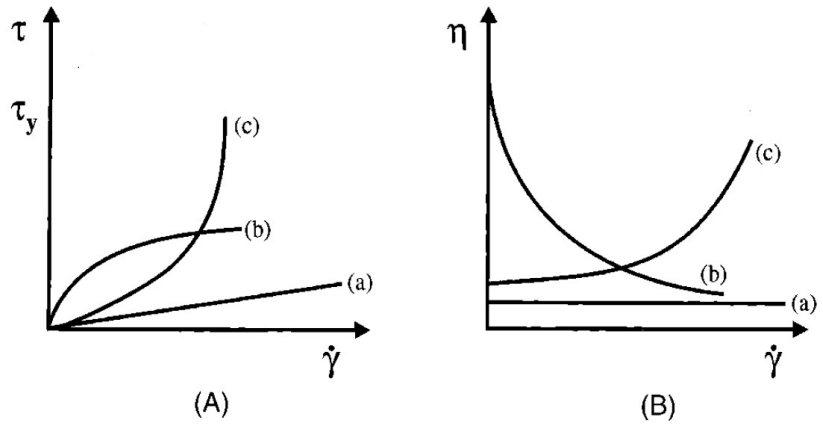

Figure 7.1: Types of rheological behavior exhibited by colloidal dispersions: (a) Newtonian flow (b) shear thinning (c) shear thickening [1]

respond to:

- *Newtonian flow behavior*. For Newtonian liquids the viscosity of the medium is independent of the applied force. This means that a linearly increasing shear force must be applied to maintain a linearly increasing shear rate. This behavior is characteristic for stable colloidal dispersions where dispersed particles exhibit little attractive interaction, if any.

- *Pseudoplastic or shear thinning behavior.* In this regime, the viscosity drops with increasing shear rate. With colloidal dispersions, this typically occurs when particles show significant interparticle attraction. With no or low shear rates, particles will interact and form particle networks, which contribute to the dispersion viscosity. When increasing the shear rate, these networks will break down and the viscosity will concomitantly drop.

- *Dilatant or shear thickening behavior.* This behavior occurs when repulsive particle-particle interactions keep the particles in an ordered, layered, equilibrium structure at no or low shear rates. However, once the shear rates exceeds a critical level, the shear forces can overcome the repulsive particle-particle interactions and a disordered particle organization results. This leads to a viscosity increase, which can be undone by removing the shear force.

In summary, stable inks containing well dispersed NCs will show Newtonian behavior. In the case of weakly flocculated suspension at low concentrations, the small clusters will not be sufficiently close to form interparticle networks and

again, Newtonian flow is expected. Dispersions in which interparticle attraction is dominant on the other hand will show a markedly increased viscosity at low shear rates, which drops at higher shear rates due to the breaking of the formed aggregates.

Telling apart stable dispersion containing individual nanocrystals or dispersed nanocrystal aggregates by rheological measurements may be hard since the inks used here have a very low viscosity and the influence of flocculation on their behavior may be minimal. We therefore propose to use 2 additional techniques to monitor possible particle flocculation. First, the hydrodynamic radius of the dispersed particles or particle aggregates can be determined via Dynamic Light Scattering (DLS) as soon as they are sufficiently small to show Brownian motion. Second, dark field (DF) optical microscopy can be used to demonstrate aggregate formation. Although individual CZTS NCs are too small to be seen using a DF microscope, aggregates of CZTS NCs may scatter light sufficiently strong to be observed. In this way, DF microscopy can provide a rapid first indication of the state of the dispersed particles (individual NCs or NC aggregates). Also more heavy flocculation can easily be studied. When the crystals flocculate in the secondary minimum of the total interparticle interaction we will be able to see the Brownian motion of the metastable clusters. However, when more pronounced flocculation occurs the clusters will precipitate and lose Brownian motion. This results in the formation of immobile structures clearly visible under the microscope, an indication of destabilization of the ink.

7.2 Experimental

We used similar dispersions of CZTS NCs as in Section 6.3 of the previous chapter. The main difference is that we replace toluene with dodecane as a solvent to improve drying behavior. Rheology measurements were conducted using an Anton Paar Rheoplus system. A cone/plate measuring system was used to measure the viscosity. We first applied a pre-shear to break all existing structures and networks. After the pre-shear, we measure in a shear controlled way the viscosity of the ink, lowering the shear rate form 2000 - 2 s^{-1}.

DLS measurements were conducted on a Malvern Zetasizer. We could measure the diameter directly with the ink without need for further dilution. The DLS measurements were performed immediately after redispersion to make sure no new dynamic equilibrium could be formed due to ligand loss.

Dark field (DF) microscopy was done by placing a droplet of the ink between 2 microscopy slides. This was done using bottom illumination with white light.

7.3 Results and Discussion

7.3.1 CZTS Nanocrystals Stabilized with OLA

For the rheological and DLS studies on OLA capped CZTS nanocrystals dispersions, we replaced toluene by dodecane as the solvent to have a solvent that shows as large as possible an affinity for the used ligand. Since OLA and dodecane both have an aliphatic chain, it is therefore preferred over toluene based on the like-dissolves-like principle. Furthermore, the solvent should not be too volatile, but still it should evaporate upon modest annealing. Dodecane has a boiling point just over 200 °C and a low vapor pressure and thus makes an excellent choice, especially since it is inert and non-toxic.

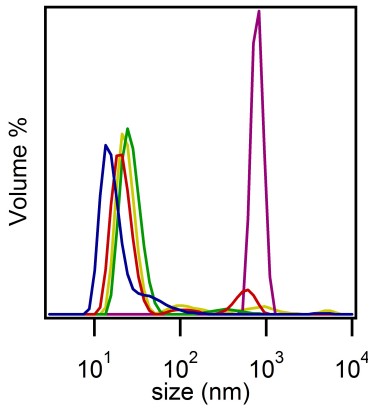

Figure 7.2: DLS measurements of a purification series using OLA as a ligand. Blue: OLA excess Green :1 purification step, yellow: 2 purification steps, red: 3 purification steps, purple: 4 purification steps

As shown Figure 7.2, DLS measurements on CZTS NCs dispersed in dodecane with an excess of OLA show a unimodal size distribution with a Z-average diameter of 40 nm. Based on the TEM micrographs of the CZTS NCs as shown in Section 5.1.1, we thus conclude these dispersions contain individual CZTS NCs without significant aggregation. This is confirmed by the DF microscopy image, which shows a homogeneous, brown liquid without visual Brownian motion (see Figure7.3a). One or two purification steps do not significantly change this picture. The Z-average of the size dispersion slightly increases from 42 nm to 54 nm and a small amount (1-2%) of larger clusters appears in the size distribution (see Figure 7.2). These clusters lead to some minor scattering in the DF microscopy images, as shown in Figure 7.3b. In line with these findings, dispersions of CZTS NCs stabilized with OLA and with excess OLA added behave as Newtonian liquids. Note

that the viscosity of the dispersions is almost identical to that of dodecane, which amounts to $\approx$ 1 mPa. at 25 °C (see Figure 7.4). We thus conclude that these dispersion contain well dispersed CZTS NCs which show little, if any, interparticle attraction.

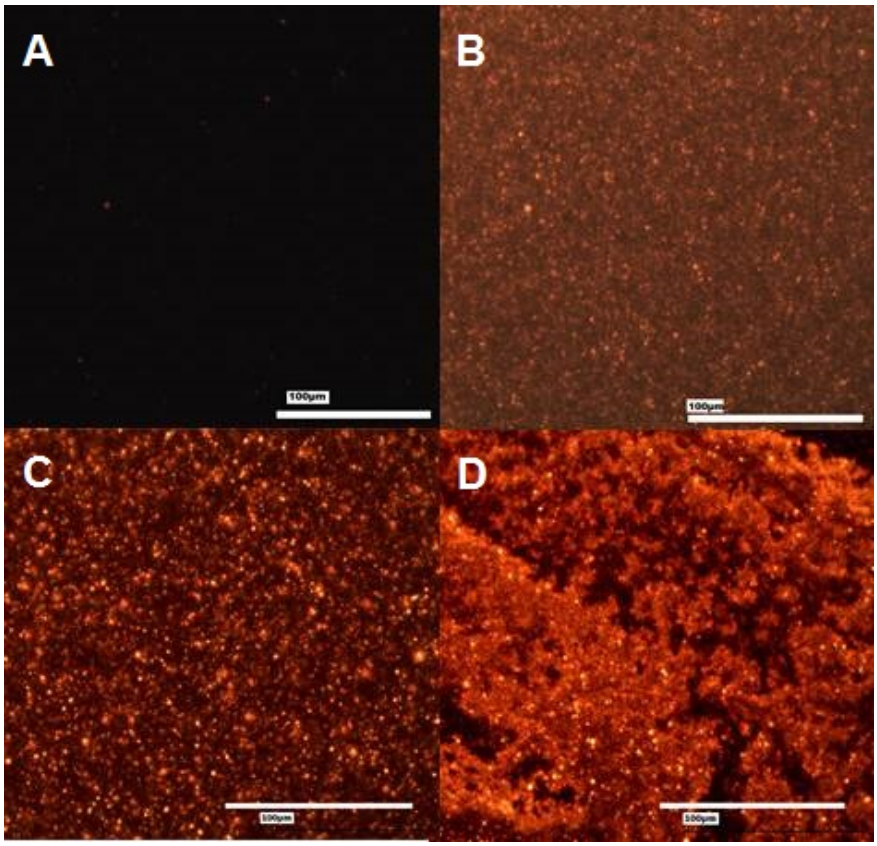

Figure 7.3: A: DF image of CZTS NCs with an OLA excess. B: DF image of CZTS NCs with 100-80% surface coverage DF image. C: DF image of an ink with 30% OLA loss on the CZTS NC surface. D: +40% OLA loss on the CZTS NC surface, resulting in the settling of clustered structures

After 3 purification steps a more significant portion of clusters appears in the DLS-derived size distribution and the Z-average diameter increases to 320 nm. This indicates that when $\approx$ 30% of the OLA ligands has been removed (see Section 6.3.2) interparticle attraction becomes dominant, resulting in NC clustering. However, these inks maintain their Newtonian behavior flow behavior and their viscosity remains close to that of dodecane (see Figure 7.4). The combination of both observations suggests that the clusters may reflect the occurrence of a sec-

ondary minimum in the potential energy diagram. This could be understood from the significant loss of bound OLA, which may leave parts of the NC surface with little or no ligands. The concomitant loss of steric repulsion can lead to NC aggregation, yet the ensuing removal of sparsely covered surfaces increases the average ligand coverage on the NC surfaces exposed to the solvent. This increases the repulsive steric hindrance between approaching aggregates, which reflects itself in the secondary minimum in the free energy profile. The view on the CZTS NC ink after 3 purification steps as a stable dispersion of NC aggregates is confirmed by DF microscopy images, which mainly shows clusters exhibiting Brownian motion.

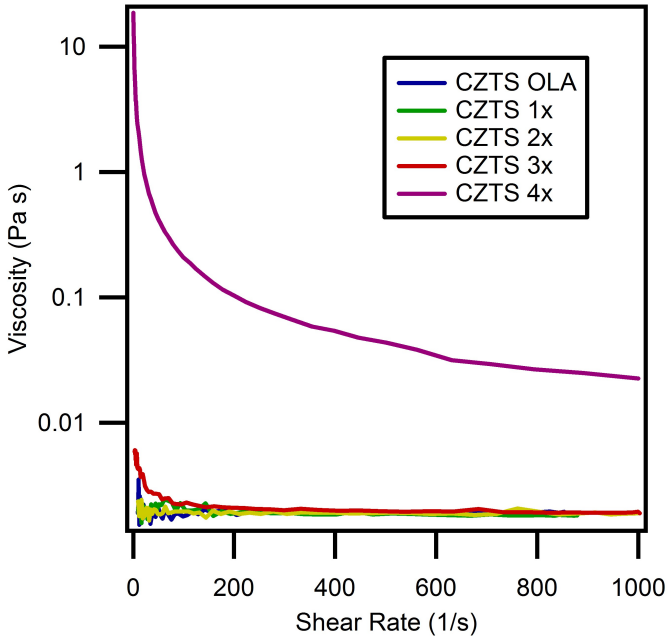

Figure 7.4: The viscosity of OLA capped NCs in function of an applied shear rate.

A 4^{th} purification step, which involves the accumulated loss of 40% of the original ligand density, results in the complete clustering of the NCs. The Z-averaged DLS diameter has increased to nearly 1.5 μm. DF microscopy reveals that the clusters have become too big to show Brownian motion and they settle as large aggregates. It thus appears that a threshold has been surpassed where the level of OLA loss leads to extensive and uncontrolled nanocrystal aggregation. The flow behavior of these dispersions exhibits a marked shear thinning, where an already high viscosity at high shear rates further increases when reducing the shear rate as NC clusters are formed.

As a final remark, we note that all measurements discussed here have been

preformed within 30 minutes of the redispersion step in dodecane. However, we found that all OLA based samples eventually showed structure formation, with the sole exception of the sample with an OLA excess, which remained clear under the DF microscope even after months of storage. This means that the dynamic equilibrium, which strips OLA of the NC-surface over time as seen in Section 6.3, has an negative influence on the dispersion stability. It appears that the inevitable desorption of OLA from CZTS NCs will always compromise ink stability, which strongly restricts the shelf like of these CZTS dispersions. As-synthesized, OLA stabilized CZTS NCs should therefore be stored as a dry NC powder or in dispersions to which an excess of OLA has been deliberately added.

7.3.2 CZTS Nanocrystals Stabilized With Thiols

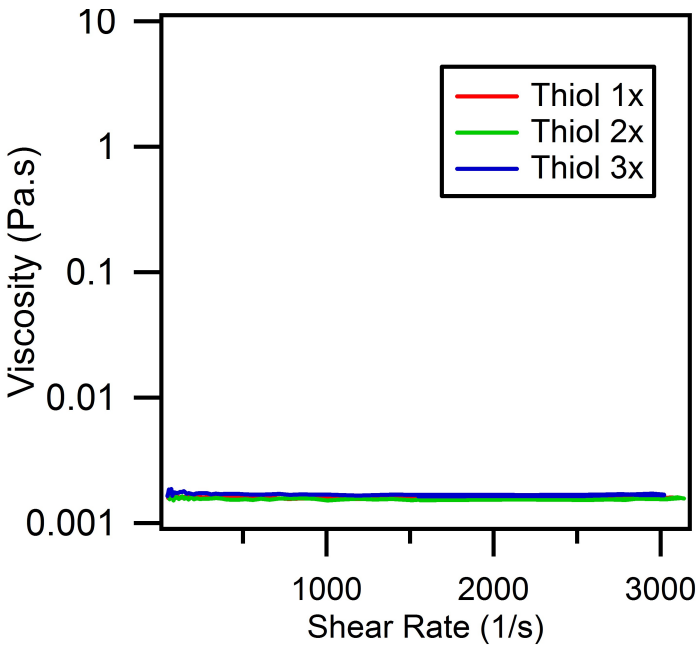

Figure 7.5: The viscosity of the exchanged thiol samples in function of shear rate. The ink show Newtonian liquid behavior, indicating no interactions between the crystals.

Since NCs with a fully covered OLA shell are dispersed as individual NCs that show Newtonian flow behavior, we expect a similar behavior for thiol capped NCs. We therefore analyzed the rheological behavior of 3 thiol-based NC dispersions with 60%, 30% and 10% of the original amount of OLA still present, respectively. The same samples were used for the NMR analysis as discussed in Section 6.4.1. All 3 dispersions showed Newtonian flow behavior as can be seen in Figure 7.5.

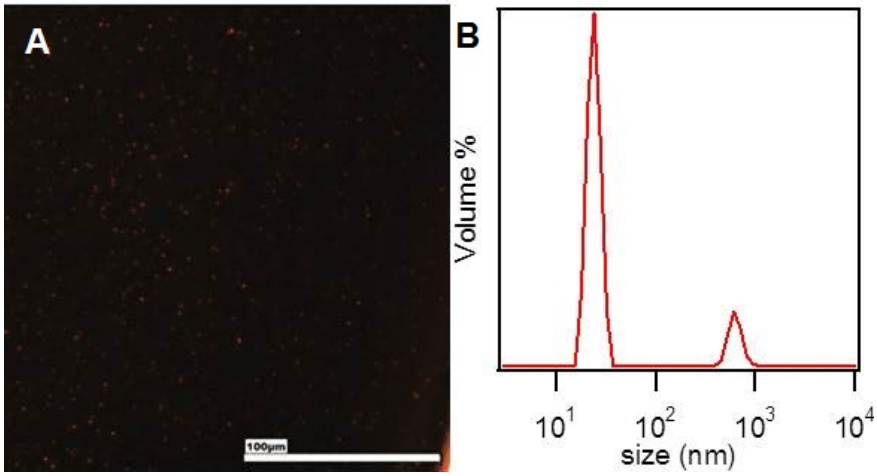

Figure 7.6: A: A DF microscopy picture of a thiol capped CZTS ink. B: DLS of A thiol capped ink which shows very limited clustering.

Furthermore, the thiol based inks show a largely unimodal DLS-derived size distribution with a Z-averaged diameter of 28.5 nm. This points again towards well dispersed NCs, with only a slight fraction of stable small clusters present (see Figure 7.6). In the same figure, the DF microscope image confirms that these clusters are only present in tiny amounts and exhibit Brownian motion. Even after a few days, no further cluster formation occurs and the ink remains stable. These findings are hardly surprising since the solvent also acts as the stabilizing agent, which implies that the nanocrystal surface will maintain a high ligand coverage. Note that as compared to OLA-based inks, thiol-based inks could be kept for months without a change in colloidal stability.

7.3.3 Carbon Free CZTS Nanocrystals

Exchange of OLA for sulfide stabilization results in a CZTS NC dispersion in DMSO in which the NCs are stabilized by charge, supposedly by the preferential adsorption of sulfide ions. As discussed before, the zeta-potential of these dispersions amounts to -67 mV, which seemingly suggests that the NCs form a stable ink, without clustering. However, when analyzing the ink via DLS, we find that the NCs are not dispersed as individual NCs, but form clusters with a Z-average of 616 nm (see Figure 7.7b). These clusters are also visible under the DF microscope (see Figure 7.7a), but unlike the heavy clustered samples in the OLA based ink, these clusters stay in Brownian motion over time. These observations are confirmed by rheology measurements, in which DMSO based inks appear as Newtonian liquids (as seen in Figure 7.8). Although the ink contains NC aggregates, these clusters

from a stable colloid and are not attracting one another.

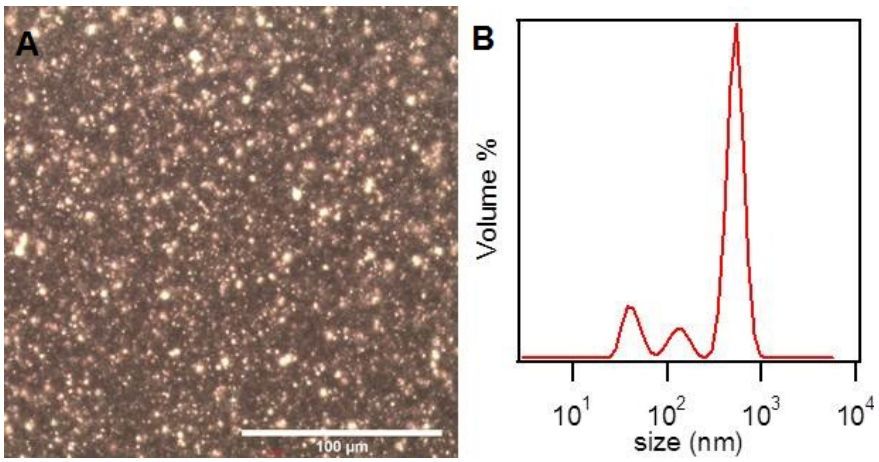

Figure 7.7: A: DF microscopy picture of CZTS NCs stabilized using sulfide anions. B: A DLS measurement of the same sample

The appearance of CZTS NC clusters may not be too surprising in view of the ligand exchange process described in section 6.5.2. Before we transferred the NCs to DMSO, we first stripped up to 60% of the OLA of the surface. In section 7.3.1, we already showed that NCs with that amount of ligands stripped off tend to cluster. It thus appears that the phase transfer to DMSO is applied to CZTS clusters, rather than to individual CZTS NCs. The imposed stirring during the phase transformation does not give enough energy to break the clusters to the level of individual NCs. Even after an ultrasonic bath treartment the NCs remain clustered. Nevertheless, this resulting colloid of aggregated CZTS NCs appears well stabilized by charge. Note that in spite of their colloidal stability, the clusters are so large that they suffer from slow gravitational precipitation. The ink therefore requires some stirring or ultrasonic treatment before use.

7.4 Conclusion

In view of ink formulation, we found that the loss of OLA ligands from the CZTS NC surface has a significant effect on the stability of CZTS NC inks. As long as sufficient OLA remains on the NC surface (100-80% coverage) a stable sterically stabilized solution with individually dispersed NCs is retained . When more ligand is stripped of the surface (80-60% coverage), NCs form clusters yet the ink remains stable. However, when further reducing the ligand coverage (-60% coverage), we found that CZTS inks turned unstable and all NCs flocculated. This resulted in a significant increase of the ink viscosity and the formation of large, aggregated

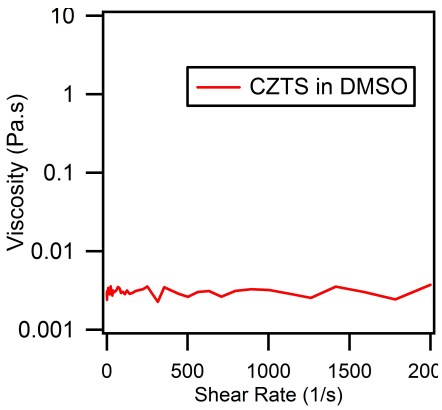

Figure 7.8: A rheology measurement of a sulfide based ink of CZTS NCs. Indicating a Newtonian flow behavior.

structures. Importantly, all OLA based inks – with the exception of inks with an excess of OLA – showed signs of precipitation over time, which we linked to the gradual desorption of OLA ligands. We found that for a long term stability, thiols are a good alternative for OLA based inks, where the ample supply of ligands prevents aggregates from forming. Finally, we observed that the C-free inks are composed of charge stabilized nanocrystal clusters, which is most likely linked to the transfer protocol in which a significant amount of OLA needs to be stripped off the NC before they transfer to a polar solvent.

8

Deposition of CZTS Thin Nanocrystal Films

A key element in solution-based processing is the formation of a high quality layer of the desired material. The printing of thin films involves a considerable cost reduction as compared to vacuum-based processes, yet the deposition of crack-free, smooth precursor films is often highly challenging. In the previous sections, we have shown how stable NC inks can be formulated using 3 different stabilizing agents. The next step involves the analysis of film deposition, using these 3 different inks.

8.1 Available Deposition Techniques

To deposit thin films, multiple deposition techniques are available, where we will focus on wet film deposition in this thesis. This is a two step process, involving the deposition of the precursors in a wet film and the subsequent drying of this film. Three deposition techniques were used in this thesis, namely dropcasting, doctor blading and inkjet printing.

8.1.1 Dropcasting

Drop casting is probably the most basic way of forming a wet film. It involves the dropwise deposition of a predefined amount of the ink on a substrate, typically using a syringe or a pipet. The ink spreads over the substrate and is allowed to

dried. Drop casting is a well suited for rapid, lab scale testing since it requires not more then a pipet to deposit the ink and it has the advantage that a known amount of ink (and thus precursor material) can be deposited on the substrate. This enables the final layer thickness to be calculated, if an equal spreading of the ink over the substrate is assumed. An example of a dropcast film after drying of the wet film on a hot plate is shown in Figure 8.1.

Figure 8.1: A dropcasted layer of CZTS NCs

Important disadvantages of dropcasting are that the ink needs to be sufficiently fluent. A viscous ink will not spread over the substrate, leaving parts of it uncovered and if it is covered often with a film of varying thickness. Also the deposition of very thin films is difficult since there has to be sufficient ink to wet the entire substrate. If not, surface tension will tend to contract the film. However, since dropcasting is a straightforward and fast method, we use it for first deposition test.

8.1.2 Doctor-Blading

Doctor-blading is a technique that can overcome some of the disadvantages of drop casting. Here, a blade is moved horizontally over the substrate with a known gap separated the blade edge from the substrate. Ink deposited on the substrate is spread over the surface. The layer thickness can be controlled by carefully setting the width of the gap and speed of the blade. Compared to dropcasting, doctor blading allows viscous solutions to be homogeneously spread over the surface. A disadvantage is that when the blade scrapes the surface, part of the ink is removed, leaving only the set gap to determine the possible layer thickness. A picture of the setup used for film deposition by doctor blading with a variable blade gap is shown in Figure 8.2.

Figure 8.2: A docterblading setup using a blade with variable height

8.1.3 Inkjet Printing

In collaboration with the SCRiPTS group of Ghent University were able to use a inkjet printing system. Inkjet printing is a more advanced technique for layer deposition. An inkjet printer generates very fine droplets that can be cast on the substrate, generating thin films in a reproducible way. Here, we made use of a Dimatix printer with 16 piezoelectric nozzles (picture in Figure 8.3), where very small movements of a piezo electric element are used to generate the extremely fine droplets to be cast on the substrate. The printer allows us to spread the surface with the thinnest layer. Attempts to generate a layer with the same thickness using drop casting or doctor blading resulted in partially covered substrates only. Next to the ability to generate very fine droplets, a printer has an on demand printing possibility, allowing us to print patterns, yet this possibility was not used in this thesis [22].

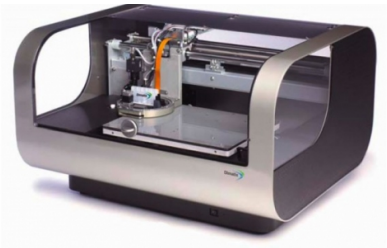

Figure 8.3: A picture of the Dimatix printer used for layer by layer deposition

8.2 Deposition of OLA Stabilized Films

8.2.1 Experimental

In a general procedure, the OLA stabilized CZTS NCs have been deposited via drop casting. Here, we first calculated the amount of ink required to form a 1.5

μm thick film on an 2.5$\times$2.5 cm^2 substrate using a 5 wt% dispersion. We used Mo coated glass substrates, which were washed using a 20% NH_4OH sollution. Initial drop cast experiments made clear that the ink spreads homogeneously over the Mo coated substrate. After formation of the wet film, the substrate is gently heated to 75 °C and dried for 1 hour in air, which suffices to obtain a layer with a dry appearance. A second heating step of 300 °C is subsequently applied under inert atmosphere.

Following the procedure outlined in Chapter 5.1.1, we deposited layers using OLA enriched inks and inks with OLA-NCs after purification (up to 4 times). All the purified OLA-NC dispersion (1 to 4 times) were deposited directly after redispersion with an ultrasonic bath to prevent the ink from destabilization by ligand desorption. All samples where analyzed using scanning electron microscopy (SEM), where top-view images and cross-sections were recorded to determine the film homogeneity and thickness. In addition, CHNS analysis was used to determine the total amount of carbon present.

8.2.2 Results and Discussion

The OLA enriched NC ink yielded a film with an oily and wet appearance after drying at 75 °C, which we attribute to an excess of OLA in the layer. When the layer is dried at 300 °C, a grey smoke is observed which probably points towards the evaporation of residual organic material. SEM images of the layers are shown in Figure 8.4b. The layer deposited with the excess of OLA has a bumpy surface with small craters and a thickness of 1.7 μm, as can bee seen on the cross sectional SEM images in Figure 8.4A. CHNS analysis indicates that this layer contained up to $\approx$ 35wt% of carbon before heating at 300 °C. After heating, the carbon content remained significant at about 19%. Most likely, it is this removal of carbon leads to the formation of the small cracks and craters visible in Figure 8.4b. Deposition using the purified CZTS inks where ligand loss was restricted to 10-20% of the original amount of ligands gave a promising result. Both layers are smooth, with a thickness of 1.5-1.7 μm (see Figure 8.4C), which is in accordance with the calculated thickness. When depositing a film with the 30% ligand loss ink, small cracks occurred in the layer (see Figure 8.4d).

As compared to literature values, depositing a 1.5 μm thick film from 25 nm CZTS NCs is far from obvious [23, 24]. Cima et al. showed for example that a linear relationship exists between the particle size and the critical cracking thickness of a layer made of these particles. Tirumkudulu et al. applied this theory to silica nanoparticles with a diameter of 22 nm (similar in size to our NCs) and found a critical cracking thickness (CCT) of 400 nm. To understand why films with a thickness up to 1.7 μm could be formed from 25 nm CZTS nanocrystals, a better insight in crack-formation is needed. Cracks develop during the film formation

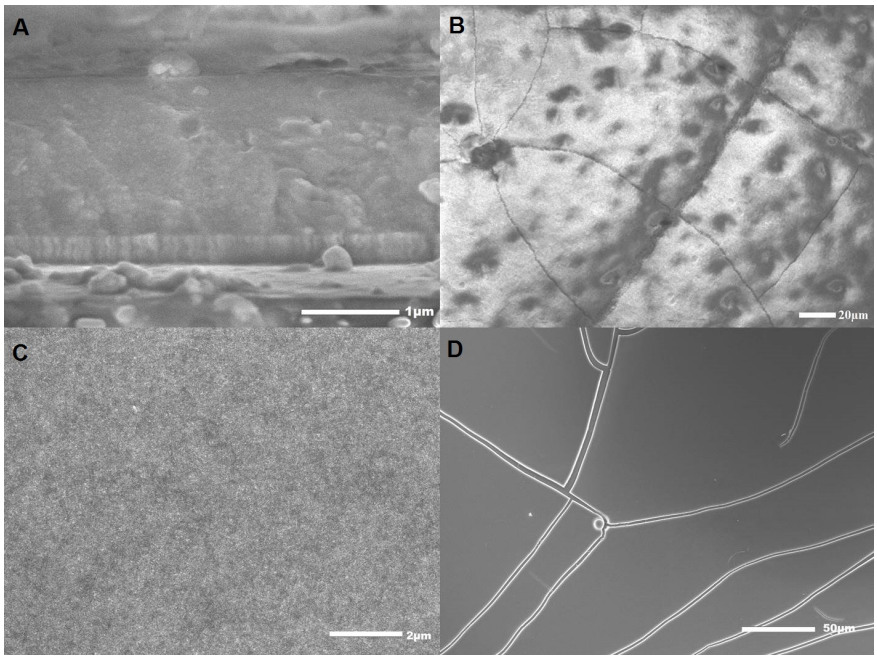

Figure 8.4: A: The cross-section of a CZTS deposited layer. B: A layer of CZTS NCs with large excess of OLA. C: An layer without OLA excess but fully covered NC surface forming a crack-free layer. D: The cracked layer of CZTS NCs with 30% OLA loss.

when the normal stress imposed by the removal of the solvent through interfacial tension induces a transverse tensile stress in the plane of the film (an example of tensile stress on a film is shown in Figure 8.5a). If that stress exceeds the strength of the close-packed network of substrate-bound particles, the film will crack. The normal force is the force resulting from the attractive forces between the neigbouring particles as shown in Figure 8.5b. The physical quantity that expresses the result of these internal forces between particles is the normal stress. This means that higher normal force values, and thus more interparticle interaction, leads to higher stress on the film and to a faster crack formation.

The silica particles used in literature were charge stabilized. When the solvent evaporates the particles lose their repulsive potential and the particles start touching each other. This means that the VDWL attractive forces play an important role and without a repulsive force present normal stress increases (See Figure 8.5b). If the particles are smaller a higher amount of contact points - where VDWL forces are applied - are available. This explains why films fabricated using smaller particles crack faster and thus have a lower CCT. The upper limit of 400-500 nm has been shown for particles of 25 nm. However, in our case we were able to deposit a layer of nearly 2 μm. We can find an explanation in the stabilization method.

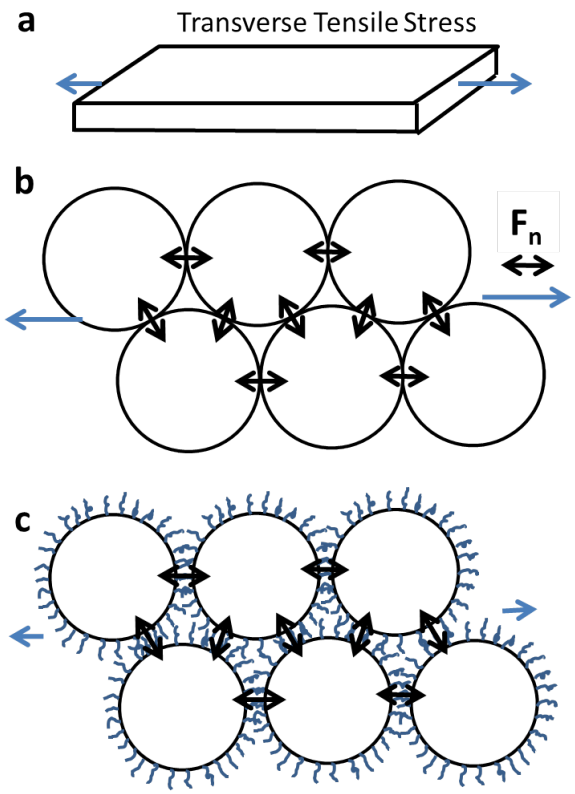

Figure 8.5: a: Graphical representation of a tensile stress on a film. b: Graphical representation of the normal force en resulting stress in a particle film without sterical stabilization and c: with sterical stabilization.

The CZTS NCs used here are dispersed as individual NCs, sterically stabilized by a ligand shell of organic ligands covering their surface. These ligand shells shield the VDWL interactions between neighboring NCs. This means that the interparticle interaction in the film is much lower and the resulting tensile stress will be lower, enabling films up to 5 times thicker than expected to be formed [23, 25] (see Figure 8.5c). This effect is similar to the effect that organic binders have upon film formation and is described in literature.

When the amount of OLA on the surface is reduced, the drying NCs have difficulties to maintain a crack-free film during drying. When the OLA content is reduced by 30% the film cracks at 1.5 μm. An example of such a film can be seen in Figure 8.4d. However, reducing the thickness of the film by half still allowed us to form a crack-free layer. The cracking can be explained by the increasing

VDWL forces between the NCs in the dried layer due to ligand loss. Therefore, the thickness had to be reduced in order to lower the tensile stress.

All results obtained with OLA based layers have been summarized in Table 8.1, which also includes the carbon content before and after the heat treatment since this gives us an idea of the amount of binder remaining in the final layer.

% of OLA Loss	C% 75 °C	C% 300 °C	Clustered?	CCT
$\geq$ 30%	34%	11.2%	No	1.7 μm
0%	23%	8.6 %	No	2 μm
-10%	19.6%	7.6%	No	1.5μm
-20%	16.9%	7.1%	slightly	800 nm
$\leq$ -30%	7.6%	3.1%	Yes	<400

Table 8.1: Overview of the inks and their properties. The left column represents the relative excess of OLA compared to the fully covered OLA surface. The second column is the residual C after drying at 75% degrees and the third column after 300 degrees. the final collomn represents the experimental critical cracking thickness of the deposited layer.

8.3 Deposition of Thiol Stabilized Films

8.3.1 Single Layer Deposition with Thiols

The thiol based inks were dropcasted similar to the OLA-based inks. After drying at 75 °C, a dry, smooth and crack-free layer is obtained, presented in Figure 8.6a. Here, it was also calculated to obtain a 1.5 μm layer of 25 nm NCs. The possible formation of this thick layer can be explained similar to the OLA covered NCs. The thiol reduces the VDWL forces lowering the tensile stress. If we analyze the film before drying a carbon content of 16.8% was detected, present in the form of octanethiol. However, after the heat treatment at 200 °C - which is above the boiling point of octane thiol - the layer cracks and completely detaches from the substrate, leaving flakes of CZTS thin film (Figure 8.6b). The carbon content of the film is now only 3.4%. Due to the evaporation of the octanethiol, the shielding on the NCs is removed, leading to high tensile stresses. Since the CCT is exceeded due to removal of the binder, the film cracks.

8.3.2 Deposition of Multilayers with Thiol Based CZTS Nanocrystals

The theory developed by Cima et al. [23] predicts that deposition of 25 nm NCs should result in a crack-free film up to 400 nm thick, since this is the CCT for hard

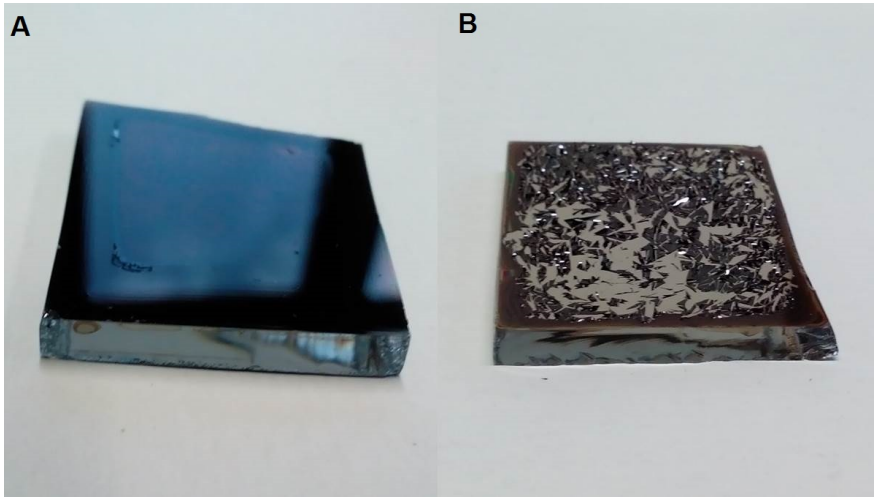

Figure 8.6: A: a single deposited thiol layer after heat treatment of 75 °C. B: The same thiol layer after a heat treatment of 200 °C in neutral atmosphere

spheres of that size touching each other. When we dry or thiol based film in first instance we are able to form a crack-free film when dried at 75 °C. The thiol reduces the interparticle interaction in the solvent depleted film (similar to the situation in Section 8.2), allowing a 1.5 μm thick film, this is shown in Figure 8.6a. But a heat treatment of 200 °C – which is the boiling point of OT – removes the majority of the OT and increases the interparticle interaction and the resulting the tensile stress and a complete cracking of the film temperatures rise above 200 degrees, this is shown in Figure 8.6b. Therefore we are obliged to reduce the deposited film thickness. Prosser et al. showed that for silica particles 25 nm films of 400 nm could be formed, to reach thicker films they used multilayer deposition. This was possible because the first layer acts as a new substrate after drying on which a second layer can be deposited [22]. This means that if the second layer would crack, the crack will not propagate through the first layer. This allows the deposition of a second layer upon our first layer (only if the first layer does not dissolve in the second layer). Transferring this knowledge on the thiol based system means that all thiols should be removed in the first layer – by means of a heat treatment – before subsequent deposition. Since it is possible to evaporate more then 80% of the thiols, after a heat treatment at 300 °C, the first layer will not redissolve. Similar is for the Si particles, depositing 300-400 nm thick layers results in film wich remain below the CCT, and thus are crack-free.

Due to the need of depositing a thin layer (400 nm) in a controlled way, we switch to inkjet printing instead of dropcasting. Here, up to 4 layers need to be

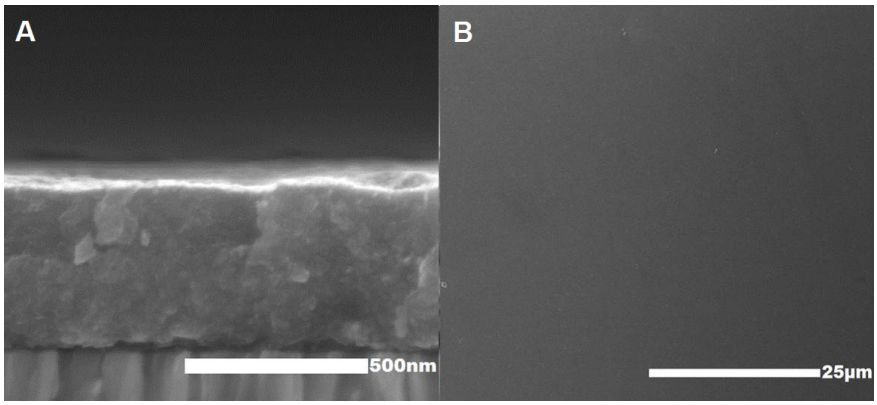

Figure 8.7: A: the crosssection of a multilayered thiol sample. B: the smooth surface of a layer based on thiol capped NCs

deposited (with intermediate heat treatments) with a layer thickness of 300-400 nm each. In between the depositions a 2-step heat treatment is applied with a 75 °C step to dry the solvent and a 300 °C to remove the bound OT. The result is a crack-free film visually identical to the film in Figure 8.6a, but could resist high temperatures (more then 200 °C). The fabricated layer was 1.2 μm thick and has a smooth surface as can be seen in Figure 8.7.

8.4 Deposition of Carbon-Free CZTS Nanocrystals

Within the logic of working with carbon-free ink stabilization, it would appear strange to add additional binders to increase the critical cracking thickness since these would reintroduce the carbon contaminants we aimed at excluding using this stabilization pathway. On the other hand, the clustering of sulfide stabilized CZTS NCs into larger aggregates as seen in Section 6.5.2 can be used to our advantage. Indeed, controlled flocculation and cluster formation can increase the layer thickness as was proven by Cima et al [23]. This generally has the possibility to increase the CCT of a layer by a maximum of 4 times the original CCT. Therefore, it still appears sensible to try depositing 1.5 μm thick layers using a single deposition step.

8.4.1 Results and Discussion

We first attempted to form CZTS layers by dropcasting, yet the DMSO which we used as the solvent did not wet the Mo substrates. When dried, this resulted in a film with a thickness of less then 1 μm at the edges and cracked in the center of the substrate where the layer was 3 μm thick (see Figure 8.8 on top). The

cracks clearly exposed the molybdenum back-contact, rendering the layer useless for further processing.

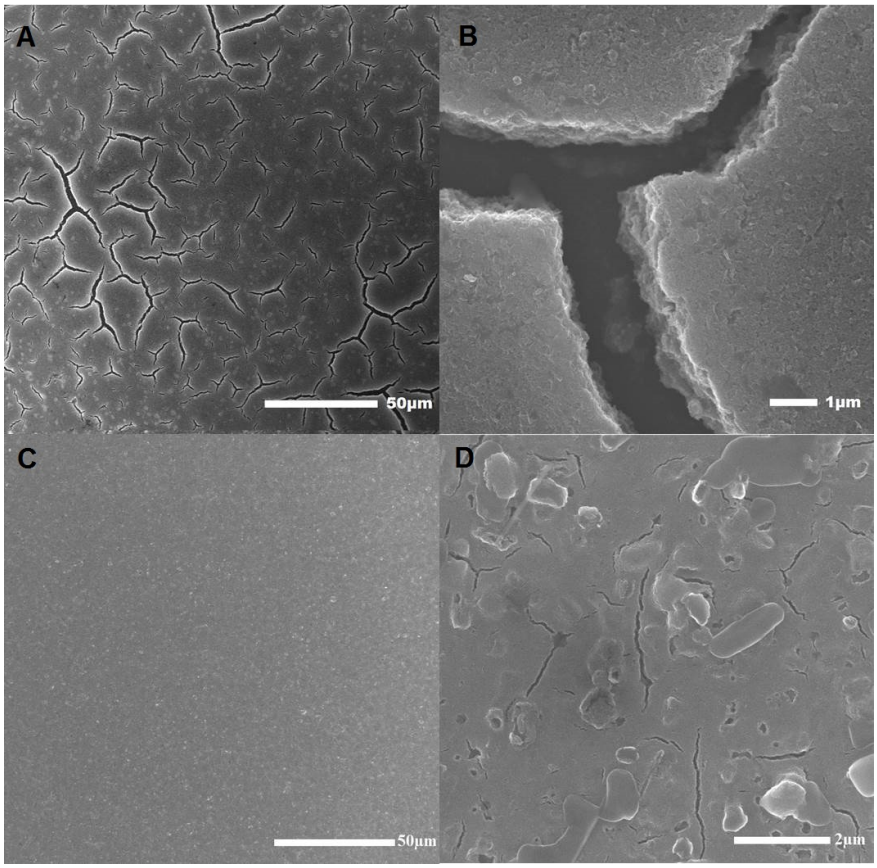

Figure 8.8: A: A picture of dropcast CZTS in DMSO which gave an irregular layer and cracks. B: the same layer at higher magnification, exposing the molybdenum back contact. C: A dropcasted and equally spread layer without mayor cracking. D: showing a magnified image of the layer in which only nanosized cracks appeared.

To circumvent this wetting problem, we turned to doctor blading in an attempt to force the ink to spread over the Mo surface. As we realized that heating would undo the spreading and thus lead to the similarly inhomogeneous films as obtained with dropcasting, we let the film dry slowly over 24 hours at room temperature. When dried under these conditions, homogenous films with a uniform layer thickness of $\approx$1.5 μm could be obtained. An example is shown in Figure 8.8 on the bottom. As can be seen, the layer does not contain large cracks that expose the substrate. Only when magnifying the image, one perceives superficial, nanosized cracks. Moreover, a heat treatment of the layer to remove all residual DMSO did

induce further cracking and the final C-content of the layer was as low as 0.35 w%.

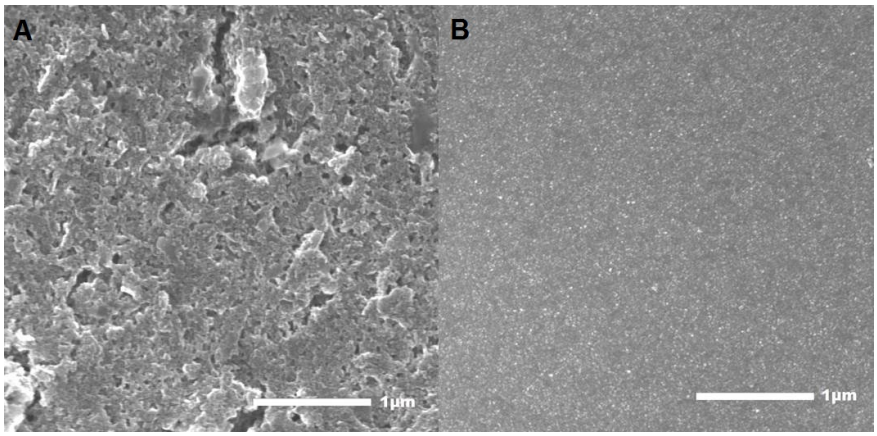

Figure 8.9: A: the magnified surface of layer fabricated using ammonium sulfide based CZTS ink. B: that of a layer based on OLA stabilized NCs

Magnified SEM images of the surface of layers formed with either CZTS/OLA or carbon-free CZTS are shown in Figure 8.9. It clearly follows that the carbon-free layer in Figure 8.9a is less smooth and much more porous then the layer on the CZTS/OLA layer in Figure 8.9b. We attribute this to the fact that the former layer is made by depositing CZTS clusters of up to 600 nm in size whereas the latter results from the deposition of individually dispersed CZTS NCs. Hence, although we succeeded in the deposition of a 1.5 μm crack-free thick layer using carbon-free CZTS NCs, we still have a layer which appears to be to porous. The effects of this porosity will have to be tested during an annealing step which will be explored in the next part of this thesis.

8.5 Depositing CTS+ZS Thin Films

To test the general view on crack-free film formation developed within this chapter, we extended our findings towards an additional, more complex precursor ink, consisting of the combination of CTS and ZS as CZTS precursors. This precursor combination has already been suggested in Section 5.4.

8.5.1 OLA-OA Based Stabilization

The ZS NCs are stabilized by oleate moieties. These are X-type ligands, which are typically tightly bound to the NC surface. The CTS NCs on the other hand are stabilized by OLA ligands. To prevent OLA desorption from the CTS NCs, we mix

the ZS and CTS NCs using an excess of OLA. After mixing, the NC suspension was purified to remove excess OLA and redispersed in dodecane forming a 5 w% ink to be used for further deposition studies. We can dropcast 1.5 μm crack-free thick films comparable to the results for CZTS NCs.

8.5.2 Thiol-OA Based Stabilization

We want to use thiols to prevent the OLA loss destabilization. We start from the ink used in Section 8.5, precipitate the ink and redisperse it in octanethiol. The NCs form a stable dispersion and can be used for ink jet printing. We deposit 4 layer of ≈400 nm to form a 1.5 μm thick film. The layer formed is crack-free.

8.5.3 C-Free CTS+ZS Inks

Our phase and ligand exchange in this ink is done separately for ZS and CTS NCs. CTS NCs are transferred in an identical way as the CZTS NCs described in Section 6.5.2. Forming a clustered NC ink in DMSO after phase transfer and purification. The ZS NCs transfer using a simple phase transfer with 2 phase system consisting of a dodecane + ZS NC system and a DMSO + ammonium sulfide ink. We mix the 2 DMSO based dispersions in a stoichiometric way and deposit a thin layer using doctor blading. We were able to fabricate a 1.5 μm thick crack-free but slightly porous layer. The difference between the layers of a sulfide or organic stabilized ink can be seen in Figure 8.10.

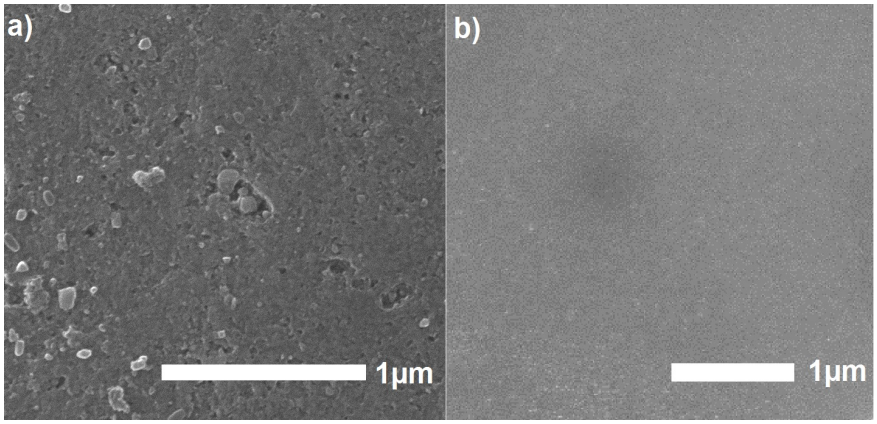

Figure 8.10: A: a top view of a slightly porous CTS + ZnS particle layer capped with sulfide anions. B: Top view of a CTS + ZnS particle layer capped with OLA and OA as a ligand.

8.6 Conclusions

We were able to deposit a film of 1.5 μm for CZTS NC inks with 3 different stabilizing agents.
The OLA based inks directly obtained form synthesis can easily produce a film with a single deposition, in which drying and heat treatment posed no problem. However, since the OLA forms a dynamic equilibrium with the solvent the ink must contain a large excess of OLA to be long term stable or it must be deposited quickly after a purification step (removing the excess OLA). Using the an ink with excess OLA causes small cracks and craters in the surface due to the removal of the large amount of OLA upon heat treatment, also the final layer contains nearly 20 wt% of carbon, which can be seen as an undesired contamination. When removing the excess of OLA, but leaving the NCs with at least 80% of its capping, crack-free single deposited layers can be formed. This is higher then the theoretical maximum of 400 nm for 25 nm particles due to the OLA that acts as a binder and can reduce the stress in the film. However, the final film still contains up to 7.5 wt% of carbon.
If octanethiol is used as a coordinating solvent a layer of 1.5 μm can be deposited in first instance. However when removing the thiol by heating above its boiling point a single deposited layer cracks and peels of the substrate. This can be solved with multilayer deposition of 300-400 nm thin films via inkjet printing. Intermediate removal of excess thiol, via heat treatment, is required to prevent redispersion in the next deposited layer. Crack-free layers of 1.5 μm can be produced.
The use of carbon-free stabilized inks removes all binder from the dispersion, but due to the nature of the exchange not NCs of 25 nm but clusters of NCs up to 600 nm are dispersed. But since no binder can be added the clusters can help us to deposit a layer of 1.5 μm in one deposition. When dried carefully a crack-free and carbon free layer can be deposited although the layer appears more porous, containing small voids compared to the C-stabilized based inks.
We also were able to apply our formulation and deposition methods towards the CTS + ZS NC system. Indicating that the gained knowledge on ink formulation and film deposition can be transferred to other particle systems.

References

[1] J. A. Lewis, "Colloidal Processing of Ceramics," *Journal of the American Ceramic Society*, vol. 83, no. 10, pp. 2341–2359, 2000.

[2] D. J. Shaw and B. Costello, "Introduction to colloid and surface chemistry: Butterworth-Heinemann, Oxford, 1991, ISBN 0 7506 1182 0, 306 pp,{\pounds} 14.95," 1993.

[3] R. J. Hunter and L. R. White, *Foundations of colloid science*. No. v. 1 in Oxford science publications, Clarendon Press, 1987.

[4] Malvern, "Zeta potential - An introduction in 30 minutes,"

[5] D. H. Napper, "Steric stabilization," *Journal of Colloid and Interface Science*, vol. 58, no. 2, pp. 390–407, 1977.

[6] M. L. H. Green, "A new approach to the formal classification of covalent compounds of the elements," *Journal of Organometallic Chemistry*, vol. 500, no. 12, pp. 127–148, 1995.

[7] B. Fritzinger, R. K. Capek, K. Lambert, J. C. Martins, and Z. Hens, "Utilizing self-exchange to address the binding of carboxylic acid ligands to cdse quantum dots," *Journal of the American Chemical Society*, vol. 132, no. 29, pp. 10195–10201, 2010.

[8] W. W. Yu, Y. A. Wang, and X. Peng, "Formation and stability of size-, shape-, and structure-controlled cdte nanocrystals: ligand effects on monomers and nanocrystals," *Chemistry of Materials*, vol. 15, no. 22, pp. 4300–4308, 2003.

[9] I. Moreels, Y. Justo, B. De Geyter, K. Haustraete, J. C. Martins, and Z. Hens, "Size-tunable, bright, and stable pbs quantum dots: a surface chemistry study," *Acs Nano*, vol. 5, no. 3, pp. 2004–2012, 2011.

[10] I. Moreels, B. Fritzinger, J. C. Martins, and Z. Hens, "Surface Chemistry of Colloidal PbSe Nanocrystals," *Journal of the American Chemical Society*, vol. 130, no. 45, pp. 15081–15086, 2008.

[11] A. Cros-Gagneux, F. Delpech, C. Nayral, A. Cornejo, Y. Coppel, and B. Chaudret, "Surface chemistry of inp quantum dots: a comprehensive study," *Journal of the American Chemical Society*, vol. 132, no. 51, pp. 18147–18157, 2010.

[12] I. Moreels, J. C. Martins, and Z. Hens, "Ligand adsorption/desorption on sterically stabilized inp colloidal nanocrystals: observation and thermodynamic analysis," *ChemPhysChem*, vol. 7, no. 5, pp. 1028–1031, 2006.

[13] N. C. Anderson, M. P. Hendricks, J. J. Choi, and J. S. Owen, "Ligand exchange and the stoichiometry of metal chalcogenide nanocrystals: Spectroscopic observation of facile metal-carboxylate displacement and binding," *Journal of the American Chemical Society*, vol. 135, no. 49, pp. 18536–18548, 2013.

[14] Z. Hens and J. C. Martins, "A solution nmr toolbox for characterizing the surface chemistry of colloidal nanocrystals," *Chemistry of Materials*, vol. 25, no. 8, pp. 1211–1221, 2013.

[15] A. Hassinen, I. Moreels, K. De Nolf, P. F. Smet, J. C. Martins, and Z. Hens, "Short-chain alcohols strip x-type ligands and quench the luminescence of pbse and cdse quantum dots, acetonitrile does not," *Journal of the American Chemical Society*, vol. 134, no. 51, pp. 20705–20712, 2012.

[16] R. Dierick, F. den Broeck, K. De Nolf, Q. Zhao, A. Vantomme, J. C. Martins, and Z. Hens, "Surface Chemistry of CuInS2 Colloidal Nanocrystals, Tight Binding of L-Type Ligands," *Chemistry of Materials*, vol. 26, no. 20, pp. 5950–5957, 2014.

[17] R. Gomes, A. Hassinen, A. Szczygiel, Q. Zhao, A. Vantomme, J. C. Martins, and Z. Hens, "Binding of Phosphonic Acids to CdSe Quantum Dots: A Solution NMR Study," *J. Phys. Chem. Lett.*, vol. 2, pp. 145–152, 2011.

[18] N. C. Anderson, M. P. Hendricks, J. J. Choi, and J. S. Owen, "Ligand Exchange and the Stoichiometry of Metal Chalcogenide Nanocrystals: Spectroscopic Observation of Facile Metal-Carboxylate Displacement and Binding," *Journal of the American Chemical Society*, vol. 135, no. 49, pp. 18536–18548, 2013.

[19] S. Hohng and T. Ha, "Near-complete suppression of quantum dot blinking in ambient conditions," *Journal of the American Chemical Society*, vol. 126, no. 5, pp. 1324–1325, 2004.

[20] M. V. Kovalenko, M. Scheele, and D. V. Talapin, "Colloidal nanocrystals with molecular metal chalcogenide surface ligands," *Science*, vol. 324, no. 5933, pp. 1417–1420, 2009.

[21] A. Nag, M. V. Kovalenko, J. S. Lee, W. Y. Liu, B. Spokoyny, and D. V. Talapin, "Metal-free Inorganic Ligands for Colloidal Nanocrystals: S(2-), HS(-), Se(2-), HSe(-), Te(2-), HTe(-), TeS(3)(2-), OH(-), and NH(2)(-) as Surface Ligands," *Journal of the American Chemical Society*, vol. 133, no. 27, pp. 10612–10620, 2011.

[22] J. H. Prosser, T. Brugarolas, S. Lee, A. J. Nolte, and D. Lee, "Avoiding Cracks in Nanoparticle Films," *Nano Letters*, vol. 12, no. 10, pp. 5287–5291, 2012.

[23] R. C. Chiu, T. J. Garino, and M. J. Cima, "Drying of Granular Ceramic Films: I, Effect of Processing Variables on Cracking Behavior," *Journal of the American Ceramic Society*, vol. 76, no. 9, pp. 2257–2264, 1993.

[24] K. B. Singh and M. S. Tirumkudulu, "Cracking in Drying Colloidal Films," *Phys. Rev. Lett.*, vol. 98, no. 21, p. 218302, 2007.

[25] E. Santanach Carreras, F. Chabert, D. E. Dunstan, and G. V. Franks, "Avoiding mud cracks during drying of thin films from aqueous colloidal suspensions," *Journal of colloid and interface science*, vol. 313, no. 1, pp. 160–168, 2007.

Part III

Phase Transformation in CZTS(e) Nanocrystal Films

Efficient thin film solar cells require a complete separation of the electron-hole pairs photo generated in the CZTS(e) absorber layer [1]. In as-deposited NC film, various factors may hamper charge-carrier separation. First, charge transport relies on hopping between adjacent nanocrystals, a mechanism leading to relatively low carrier mobilities. Second, the large surface area of the nanocrystals may lead to extensive trapping and recombination of charge carriers. [2] A possible way to overcome these problems is the transformation of the nanocrystal films into a dense, solid film, for example by thermal annealing. The main goal of this process would be the reduction of the grain boundaries. Current progress in CZTS(e) solar cells shows that nanocrystal based solar cells without additional grain-growing thermal annealing are unable to reach 1% efficiency [3]. Therefore, this chapter focuses on different approaches to make the as-deposited nanocrystal film more dense, thus increasing the grain size and reducing the surface area of the grain boundaries.

At present, no systematic research on the densification of nanocrystal films has been conducted and little is known about the mechanism behind the phenomena [4]. We lack initial knowledge on densification mechanisms in nanocrystal films and therefore we started with an experimental study on the relation between heating/sulfurization/selenization parameters and properties of the resulting films. This study was inspired by research on densification of CIGS NC films, first published in 1997 [5], in which the optimal conditions for densification were described. Here particles were synthesized using a precipitation reaction and films were spray deposited on a Mo substrate. We accordingly followed three different directions: (1) employing (rapid) thermal annealing of the NC precursor films; (2) incorporation of excess Se or S through annealing in a sulphur or selenium rich atmosphere and (3) utilize a binary/ternary composite structure, from which the desired component is formed. In this part of the thesis we will explore these 3 conditions for CZTS(e) NC thin films.

9

Annealing of Sulfide Stabilized Colloidal Semiconductor Nanocrystals

9.1 Introduction

Since thermal annealing is indispensable to induce recrystallization in a NC film, we first explore what happens with NC layers when heated in an atmosphere not containing sulphide or selenide species. As shown in part 2, crack-free layers could be formed by depositing NCs from inks either stabilized by steric hindrance (ligands) or charge (carbon-free inorganic anions). The long chained organic ligands leave residual carbon in the layer after deposition and drying, which can hamper the possible phase transformation or lead to possible carbon deposits that may deteriorate the electronic properties of the layer [6]. To circumvent this problem, we introduced colloidal NCs stabilized with short anions, possibly involving chalcogenide such as S^{2-} of Se^{2-}), as an alternative. Especially chalcogenide-based anions are of interest since they occupy a smaller volume than organic ligands and they should not introduce a residual contamination with elements foreign to the final semiconductor compound. This could be an improvement not only for CZTS(e), but also for CIGS. NC stabilization with chalcogenide ligands would have the additional advantage of creating a small excess of chalcogenide species in a NC layer prior to annealing. This could possibly be exploited to avoid the cumbersome gas-phase sulfurization or selenization step typically required for grain growth and thus device integration in a highly efficient CIGS or CZTS(e) solar cell. However, the annealing and sintering behavior of chalcogenide stabilized NC

layers has not been studied yet.

In this chapter, we therefore explore the effect of different thermal treatments on thin films of CZTSe NCs stabilized with $(NH_4)_2S$ without the use of a chalcogenide atmosphere. We will test the difference between an inert and a reducing atmosphere, where we hope that the stabilization by S^{2-} can remove as much contaminants as possible and enhance recrystallization. We will use in-situ transmission electron microscopy (TEM) and in situ X-ray diffraction (XRD) to follow the behavior of the NCs during heat treatment. In addition, thermogravimetric analysis (TGA) combined with mass spectrometry (MS) and X-ray photoelectron spectroscopy (XPS) will be used to analyse the annealing-induced changes in film composition. Part of this work was executed in collaboration with Ruben Dierick (Ghent University, synthesis of CIS nanocrystals and analysis of TGA and XRD measurements), Dr. Els Bruneel (Ghent University, XPS measurements), Boris Cappon and prof. Christophe Detavernier (Ghent University, in-situ XRD measurements) and Hanne Damme and Prof. An Hardy (Hasselt University, TGA-MS measurements).

9.2 Experimental

9.2.1 Synthesis of Nanocrystals

The synthesis of CdSe and CZTSe NCs are described respectively in Chapter 3 and 4 of this thesis. The synthesis of CIS NCs are based on the synthesis of Panthani et al. [7].

9.2.2 Processing of Nanocrystals

The processing and formation of thin films of CZTSe nanocrystals has been performed as described in Part 2 of this thesis for CZTS. Also CIGS and CdSe thin films of NCs with steric stabilizers and sulfide based stabilization has been fabricated according to the same principle.

9.2.3 Thermal Treatment

Thermal treatment was preformed in a tube furnace at a temperature of 450 °C. We used a gas flow of N_2 atmosphere with a reducing atmosphere of Ar + 5% H_2 (forming gas).
For in situ XRD, He + 5% H_2 forming gas was used.

9.2.4 Characterization

To determine the effect of heating in a vacuum, we used bright-field TEM images recorded with a JEM-2200FS transmission electron microscope. These samples were prepared by dipping a TEM-grid in a dilute NC solution. XRD and in-situ XRD patterns were recorded using a Bruker D8 Discover. Cu K alpha radiation was used as an X-ray source, while a linear Vantec detector monitored the crystallinity of the thin films. XPS analysis was performed using a S-probe spectrometer with an Al-source (monochromatized Al-radiation: 1486 eV).

9.3 Results and discussion

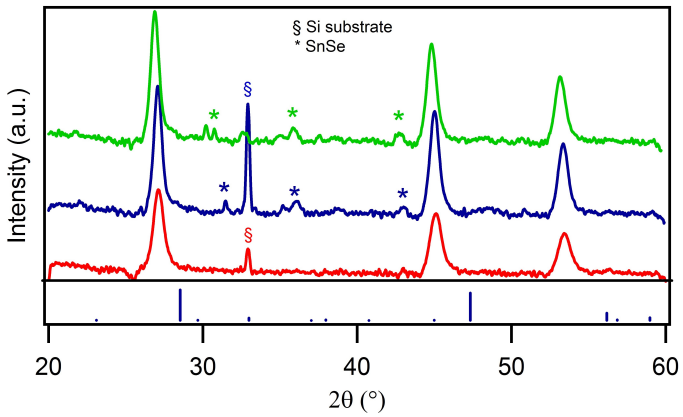

Figure 9.1: XRD reflection of CZTSe NCs covered with OLA (red) the same CZTSe NCs after annealing in reducing atmosphere (blue) and in neutral atmosphere (green) at a temperature of 450 °C

Annealing a 1 μm thin film of OLA-stabilized CZTSe NCs (capped with OLA) to 450 °C at a rate of 10°C/min in a N_2 atmosphere results in sharpening of the CZTSe reflections as shown in the XRD diffractogram in Figure 9.1 (green curve). According to the Scherrer equation, this sharpening of the diffraction peaks reflects crystal growth during the heat treatment, where we calculate an increase of the crystallite size from 11 nm for as-deposited CZTSe NCs to 18 nm after annealing. When performing the same experiment in a N_2 + 5% H_2 atmosphere the NCs attain a diameter of 17.8 nm, i.e., no difference is detected. For both these treatments, the XRD diffractogram indicate that annealed CZTSe NC layers contain a small fraction of a secondary phase, which we identified as SnSe. So, the different treatments lead to similar results.

In the case of films of CZTSe NCs capped with sulfide anions, Figure 9.2

shows the evolution of the signal intensity in the 2θ region around the CZTSe (112) peak as a function of time during a thermal treatment in helium following the temperature profile indicated in Figure 9.2. Most notably, no significant peak sharpening is observed. Estimating the grain size from the width of the diffraction peaks points to an increase of from 11.2 nm to 12.9 nm after annealing only. Hence, sintering of S^{2-} stabilized CZTSe NCs seems inhibited as compared to long chain organic ligands (see Figure 9.1). On the other hand, we found that the sintering of CZTSe NCs with S^{2-} ligands can be triggered by exposing the NCs to forming gas during annealing (5% H_2 in He). In this case (Figure 9.2b), the (112) peak sharpens throughout the process. This indicates growth of the CZTS NCs, where a detailed calculation yields a final crystallite size of 16.5 nm. For comparison, XRD patterns are shown after the annealing in helium (Figure 9.2e) and forming gas (Figure 9.2f). Note that for the annealing under forming gas, also some SnSe is formed.

To assess the generality of these findings, the same annealing experiments were conducted with different metal chalcogenide NCs stabilized using S^{2-} anions. We found that $CuInS_2$ (CIS) and CdSe [8] exhibit a similar inhibition of sintering. As an example, Figure 9.3 shows the in-situ XRD diffractogram of CIS NCs, which exhibits a small but significant improvement of the nanocrystallinity of the NC film. For CdSe the exact same crystal growth is observed. Although there is a significant sharpening of the XRD peak we still are limited to a nanocrystalline structure.

To further confirm the difference in annealing behavior between OLA capped and S^{2-} stabilized NCs, we focused on $CuInS_2$ NCs and compared their behavior using in situ TEM. A similar study on CZTSe NCs proved impossible since we found that these NCs lose SnSe when heated in the vacuum environment of the TEM. Dip coated sub-monolayers of CIS NCs with different surface termination were heated to 550 °C on the TEM grid and their morphology was continuously monitored. Typical TEM micrographs at elevated temperature are shown in Figure 9.4.

When the temperature is in the range of 450-500 °C clear sintering is observed for CIS NCs capped with oleylamine (Figure 9.4a and b), where even large crystallites with dimensions of 100 nm appear. This behavior is absent when heating S^{2-} stabilized CIS NCs (Figure 9.4c and d). In this case, the CIS NCs size and shape is preserved throughout the heating process. While it is difficult to set an exact temperature during in situ TEM studies, the difference between both samples is obvious and concurs with the observations from the in situ XRD measurement in Figure 9.2a.
In order to identify the species leaving the nanocrystal-ligand system upon annealing, TGA-MS measurements were carried out on a powder of CIS NCs capped

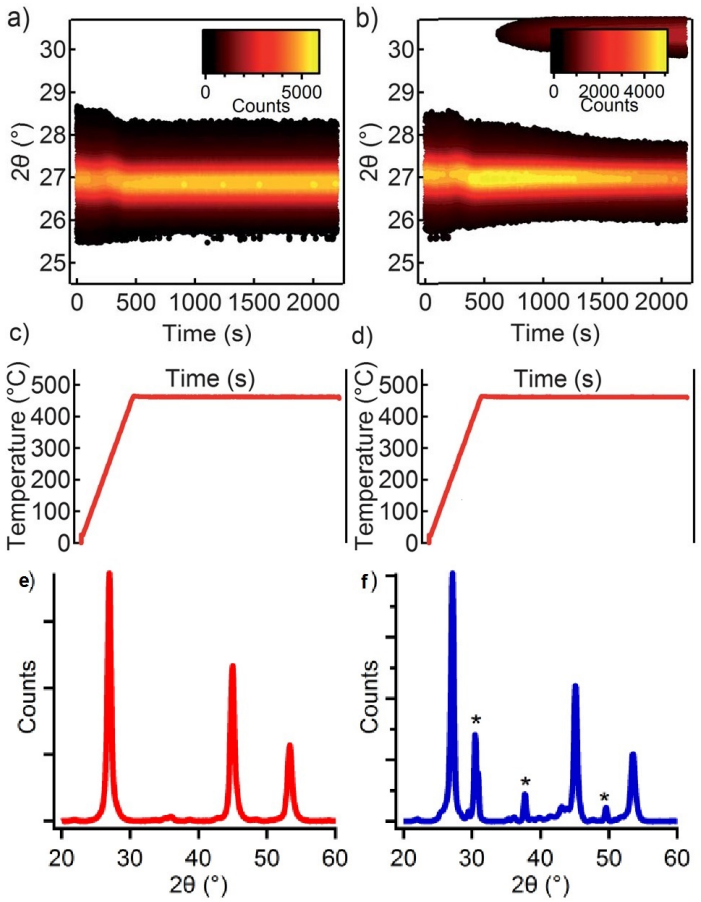

Figure 9.2: In situ XRD experiments on CZTSe NCs capped with sulfide ligands.(a) (112) reflection after treatment with neutral atmosphere (b) With reducing atmosphere (c) and (d) the temperature profile over time and (e) the XRD reflections after annealing of NC in neutral atmosphere and (f) in forming gas

with $(NH_4)_2S$ in both inert and reducing atmosphere. Figure 9.5a shows the TGA-DTG signal when both samples were heated to 600 C at 10 C min^{-1}. In TGA, we observe an overall similar, stepwise weight loss up to a temperature of 600 °C amounting to ≈30% of the original mass. Nevertheless, the DTG signal shows a clear difference between both samples in the temperature range 400-600 °C, where the sample annealed in an inert atmosphere loses extra mass. The DTG signal also emphasizes the stepwise decomposition process. Using mass spectrometry coupled in-line with TGA, gaseous species evolving from both samples were detected in situ. As summarized in Table 9.1 , this involves species which we

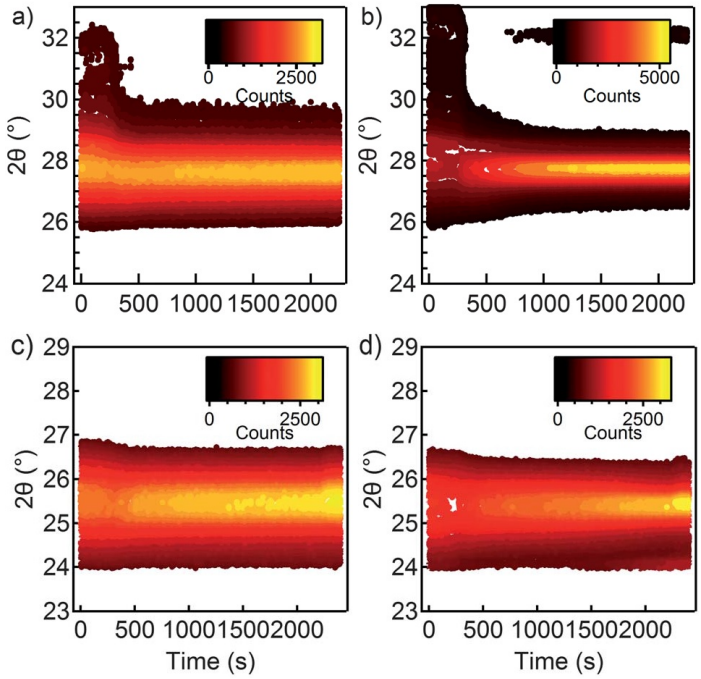

*Figure 9.3: In situ XRD experiments from the annealing of CIS capped with sulfide anion in neutral atmosphere (a) and in forming gas (b). The same experiment for CdSe in neutral atmosphere (c) and forming gas (d) (the * represents a secondary phase of SnSe).*

suspect to originate from both $(NH_4)_2S$ and formamide. While the powder used for the TGA-MS measurements appeared to be dry, fragments originating from the decomposition of the solvent used, i.e., formamide, can clearly be distinguished. The response for all the fragments in Table 9.1 is shown as a function of temperature in Figure 9.5b-e. At 100 °C, the largest mass loss originates from HCN/CN and CO_2 fragments, and this is similar for both annealing conditions. We identify species with m/z values of 16, 17 and 18 as NH_2^+, NH_3^+ NH_4^+ species, originating from either $(NH_4)_2S$ or formamide. Under a H_2/N_2 atmosphere, the corresponding signals (Figure 9.5b) show an increase at high temperatures, which we attribute to the formation of H_2O – which leads to fragments with the same m/z – by the reaction between H_2 and residual O_2, an interpretation corroborated by the reduction of the residual O_2 signal at m/z = 32 (data not shown).

Next, at 250 °C, another set of CO_2 fragments is released, followed by the release of SO_2. Importantly, fragments with m/z ratios of 33 and 34, corresponding to SH^+ and SH_2^+, respectively, are detected from 300 °C onwards in the case of a reducing atmosphere, and are absent under inert conditions. These fragments

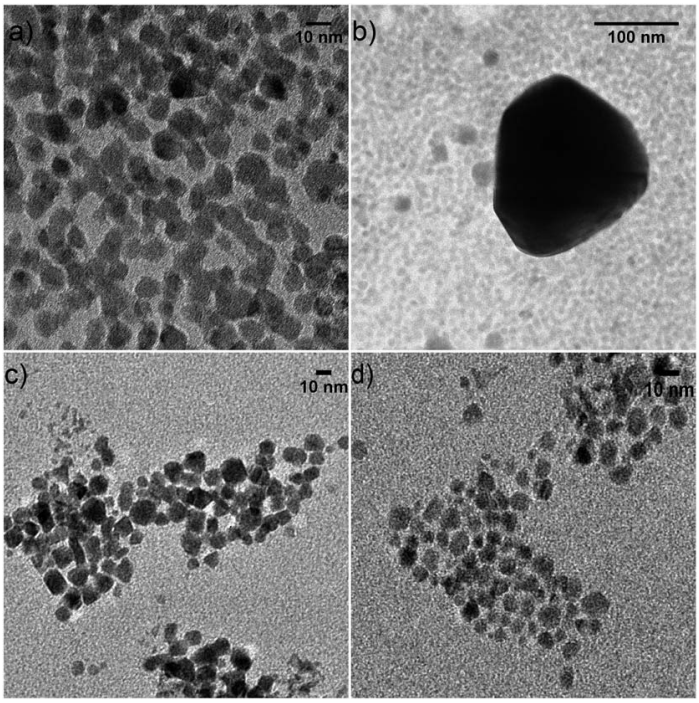

Figure 9.4: In situ TEM images of CIS NCs. The NCs were heated to 450° C in high vacuum. (a) and (b) are pictures of OLA capped CIS NCs. (c) and (d) are pictures of sulfide base NCs.

are typical of H_2S, indicating its formation only in the case of H_2/Ar and their appearance coincides with the onset of sintering in the CIS NC film. Interestingly, CO_2 and SO_2 are detected in both conditions. We attribute CO_2 to the decomposition of formamide, and we suspect that this coincides with the oxidation of S_2 from $(NH_4)_2S$ – the species stabilizing the NCs in formamide – to SO_2 (cf. infra). In Figure 9.5d, we can also observe the species responsible for the difference in DTG signals (Figure 9.5e). At 500 °C, compared to annealing in a reducing atmosphere, an excess amount of CO_2 and SO_2 leaves the sample. Since we base our annealing results in in situ XRD on thermal treatments that do not exceed 450 °C, it appears that the presence of this species is related to the inhibition of the sintering of NCs. In the case of a hydrogen containing atmosphere, this oxidized compound can be reduced to H_2S, leaving the surface.

To confirm the presence of oxidized sulfur in NC films originally stabilized by $(NH_4)_2S$, we analyzed various films using XPS. Figure 9.6a shows an XPS spectrum recorded on a layer of as-deposited NCs stabilized by $(NH_4)_2S$. The spectrum shows a single peak related to S at 161 eV, which is typically attributed

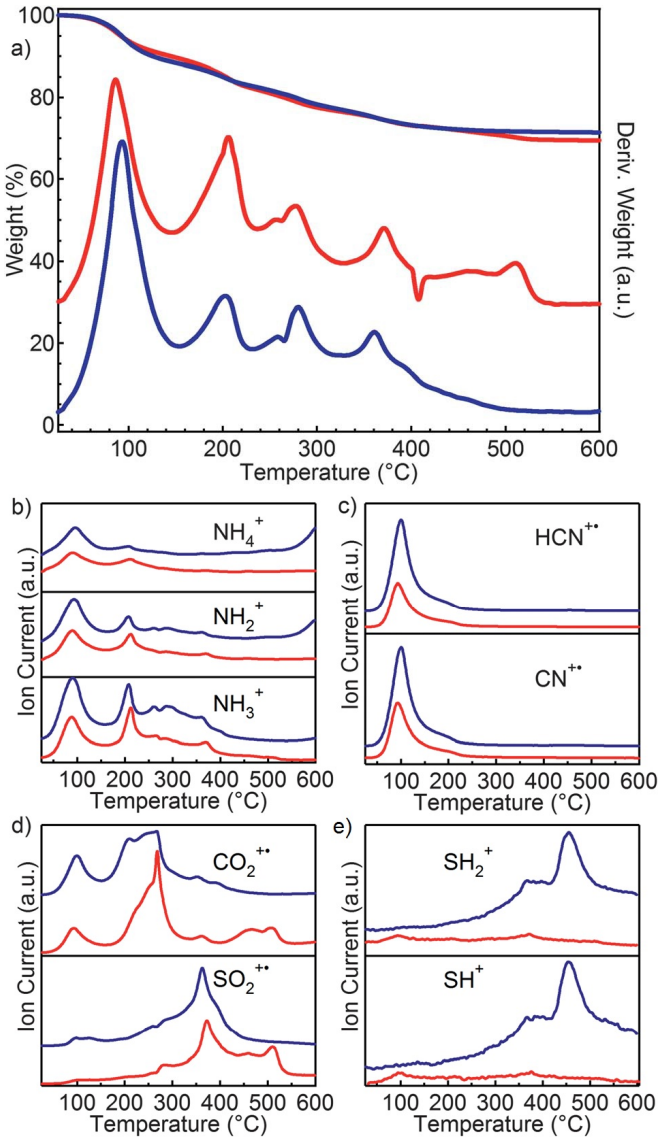

Figure 9.5: a: TGA-DTG spectra of CIS-$(NH_4)_2S$ NCs in (blue) Ar/H_2 (5% H_2) and (red) He. b-e: Detected signals in mass spectrometry as a function of temperature during the TGA-MS experiment. Red and blue lines represent signals for samples heated in inert respectively reducing atmosphere.

to a relatively weak bonding 2p state of S^{2-}. We stress that no oxidized sulfur species are found prior to annealing, which is in any case carried out as soon as

m/z	Species	Proposed source
16	NH_2^+	$(NH_4)_2S$/$HCONH_2$
17	NH_3^+	$(NH_4)_2S$/$HCONH_2$
18	NH_4^+	$(NH_4)_2S$/$HCONH_2$
26	CN^+	$HCONH_2$
27	HCN^+	$HCONH_2$
33	SH^+	$(NH_4)_2S$
34	SH_2^+	$(NH_4)_2S$
44	CO_2^+	$HCONH_2$
64	SO_2^+	$(NH_4)_2S$

Table 9.1: List of m/z values detected in TGA-MS

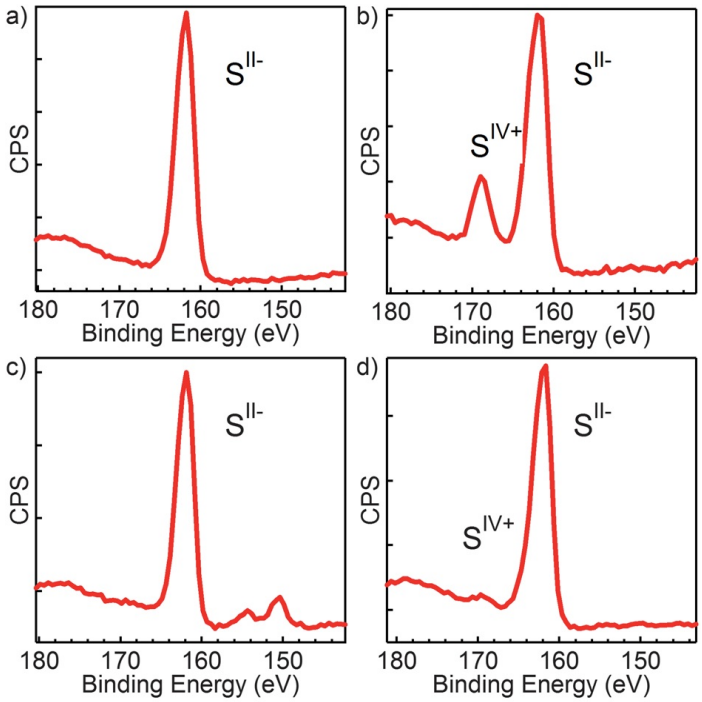

Figure 9.6: XPS spectra of $CuInS_2$ layers capped by $(NH_4)_2S$ on Si: As-deposited (a), after 3 weeks under ambient conditions (b), after following the standard thermal treatment in H_2/N_2 (c) and after heating to 300 °C in N_2 (d).

possible after deposition. After keeping this layer under ambient conditions for 3 weeks, a second feature emerges at higher binding energy (Figure 9.6b), which can be related to S species in a higher oxidation state (i.e., S^{4+} or higher). We thus conclude that all sulfur in the system is initially present as S^{2-} and $(NH_4)_2S$,

while the sulfide at the NC surface progressively oxidizes to SO_2, ${SO_3}^{2-}$ and/or ${SO_4}^{2-}$. Since we found that NC sintering is inhibited under an inert atmosphere for layers composed of solely S^{2-} as well, we measured an XPS spectrum of these fresh layers after annealing in H_2/Ar (Figure 9.6c) and N_2 (Figure 9.6d). Only in the latter case, a slight contribution of oxidized sulfur is discernible. This shows that the oxidation of sulfide species occurs during annealing under inert conditions, probably related to the decomposition of the leftover solvent.

9.4 Conclusions

In summary, we studied the behavior of films of CZTS NCs stabilized by S^{2-} ligands under thermal annealing. Whereas under inert conditions, the NCs show little sintering at temperatures up to 450 °C, more pronounced growth is observed for annealing in a reducing atmosphere. A similar difference as a function of surface termination is found for CdSe and CIS NCs. We attribute the difference between both to the behavior of the S^{2-} species. Under a reducing atmosphere, the onset of sintering concurs with the release of H_2S, while under an inert atmosphere, sulfide is retained in the film and partially oxidized, thereby inhibiting sintering. Importantly, the oxidized sulfur compounds can originate either from exposure to air or from the decomposition of solvent molecules during the annealing process itself.

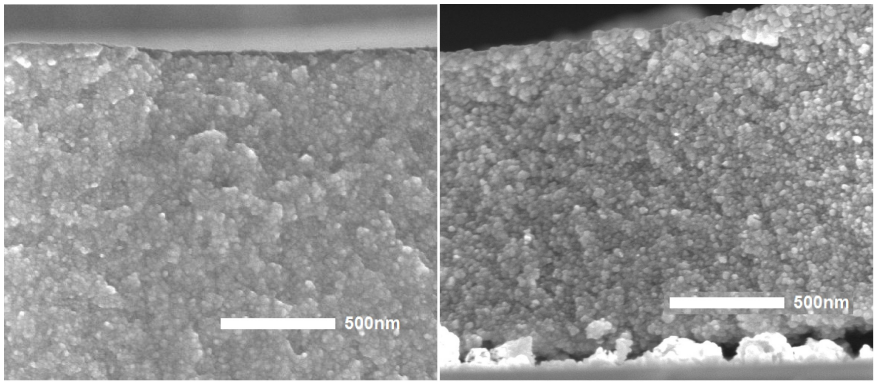

Figure 9.7: Cross sectional SEM of CZTSe NC capped with sulfide anions annealed in neutral atmosphere (a) and forming gas (b).

Even if sintering of CZTS NCs with S^{2-} ligands can be induced by using a reducing atmosphere, the overall grain growth remains limited. This is clearly demonstrated by a cross sectional SEM image of a layer of CZTSe NCs (see Figure 9.7), where for both annealing conditions (inert atmosphere in Figure 9.7a and reducing atmosphere in Figure 9.7b) the nanocrystalline structure of the film is largely preserved. Hence, whereas the NC stabilization by $(NH_4)_2S$ moieties pro-

vides a way to stabilize CZTSe NCs in polar solvents while decreasing the carbon content and the inter-NC distance in a NC thin film to a minimum, this lack of sintering is a considerable drawback for applications such as thin film photovoltaics that require dense thin films made from large crystallites.

10

Chalcogenide Induced Crystal Growth in CZTS Nanocrystals Films

10.1 Introduction

We have shown that an annealing treatment under an inert or reducing atmosphere, only a minor NC recrystallization and grain growth to micro-sized crystals is clearly absent. However, an introduction of excess chalcogenide in the layer can improve crystal growth [9]. This excess can be created by the introduction of the NC film in a sulfur or selenium rich atmosphere during heat treatment, also known as sulfurization or selenization respectively. This technique originates from the formation of CIGS absorber layers in which metal containing films were deposited and where the chalcogenide had to be introduced via the atmosphere [10]. Although the as-deposited NCs already contain the desired amount of S or Se, literature has shown that selenization can replace up to 90% of S by Se in the case of CZTS NCs [11]. This replacement of S by Se in the NCs could be a driving force inducing grain growth and densification of the NC layer and will be explored here from that point of view, where both sulfurization and selenization are considered.

Generally, bilayer structures are produced after selenization of the NC film. Here, a large-grained layer can be found on the surface, while a fine-grained layer is present at the interface with the Mo substrate, illustrated in Figure 10.1. In some cases, an additional large grain layer is formed at the interface, leading to a trilayer structure (figure 10.1b). Hence, a recrystallization process commences at places with the highest interfacial energy and lowest thermal activation energy. These

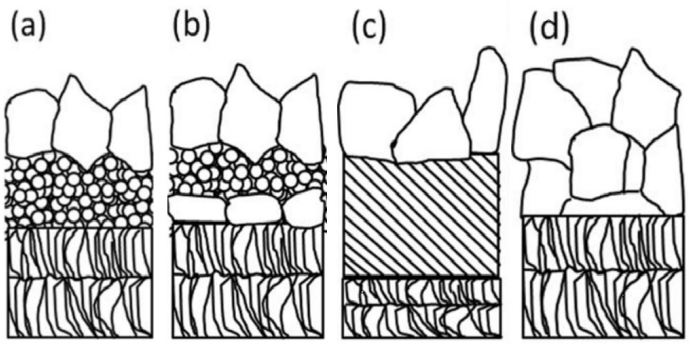

Figure 10.1: A graphical representation of how CZTS NCs can transform. A and B: are general transformation of a NC precursor containing organics. C: molecular precursors after transformation using organics. D: transformation of organic free molecular precursors [1].

places are equal to the surface of the film, and in some cases to the Mo interface, producing grains with a diameter of 1 or more microns. So, grain growth of the NCs far from the interface proceeds much slower. These types of films (Figure 10.1a and b) generally produces device efficiencies in the range of 7-10% [11, 12]. This typical morphology of the annealed NC films is thought to be caused by the presence of carbon due to the NC ligands. Ink-based CIGS solar cells show a similar morphology, when a significant amount of carbon is present to improve viscosity and coating behavior of the precursor (Figure 10.1c) [13, 14]. Also here CIGS grains only nucleate at the surface. Carbon-free molecular precursor based CZTS films on the other hand (Figure 10.1d) show stacked grains, indicating that the nucleation takes place throughout the bulk of the film. This could be seen in the work of Mitzi et al. using a C-free hydrazine based precursor layer [15].

The different layered structures of the annealed NC films have different effects on the performance of the resulting devices. Large CZTS grains arranged in a single monolayer contain almost no grain boundaries, which have a beneficial effect on the preformance. Few interfaces lower the series resistance and reduce the recombination of excitons. However, if fine grain layers are present (e.g. nanocrystals), the series resistance will increase, leading to the inactivity of the fine grain layer during current generation. Hence, the presence of fine grain layers should be avoided to improve the device performance. The crystal interfaces are also detrimental for the exciton hole pair recombination.
A higher degree of crystallinity could be achieved using a higher Se supply by increasing the amount of Se evaporation and the generation of higher Se pressures. However, the formation of a thicker $MoSe_2$ layer in-between CIGS and Mo is a

drawback, which was explained by a liquid Se assisted reaction rather than by a vapor phase Se assisted reaction [4].
In this Chapter we will explore the effect of sulfurization and selenization on CZTS nanocrystalline films deposited with different stabilizers. We will start with CZTS NCs capped with organics steric stabilizers, to study the effect of carbon in the layer. The sulfurization/selenization of a carbon-free layer was studied as well. Here we aimed at obtaining a similar result as the carbon-free precursor films in Figure 10.1d. Sulfurization, device fabrication and efficiency testing was done in collaboration with Prof. P. Dale of the University of Luxembourg.

10.2 Experimental

10.2.1 Synthesis

The synthesis of CZTS NCs has been discussed in Part 1 of this thesis.

10.2.2 Nanocrystal Processing

The processing of NCs was discussed in part 2 of this thesis. Crack-free layers of NCs stabilized by OLA, thiol and sulfide were used in the densification experiments. We started from crack-free layers deposited on molybdenum coated glass with a thickness of 1.5 μm of CZTS NCs. The layers were dried and preheated in neutral atmosphere to 300 °C to remove all solvent.

10.2.3 Sulfurization

Sulfurization was performed in a graphite box that was placed in a tube furnace. The tube furnace was flushed and placed under a pressure of 1 mbar in a N_2 + 5% H_2 atmosphere. In the graphite box, a square inch sized molybdenum coated lime glass sample with a layer of CZTS NCs was placed together with 100 mg of elementary S and 20 mg of tin sulfide [16]. The sulfur evaporates at high temperature providing a sulfur atmosphere. The tin sulfide is added to provide a counter pressure of SnS which otherwise would become volatile and escape from the CZTS layer [17]. After the annealing process the sample was characterized using cross sectional SEM, XRD and Raman spectroscopy to determine the phase morphology and crystal structure.

10.2.4 Selenization

For selenization we designed a graphite box which could be sealed. In the graphite box an inch by inch substrate with the CZTS NC layer was deposited, together with 79 mg of Se. The box was sealed under N_2 atmosphere at 25 °C and atmospheric

pressure. The closed box was placed in a muffle furnace that was heated to 550 °C for 30 minutes. Additional $SnS(e)_2$ to prevent Sn loss is not necessary, as the box can be sealed and no $SnS(e)_2$ can escape.

10.2.5 Characterization

SEM was performed using a JEOL JSM-7600f and cross sections were measured without metal coating. EDX measurements were executed using an Oxford Instruments Silicon Drift Detector (SDD) - X-Max^N detector. XRD measurements were performed using a Thermo Scientific ARL XTRA Powder Diffractometer and a Cu K alpha radiation was used as an X-ray source. Raman measurements were performed using a RAMANRXN[1] microprobe spectrometer using a green laser with a wavelength of 532 nm.

10.3 Results

10.3.1 Sulfurization of Steric Stabilized CZTS Nanocrystal Films

In a first experiment, a crack free film of OLA stabilized CZTS NCs was annealed using a sulfur rich atmosphere. We annealed at 550 °C during 30 minutes. Images of the obtained film are shown in Figure 10.2. The layer shows a bilayer structure (Figure 10.2 a) featuring a coarse grained crystalline layer on top of a fine grained layer. The top view of the layer (Figure 10.2b) shows the size of the formed crystals. The XRD diffractogram (Figure 10.2c) show the possible reflections of kesterite CZTS, the reflections of Mo and a small amount of MoS_2. If the kesterite reflections are examined more closely, a broad base and sharp top on the reflections is noticeable. The broad base originates from the small granular crystals, which induce a broader reflection. The SEM picture shows that these crystals have a diameter of maximum 15-40 nm, in other words similar to the original NCs. The top layer consists of crystals with a diameter up to 500 nm, which lead to the narrow contribution to the XRD reflections. Importantly, Raman spectroscopy showed the sharp characteristic peak of kesterite ad 336 cm^{-1} [18], confirming that indeed kesterite CZTS was formed.

The composition of both layers (coarse and fine grained) and the initial as-deposited film was obtained by means of SEM-EDX. The respective atomic fractions are summarized in Table 10.1. It follows that the coarse grained layer has the stoichiometric CZTS composition and is completely free of carbon, although we started from zinc-rich and copper-poor NCs stabilized by OLA ligands. This indicates that additional Cu, Sn and S is incorporated in the top film. Whereas the additional Sn and S can be taken from the atmosphere, a phenomenon also reported by Berg et al. if SnS_2 is present in the atmosphere [16], the Cu cannot. Looking at the composition of the bottom layer, one notices that it still has the

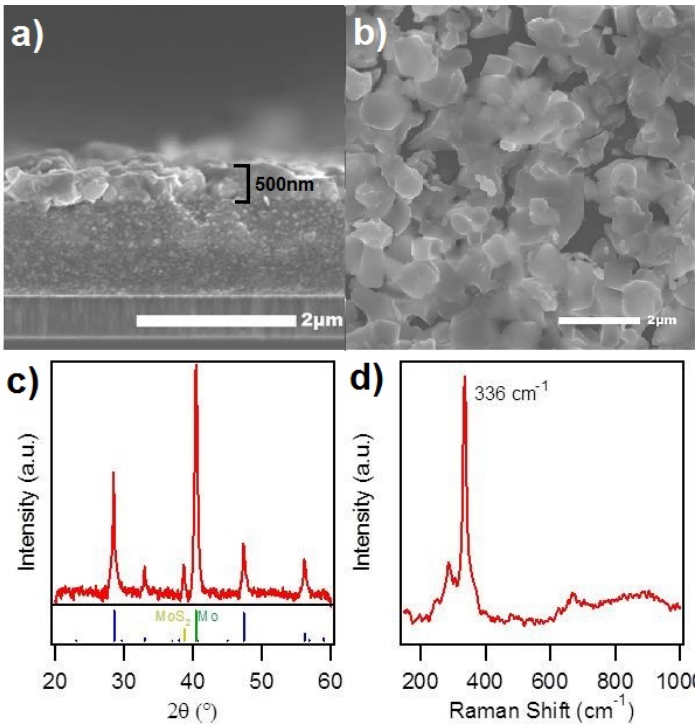

Figure 10.2: A sulfurized layer of OLA capped CZTS NCs . (a) A cross-sectional image of the layer indicating a 500 nm microcrystalline toplayer and a nanocrystalline bottom layer . (b) Top view of the layer. (c) XRD reflections of the layer. (d) Raman spectrum of the layer.

same Zn-Sn ratio and a similar amount of carbon as compared to the as-deposited layer, while featuring a huge Cu deficit. Hence, the formation of the characteristic double layer seems related to (1) the mobility of Cu atoms in the bottom layer and (2) the removal of carbon and incorporation of extra Sn and S in the top layer where the resulting stoichiometric CZTS top layer inhibits further transformation. On the other hand, the formation of MoS_2 – as can be seen in the XRD reflections in Figure 10.2 – indicates that sulfur can penetrate the entire layer without however inducing further changes in the fine grained bottom layer. No other secondary structures could be detected in XRD or Raman.

Next to the OLA stabilized NCs, thiol capped CZTS NCs films were also treated with the same sulfurization process. As discussed in section 8.3, these layers contain a slightly smaller amount of carbon (3.4 wt%). Nevertheless, Figure 10.3 indicates that the sulfurization process has a very similar effect as compared to the OLA stabilized NCs. Again, a coarse grained layer is formed on top of a fine

Element	As-Deposited	Top Layer	Bot Layer
S	48.3%	50.5%	55.1%
Cu	20.7%	24.8%	13.2%
Zn	14.0%	12.3%	14.5%
Sn	11.9%	12.4%	11.3%
C	5.1%	0%	4.9%

Table 10.1: Table containing the atom percentages of SEM-EDX results of a OLA NC based CZTS film Left: as-deposited. Middle: Top layer. Right: bottom layer

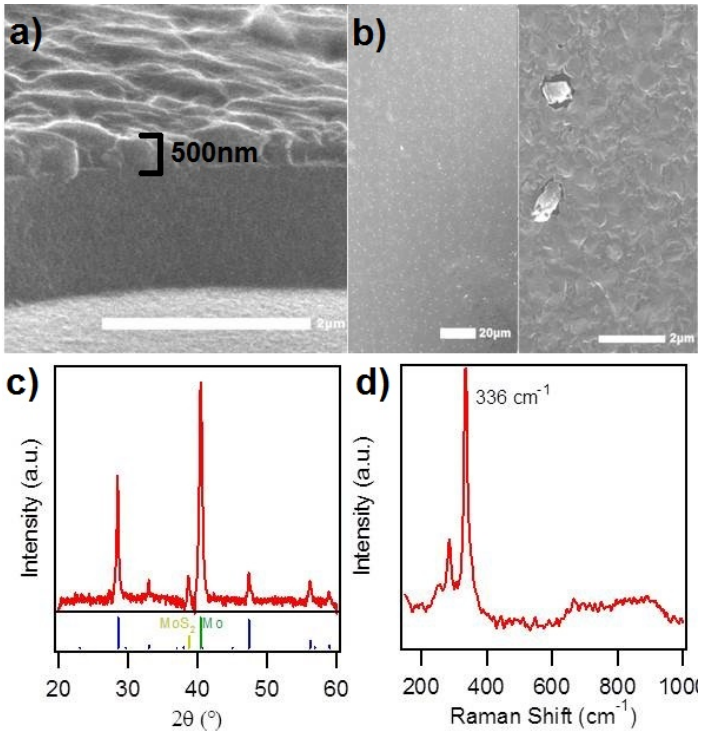

Figure 10.3: A sulfurized layer of OT capped CZTS NCs . (a) A cross-sectional image of the layer. (b) A top view of the layer, showing the crystalline crack free top layer. (c) XRD reflections of the layer. (d) Raman spectrum of the layer.

grained one, where the crystals in the top and the bottom layer have the same size as compared to the layer fabricated with OLA NCs. The top view in Figure 10.3b) reveals that the top crystalline part spreads over the film without crack formation. The formation of kesterite and MoS_2 can again be deduced from the XRD reflections (Figure 10.3c), whereas the Raman spectrum confirms that indeed kesterite is formed (Figure 10.3d).

10.3.2 Sulfurization of Carbon Free CZTS Nanocrystal Films

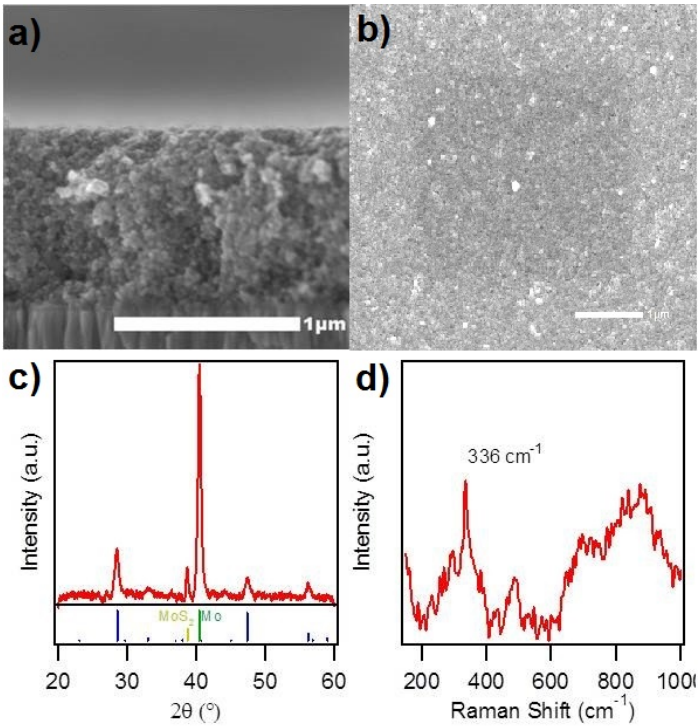

Figure 10.4: A sulfurized layer of sulfide capped CZTS NCs . (a): A cross-sectional image of the layer. (b): A close view on the NCs in the film. (c): XRD reflections of the layer. (d): Raman spectrum of the layer.

SEM images of a carbon-free CZTS/S^{2-} NC film sulfurized using the same conditions as in the previous section are shown in Figure 10.4. It follows that in this case, hardly any grain growth has occurred, with the crystallites retaining diameters of 20-30 nm. In line with this observation, the XRD reflections show broad peaks and only a faint resonance at 336 cm^{-1} – characteristic of kesterite – is present in the Raman spectrum.

10.3.3 Selenization of Steric Stabilized CZTS Nanocrystal Films

For sulfurization of sterically stabilized NC films we are limited to grain growth of a layer of 500 nm thick. Hopefully we can improve this using selenization. To compare the result of the sulfurization, we anneal a sterically stabilzed film (OLA) using a Se-atmosphere.

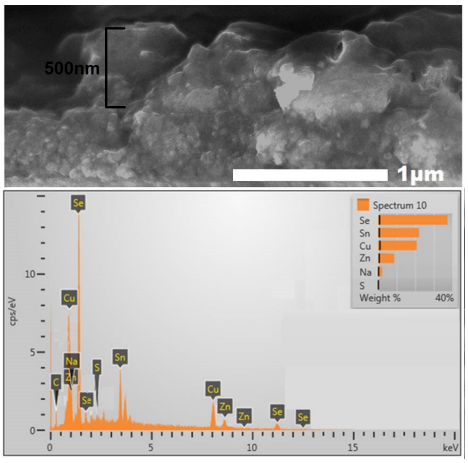

Figure 10.5: Top: a cross-section of the selenized C-containing CZTS layer. Bottom: An EDX SEM spectrum of the same NC layer. Indicating that all S is replaced by Se

After annealing we analyze the results using XRD, Raman and SEM and the results are similar to what we achieved for sulfurization. SEM images of the cross section of the layer and the corresponding EDX characterization are shown in Figure 10.5. It follows that again a top layer is formed containing coarse, 500 nm sized crystals that cover the entire film. These structures are large CZTSe crystals (confirmed with Raman and XRD in Figure 10.6c and d). The bottom layer on the other hand still contains small NCs that have hardly grown as compared to the originally present CZTS NCs. EDX indicates that all S initially present was replaced by Se, even in the nanocrystalline bottom layer. Hence, although the S-Se replacement took place, no growth was observed in the bottom layer.

10.3.4 Selenization of C-Free CZTS Nanocrystal Films

Since the selenization of C-containing film resulted in the double layered structure we switch – just like in the sulfurization case – towards C-free layers. We use Sulfide stabilized NCs and we selenize using a closed graphite box containing the layer and black selenium. We anneal by heating the closed graphite box to 550 °C. Results are shown in Figure 10.7. It shows that for selenization of C-free CZTSe NC inks the film does not show the double layered structure. But there is a slight increase in NC growth compared to the sulfurization of carbon free CZTS NCs in section 10.3.2. The layer is shown in Figure 10.7 a and b on top and it consists of 100 nm large CZTSe crystals. Some larger crystals (500 nm) of CuSe are formed on top of the layer according to SEM-EDX, These can not be detected on XRD since chalcopyrite CuSe coincides with the kesterite reflections.

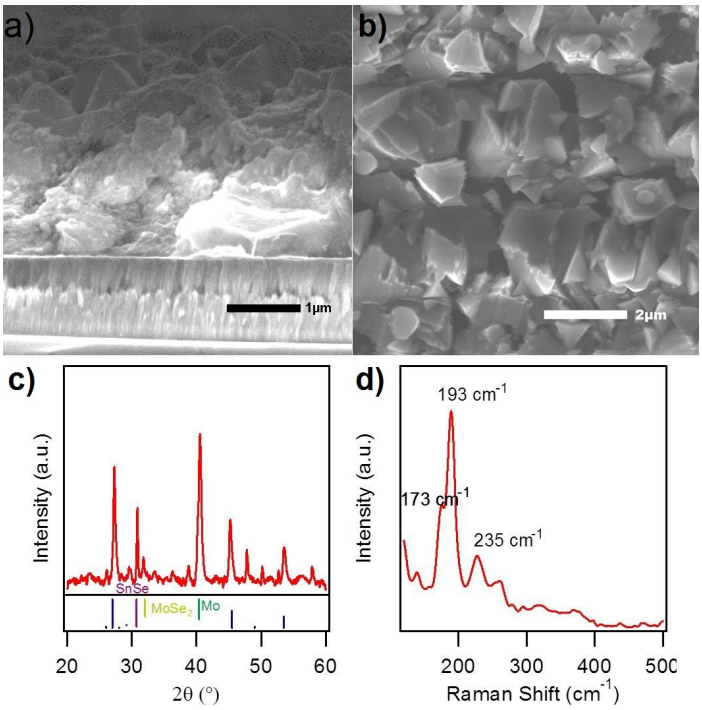

Figure 10.6: A selenized sample of C-containing CZTS NC layer. (a) and (b): A top view image of the layer showing a crystalline layer on top. (c) XRD reflections of the layer, indicating a kesterite (CZTSe) crystal structure. (d) A Raman spectrum of the layer indicating CZTSe

The measured XRD reflections (Figure 10.7 c) fit those of kesterite and using Raman spectroscopy the presence of kesterite could be confirmed(Figure 10.7 d). A small amount of secondry phase is present on the surface. The presence of CuSe crystals could be confirmed from XRD. But the formation of secondary phases does not have to be a problem. Etching techniques have been developed to remove secondary phases (CuSe and ZnSe) and improve device performance [10, 19].

10.3.5 Device Fabrication

The sulfurized CZTS layers were integrated in solar cells, where on every square inch of the substrate, 8 devices were defined. Figure 10.8 shows an example of 4 completed devices. The cells were fabricated by depositing an ≈50 nm thick n-CdS layer on top of the CZTS film using chemical bath deposition. This layer was further contacted with a ZnO layer as a transparent conductive window. The stack is similar as in Figure 2.7.

For a CZTS film made by sulfurization of a layer of octanethiol capped CZTS

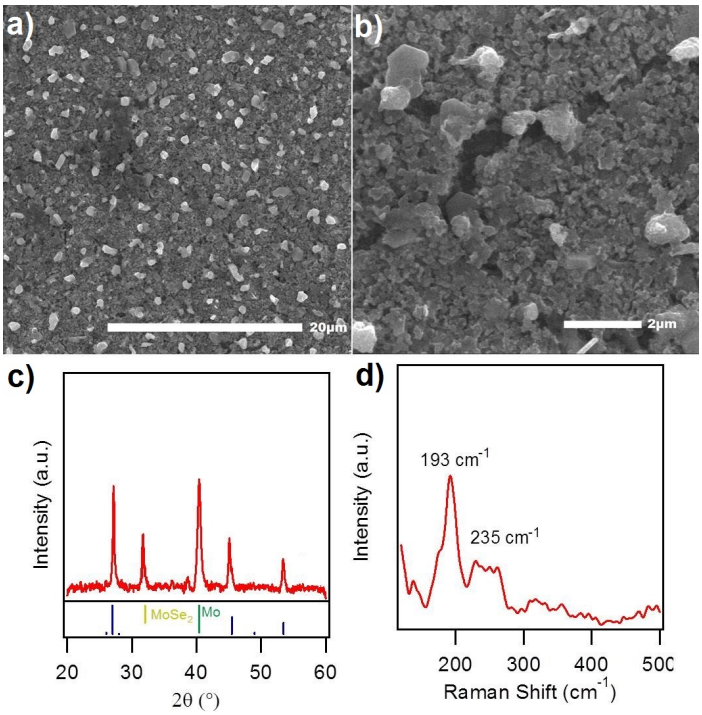

Figure 10.7: A selenized sample of a C-free CZTS NC layer. (a) and (b) A top view image of the layer showing a crystalline layer on top. (c) XRD reflections of the layer, indicating a kesterite (CZTSe) crystal structure. (d) A Raman spectrum of the layer indicating CZTSe

NCs, this resulted in 8 working devices. These devices showed an efficiency between 1.70 and 2.23%, with a mean efficiency of 2.03%. The IV and PV curve of the most performing device is shown in Figure 10.8b. It features an open circuit voltage (V_{OC}) of 0.33 V, a short circuit current (j_{SC}) of -0.009 A cm^{-2} and a fill factor of 0.403 with a maximum efficiency of 2.23%.

The efficiencies of OLA based NCs CZTS devices were significantly lower, ranging between 0 and 1.46% with an average of 0.43%. The most efficient cell is shown in Figure 10.8c. This device exhibits a V_{OC} of 0.247 V, a j_{SC} of -0.008 A cm^{-2} and a fill factor of 0.406, which resulted in a efficiency of 1.46%.

For the CZTS C-free layer we did not obtain any efficiencies, an IV and PV curve is shown in Figure 10.8d. Here, a V_{OC} of 0.0033 V, an j_{SC} of -0.0012 A cm^{-2} and a fill factor of 0.000 was obtained, thus resulting in a efficiency of 0.00%.

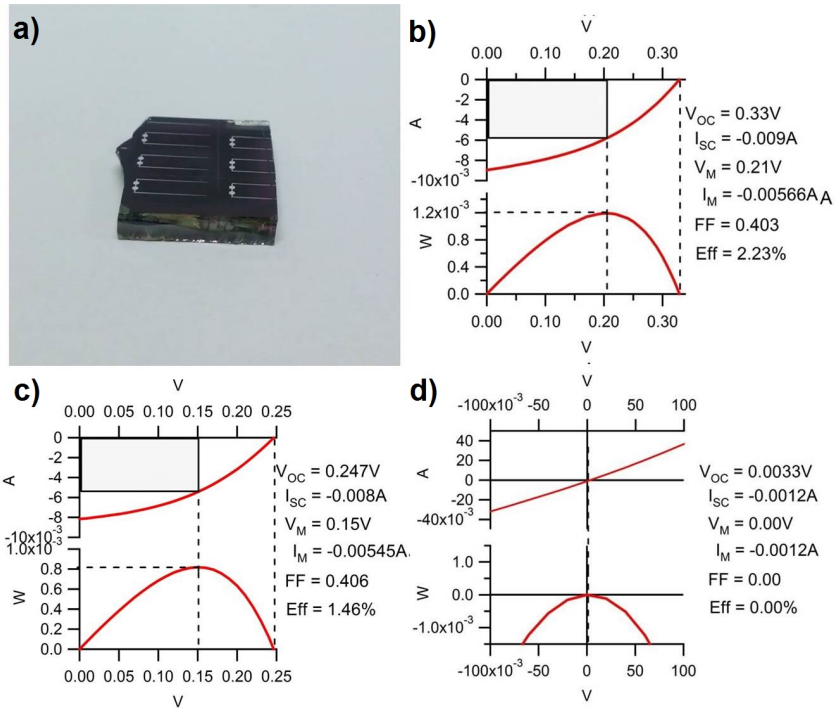

Figure 10.8: (a): A fabricated device of a sulfurized CZTS layer. (b): The IV and PV curves of a device containing an absorberlayer of sulfurized CZTS NCs capped with thiols. (c): The IV and PV curves of a CZTS cell of OLA capped CZTS NCs. (d): The IV and PV curves of a C-free sulfurized CZTS NC layer.

10.4 Discussion

The survey of sulfurization and selenization of the CZTS and CZTSe NCs with different surface termination indicates that the presence of carbon in the initial NC layer systematically has the same effect on the final layer. Both with OLA and octanethiol ligands, always a double layered structure is obtained with a 500 nm microcrystalline, carbon-free CZTS(e) top layer and a nanocrystalline, carbon-rich bottom layer. The annealed carbon-free CZTS(e) layers on the other hand preserve their original nanocrystalline structure. This indicates that the initial presence of carbon is not preventing – possibly even promoting – recrystallization to start at the top of the NC film, which is a typical high interfacial energy area where recrystallization preferentially starts. However, since the recrystallization does not extend over the entire film thickness the eventual removal of carbon seems an essential step to achieve complete recrystallization.

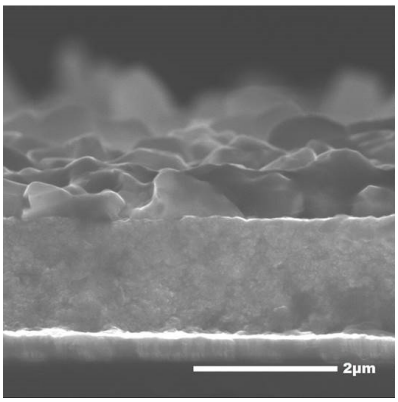

Figure 10.9: A selenized NC layer of a C-free NC ink but with the C-containing and high boiling ethylene glycol as solvent. (a) Cross section showing a double layered structure. (b) top view indicating that the sample is covered with larger crystals.

To confirm that this bilayer formation can be attributed to the presence of carbon in general, and not so much to the presence of particular steric stabilizers, we selenized a sample of carbon-free (sulfide) stabilized NC using ethylene glycol (EG) as the solvent, which lead to a carbon residue in the dried layer of 2.73%. After selenization we found that, identical to other carbon-containing inks, a double layered film occurred with coarse crystals on top and a small grained NC layer at the bottom (see Figure 10.9a), with a similar thickness of ≈500 nm. We do conclude that the formation of a coarse grain/fine grain double layer structure is linked to the presence of significant amounts of carbon-containing residues in the original NC film, irrespective of their origin (ligands or solvent).

Although we have concluded that any carbon source results in a double layer,

we found that slight difference in roughness result from using either thiols or OLA as the NC ligand. This can be linked to the densification of this top layer. As compared to octanethiol, OLA is a more voluminous ligand that leaves a higher residual carbon contamination in an selenized on sulfurized layer. Since the recrystallized 500 nm thick top layer is carbon free, this implies that the volume loss when starting from OLA capped NCs will be larger. This volume loss occurs in every direction, resulting in a rougher surface. The roughness of the top layer may have a negative effect on the device fabrication. A better pn-junction can be expected to form if the CdS is deposited on a smooth layer. This may explain the better cell efficiencies measured for CZTS cells made starting from octanethiol stabilized NCs.

10.5 Conclusions

We have analyzed the structural and compositional changes in films of NC films with different surface termination during sulfurization and selenization. For carbon-free NCs, we find that the film maintains its original nanocrystalline structure, resulting in disfunctional solar cells. Using films of NCs stabilized by organic ligands such as oleylamine or octanethiol, we systematically find that selenization and sulfurization leads to a double layer structure. The layers feature a coarse grained top film consisting of 500 nm large CZTS or CZTSe crystallites and a fine grained, nanocrystalline bottom layer. Whereas the top layer always consisted of a carbon-free stoichiometric CZTS(e), the bottom layer proofed to be Cu poor and had maintained its original carbon content. The use of different ligands results in layers with varying smoothness and, eventually, cell efficiency. This may be linked to the initial residual carbon contant, where denser starting layers (less carbon) yield smoother films and solar cells with better conversion efficiencies.

11

Ternary $Cu_2SnS(e)_3$ Nanocrystal Assisted Crystal Growth

11.1 Introduction

The use of quaternary CZTS NCs as precursors resulted in CZTS(e) films with sub optimal characteristics. Films made from sulfide stabilized NCs showed little sintering and grain growth whereas films based on sterically stabilized NCs transformed into bilayer films. A possible way to combine the benefits of carbon-free NCs with an enhanced recrystallization is the use of composite precursors. An example here is a mixture of ternary CTS and binary ZS NCs which reacts during sulfurization or selenization to form CZTS(e):

$$Cu_2ZnS + SnS_2 \rightleftharpoons Cu_2ZnSnS_4$$

This reaction will only proceed to form CZTS when the above reaction has a negative reaction free energy. According to literature, this is the case for binary NCs up to a temperature of 633 °C, which means that no binary composites should form when a precursor mixture has the right stoichiometric Cu:Zn:Sn:S(e) 2:1:1:4 composition [20]. A possible advantage of precursor mixtures is that one of the precursors may act as a fluxing agent that facilitates the formation of large crystallites. Hence the initial idea of investigating the CTS/ZS combination, where CTS could play this role [11].

In this chapter, we analyze the transformation behavior of mixed CTS/ZS NC films by sulfurization and selenization. The sulfurization experiments were conducted in collaboration with Prof. P. Dale (University of Luxembourg), while selenization was conducted in collaboration with Dr. M. Meuris (imec).

11.2 Experimental

11.2.1 Synthesis

The synthesis of the NCs has been discussed in Part 1 of this thesis. Two types of CZTS NCs have been synthesized. Cu poor ($Cu_{1.6}SnS_{2.8}$) and stoichiometric Cu_2SnS_3. ZnS has been synthesized using oleic acid (OA) as a ligand.

11.2.2 Processing

Processing of sterically stabilized inks. The NC were first exchanged to their respective stabilizer. Cu poor CTS and ZnS were separately dispersed in octanthiol and subsequently mixed in a 1:1.2 ratio. A layer of 1.5 μm was deposited using multi layer deposition of CTS NCs and of the CTS-ZS mixture.

Processing of sulfide stabilized inks. For C-Free CTS+ZS layers the NCs were first separately exchanged into DMSO using ammonium sulfide. After exchange 2 mixtures were formed. A mixture with stoichiometric CTS NCs and a 1:1 ratio with ZnS and another mixture using Cu poor CTS NCs and an 1:1.2 excess of ZnS NCs. A 2 wt% of ammonium sulfide was added to the ink for stabilization. A layer of C-Free CTS NCs of 1.5 nm has been deposited. A 1.5 μm layer has been deposited of the CTS + ZS Cu-poor zn-rich NC mixture has been deposited. And a 1.5 μm layer of CTS and ZS NCs in a stoichiometric ratio has been deposited.

11.2.3 Sulfurization

The same sulfurization process as in Section 10.2 has been used. In brief, sulfurization was preformed in a graphite box that was placed in a tube furnace. The tube furnace was flushed and placed under a pressure of 1 mbar in a N_2 + %5H_2 atmosphere. In the graphite box, a square inch sized molybdenum coated lime glass sample with a layer of CZTS NCs was placed together with 100 mg of elementary S and 20 mg of tin sulfide

11.2.4 Selenization

Samples were selenized using H_2Se. The samples were treated for 15 minutes in a flow of 60 standard cubic centimeter per minute (sccm) H_2Se 10% and 20 sccm

H_2S. The temperature was measured on the backside of the sample with lamp heating from the top, so the top surface temperature was likely closer to 500 °C.

11.3 Results And Discussion

11.3.1 Sulfurization of CTS Nanocrystals

Since CZTS is thermodynamically more stable than its composites for the 2:1:1:4 stoichiometry, we opt to use a composite ink to induce recrystallization with the goal of forming large CZTS crystals. In principle, various combination are possible to form a composite ink, but we opted for the combination of Cu_2ZnS_3 (CTS) and ZnS (ZS) for multiple reasons. In terms of synthesis and formulation the combination of these two was the most straightforward. Both NC synthesis gave high yield, were reproducible and could easily be tuned in the desired composition (Cu poor CTS NCs). Concerning formulation the Cu-Zn-Sn stoichiometry could easily be tuned by the addition of ZnS in the CTS NC dispersion. Another advantage was that both materials could be exchanged from an OLA based ink to a thiol based or carbon free ink. This exchange was troublesome for composites such as Cu_2S(e) and SnS(e).

A second reason is that we aim for liquid assisted growth, if possible. Under these conditions, one of the composites forms a liquid phase (flux) that can flow through the NC layer and thus enhance the recrystallization throughout the layer. Since a phase diagram showing the solid solution of the composites is not available, we assessed the different precursors from their respective melting points. Both Cu_2S (1130 °C) and ZnS (1180 °C) have a melting point well above typical temperatures used during transformation, making it very unlikely fluxing agents. SnS_2 on the other hand has a melting point of only 600 °C, yet this compound will preferably sublimate instead of forming a liquid phase. [17] CTS on the other hand has a melting point of 837 °C. This bulk melting point is still considerably higher then the temperature range (500-550 °C) used for annealing. However, NCs may exhibit a melting point reduction of hundreds of degrees as compared to the bulk counterpart [21], meaning that CTS when present as NCs is not an unlikely fluxing agent.

To explore the transformation behavior of CTS NCs, we first sulfurized a film of CTS NCs capped with OLA. The results are displayed in Figure 11.1a, where again the characteristic double layered structure with large crystals on top and a granular layer at the bottom is obtained. This does not indicate any melting point depression, but just confirms the findings of the previous chapter that in the presence of carbon a NC film is transformed into a double layered structure. We thus conclude that the use of carbon stabilized CTS NCs has little or no benefit as compared to CZTS(e) NCs.

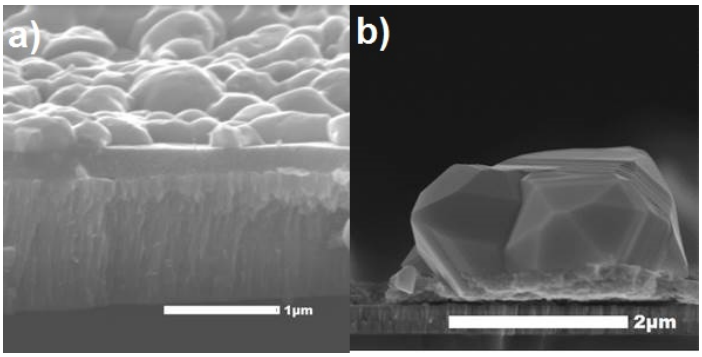

Figure 11.1: (a) A sulfurized layer of CTS NCs capped with OLA. (b) a sulfurized layer of C-free CTS NCs.

When sulfurizing CTS NCs capped with sulfides, a completely different picture emerges (see Figure 11.1b). In this case, the NC films breaks apart in a collection of large, micron-sized CTS crystallites that spread as separate entities over the substrate. This gives the impression that the CTS NCs indeed form a liquid state during sulfurization that forms large crystallites during cooling. Hence, it seems that a phase has been found that can induce liquid assisted growth and which melts at a temperature considerably lower than its bulk counterpart. Analysis by SEM-EDX indicated that the crystallites have the 2:1:3 stoichiometry of CTS. Note that the Mo substrate is still covered by a thin film of nanocrystallites, which proved to be Cu poor and Sn rich. Extra Sn might have been incorporated through the gas phase.

11.3.2 Selenization of CTS Nanocrystals

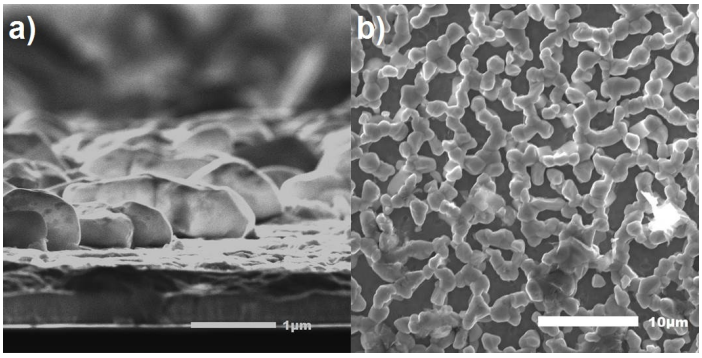

Figure 11.2: C-free CTS NCs after selenization. (a) cross section. (b) Top view of the layer.

As shown in Figure 11.2, selenization of carbon-free CTS NCs had a similar effect as sulfurization. Again, the top view and cross sectional SEM images show that large crystals are formed with diameters larger than 2 μm and having the 2:1:3 stoichiometry of CTSe.

We performed a map of the main elements present, being Cu, Sn, Se and Mo/S. Results can be seen in Figure 11.3. All Cu and Sn is concentrated in the big crystals, confirming the visual results that in this case no small granular NCs are left as was the case for sulfurization in Figure 11.1. Mo and S overlap in an EDX spectrum, but we can notice that no Mo/S signal is present for the large crystals which indivated to complete substitution of S by Se. While the substrate is clearly visible in between the crystals from the side and the top view.
In conclusion we can say that C-free CTS has great potential in introducing a composite that can enhance recrystallization. Using C-free CTS in combination with ZnS particles we could enhance the crystal growth within the layer compared to quaternary particles.

11.3.3 Annealing of Steric Stabilized CTS + ZS Nanocrystal Films

When using the CTS particles combined with ZnS particles without a ligand exchange (OLA capped particles) a double layered structure was obtained due to the presence of organics. Here, the same thickness for the CZTS crystalline layer is obtained as for the quaternary sample in section 10.3.1. A small difference here is that Raman shows a second peak at 408 cm^{-1} which corresponds to a possible CTS Raman peak, indicating that the bottom layer is still a mixture of CTS and ZS NCs instead of the desired CZTS NCs. Similar results are found for the selenization of a CTS + ZS layer containing organics.
This indicates that the mechanism of splitting the CZTS NC layer into a composite layer has no effect on the final result if carbon is present. Even though we know that C-free CTS has different properties compared to the C-Free CZTS, the results in the top layer is exactly the same, and also in the bottom layer no growth occurs. To make use of the crystal growth properties of CTS we will have to switch to a complete C-free environment.

11.3.4 Sulfurization of C- free CTS + ZS Nanocrystal Films

Sulfurization of CTS NCs showed that CTS NCs when used in a composite, carbon free precursor ink may serve as a fluxing agent to improve the crystal structure of the eventual CZTS(e) layer. Therefore, composite inks containing a mixture of ternary CTS and binary ZS were used to form crack- and carbon-free NC layers. Figure 11.5 shows SEM images of the layers obtained after sulfurization. The extensive crystal growth we observed for CTS NCs is not observed in this case.

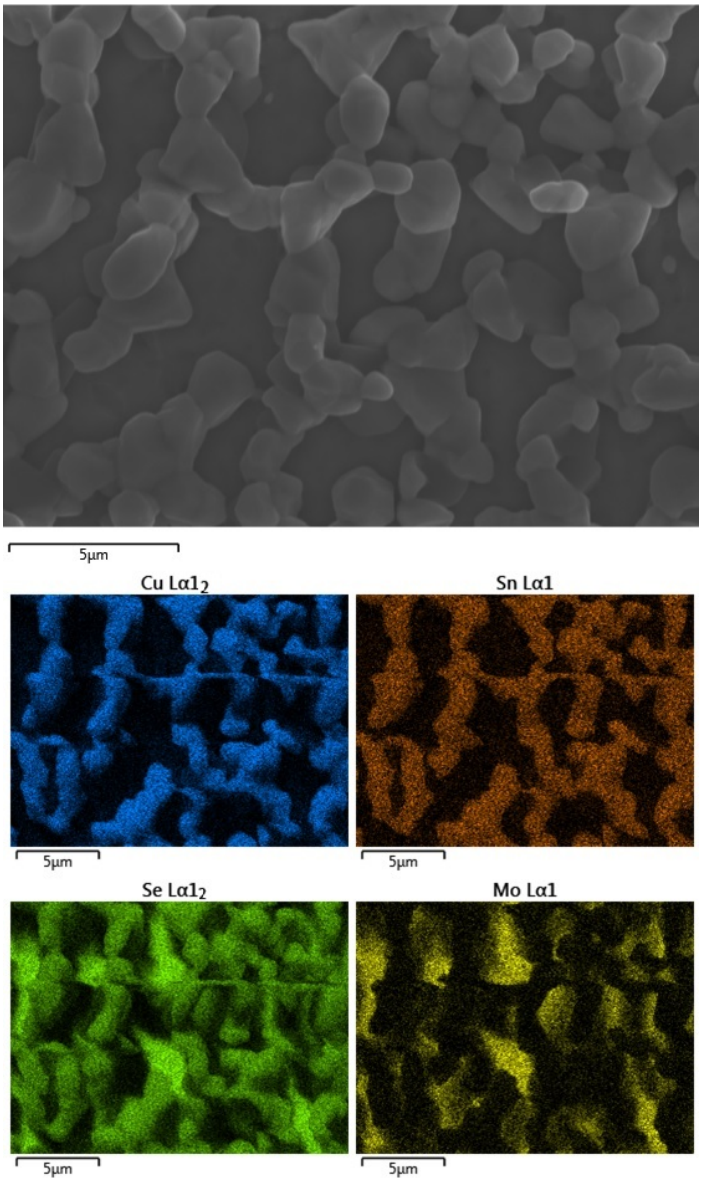

Figure 11.3: A EDX-map of the main elements present in our thin film absorber layer.

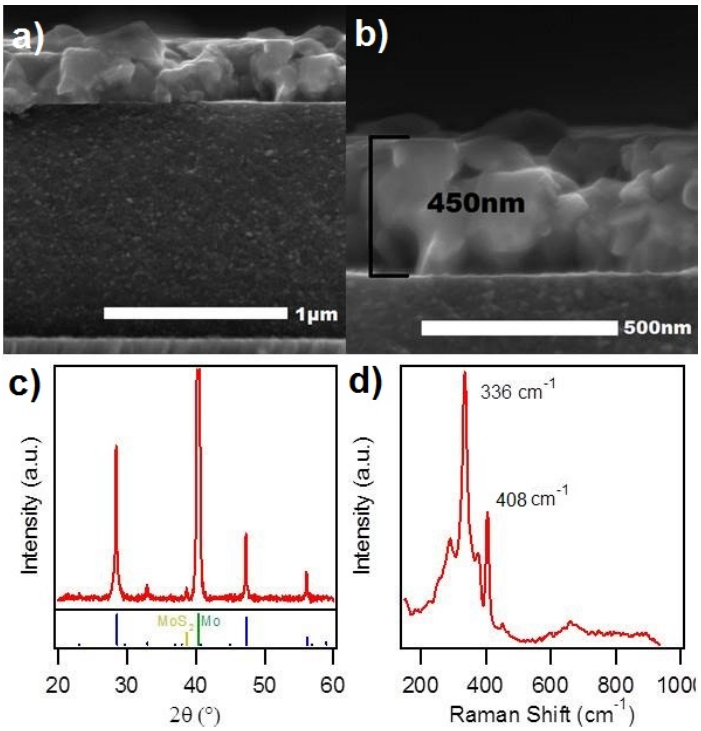

Figure 11.4: A sulfurized layer of organic capped ZS and CTS NCs . (a) A cross-sectional image of the layer. (b) A close view on the crystalline part of the layer. (c) XRD reflections of the layer. (d) Raman spectrum of the layer.

Instead, slight growth throughout the layer is detected. The cross section image shown in Figure 11.5b indicates that the layer has lost its small 20-30 nm NC structure, whereas bigger crystallites of with dimensions of ≈100 nm or more have been formed. When analyzing the width of XRD reflections as displayed in Figure 11.5c using the Debeye Scherrer equation, we find structures with a diameter of 35-40 nm. This is significantly larger than the original crystallites (13.3 nm) and the 16.7 nm sized CZTS carbon-free NCs after annealing. However, as compared to the +2 μm sized CTS crystals obtained by annealing CTS NCs, the growth is somehow limited. Raman spectroscopy (Figure 11.5 d) indicates that indeed kesterite has formed from the combination of binary and ternary NCs, yet the small peak at 408 cm^{-1} indicates that a small amount of CTS NCs remained.

The absence of truly pronounced recrystallization after sulfurization after incorporation of ZS in the CTS NCs indicates that once both compounds react to form CZTS in the carbon-free environment of the film, no further crystal growth occurs. This was already observed in the sulfurization of carbon-free quaternary

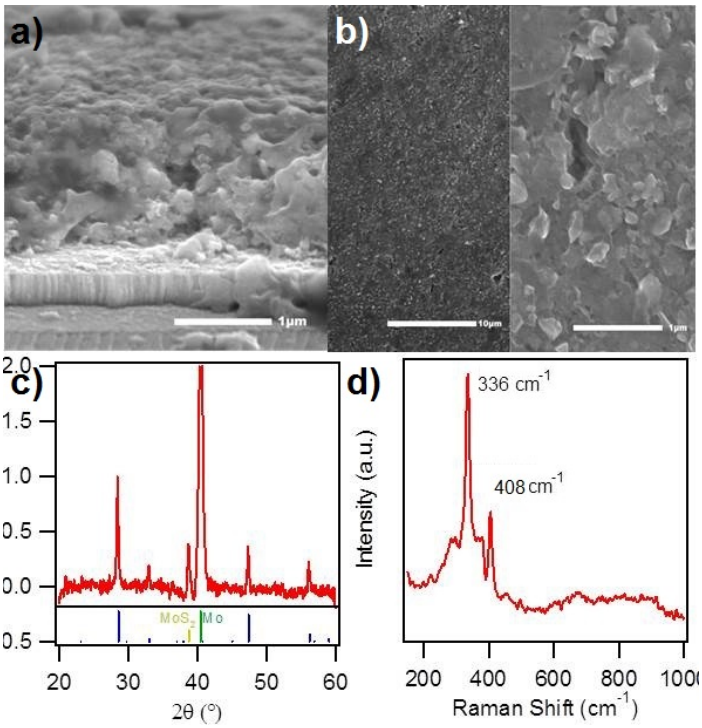

Figure 11.5: A sulfurized layer of C-free ZS and CTS NCs . (a) A cross-sectional image of the layer. (b) A close view on the top of the layer. (c) XRD reflections of the layer. (d) Raman spectrum of the layer.

CZTS NCs in section 10.3.2, where no recrystallization occurred when using CZTS as a starting material. Hence, it appears that the CZTS NCs themselves seem to lay at the origin of the poor recrystallization behavior in a carbon-free film. This conclusion is not unlikely since CZTS(e) is already the phase with the lowest free energy.

The CZTS layers formed out of the combination of CTS and ZS were incorporated in solar cells, yet they did not show any measurable conversion efficiency.

11.3.5 Selenization of C-Free CTS + ZS Composite Layers

The limited recrystallization during sulfurization could be due to the presence of sulfoxides that are formed on the NC surface as seen in Chapter 9. There we have seen that the use of a reducing atmosphere helps with the removal of these sulfoxides and shows slight, although limited, improvement in recrystallization. The combination of a reducing atmosphere and selenium might thus improve the

recrystallization and densification. We therefore annealed CTS + ZS mixed precursor films in the presence of H_2Se. Since CZTS is preferably Zn rich, these experiments initially made use of a precursor with an overall 1.6:1.2:1:4 Cu:Zn:Sn:S stoichiometry. This is the preferred stoichiometry in which the most optimal performances have been recorded [11, 22].

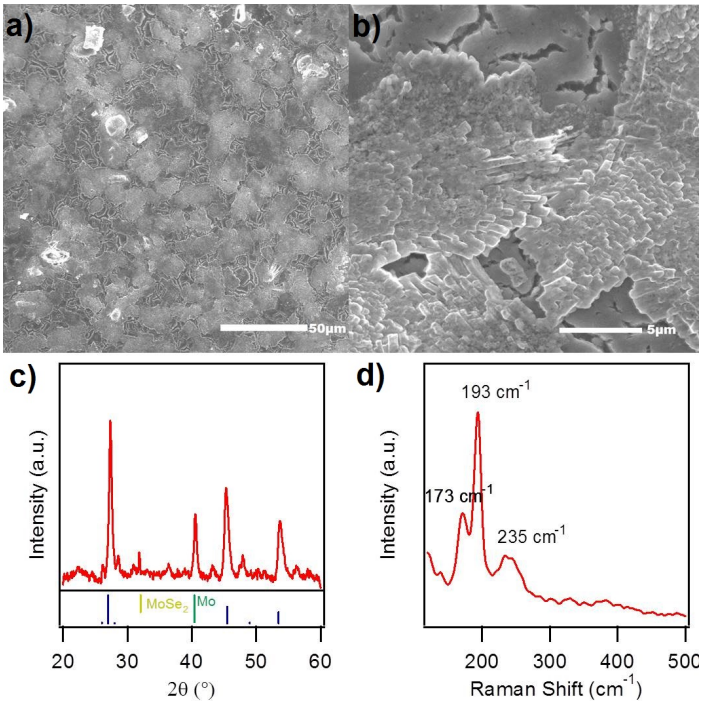

Figure 11.6: CTS+ZS NC ink with a 1.6-1.2-1-4 Cu-Zn-Sn- ratio (a) and (b) An SEM top view image of the layer after selenization with a H_2Se atmosphere. (c) XRD reflections of the layer. (d) Raman spectrum of the laser using a 473 nm laser.

When selenizing the Zn-rich sample (1.6:1.2; Cu:Zn), XRD and Raman confirm the formation of CZTSe during the reaction. However larger crystallites in combination with small NCs are obtained as is clearly visible in Figure 11.6. This indicates that a total recrystallization remains absent. Bigger crystallites are formed, showing that the recrystallization process can occur. but on the other hand a clear NC layer still remains. If we analyze the big crystallites and the small NCs using SEM-EDX we find that the recrystallized layer contained stoichiometric CZTS. But the granular layer exhibits Zn-rich and Cu-poor in a Cu-Zn 1:1 ratio. We can deduct that the large crystallites only could be formed in a limited amount due to the lack of Cu.

The deficit of Cu and excess of Zn is inhibiting our CTS assisted growth in the

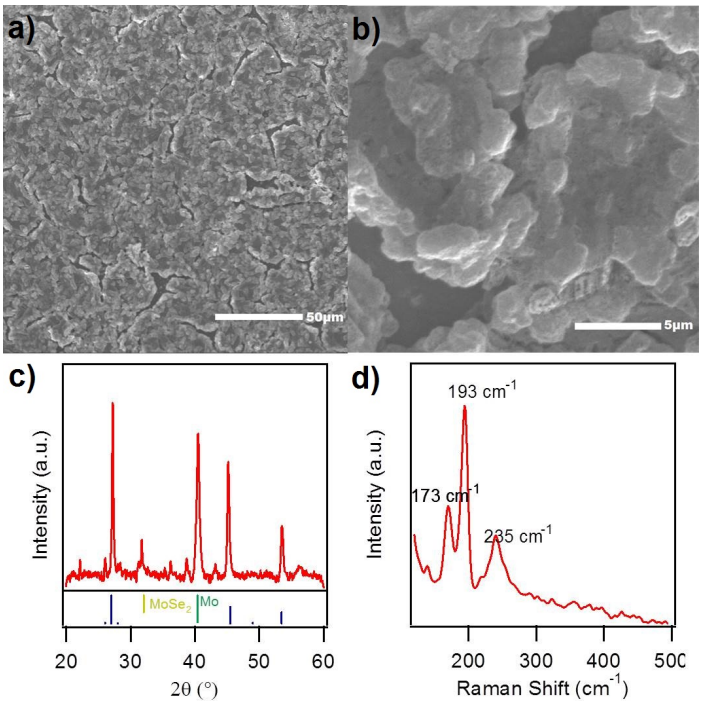

Figure 11.7: CTS+ZS NC ink with a 2-1-1-4 Cu-Zn-Sn- ratio (a) and (b) an SEM top view image of the layer after selenization with a H_2Se atmosphere. (c) XRD reflections of the layer. (d) Raman spectrum of the laser using a 473 cm^{-1} laser.

granular part. The granular part no longer consists of CTS an ZnS but mostly of a Cu-poor Zn-rich CZTS which does not show any crystal growth (see Zn-rich Cu-poor CZTS in figure 10.7). Therefore we also applied a stoichiometry of 2-1-1-4 ratio in Cu-Zn-Sn-S, which is the standard stoichiometric ratio without any Zn excess and with a sufficient amount of Cu. The results of the 2:1 Cu:Zn ratio sample are shown in Figure 11.7. XRD and Raman spectroscopy confirm the formation of CZTSe. Large crystallites are visible and no granular layer is formed. This shows that the introctuction of ZnS in a CTS matrix is possible as long as there is no excess of Zn compared to the stoichiometric CZTS. Once the CTS matrix is enriched with ZnS to form stoichiometric kesterite the lowest point of free energy is reached. A further transformation will not occur, leaving stoichiometric CZTS and a granular residue in the case of a ZnS excess, but it allows a full recrystallization in the case of stoichiometric CTS + ZnS.

The cross section in Figure 11.8 shows that the Cu:Zn 2:1 sample has no bilayered structure but large grains throughout the layer. For the Zn rich sample grain

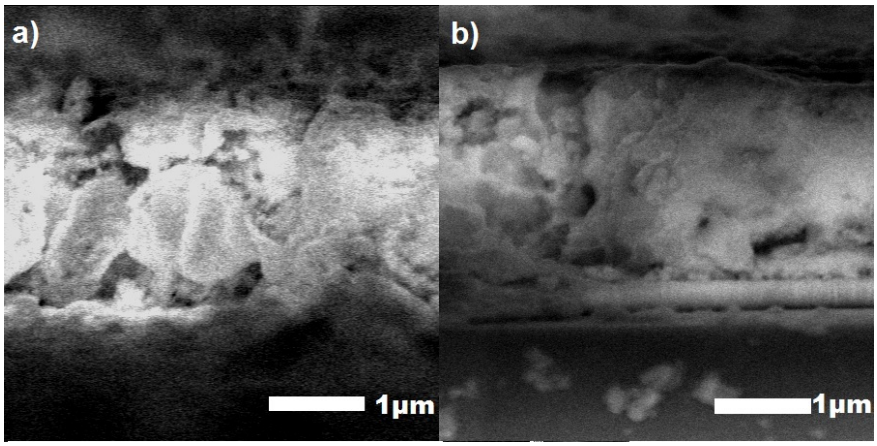

Figure 11.8: (a) cross section of the Cu:Zn 2:1 ratio sample. (b) Cross section of the Cu:Zn 1.6:1.2 ratio.

growth is less significant. A disadvantage coming from the successful densification is that cracks are formed throughout the layer. The cracks seem to be present due to the phase transformation of the film. Our original films deposited using CTS + ZS in a C-free ink discussed in Section 8.5 also lead to the fabrication of a relatively porous film. If the top layer is studied in more detail, we notice that it has transformed into dense crystals with a diameter up to 2 μm. Since the film was porous in an as-deposited state, the volume reduction due to densification is considerable. This volume reduction is responsible for crack formation. If we would be able to start from a denser C-free layer we might avoid cracking upon annealing.

11.4 Conclusions

C-Free samples containing CTS NCs show extensive recrystallization. The CTS NCs without the presence of Zn form micron-sized crystals which gives evidence of huge atomic mobility, meaning that CTS NCs can act as a fluxing agent during sulfurization and selenization. When mixing these CTS NCs with ZS NCs recrystallization occurs. But for sulfurization this recrystallization is limited to a NC level and the full recrystallization of micro sized crystals is still absent. In a CTS + ZS Zn-rich sample, CZTSe crystals form randomly on top of the layer, but a Zn-rich small grained layer is still present. However, when transforming a stoichiometric layer the complete layer transforms into larger crystallites, showing great potential in forming a dense CZTS film. Unfortunately, the starting layer of C-free CTS + ZS particles is slightly porous, with the result that the densifica-

tion leads to an important volume reduction which results in cracks, showing the Mo substrate. The latter should be avoided, because this would be devastating for device performance.

References

[1] H. Zhou, W.-C. Hsu, H.-S. Duan, B. Bob, W. Yang, T.-B. Song, C.-J. Hsu, and Y. Yang, "CZTS nanocrystals: a promising approach for next generation thin film photovoltaics," *Energy Environ. Sci.*, vol. 6, no. 10, pp. 2822–2838, 2013.

[2] V. A. Akhavan, B. W. Goodfellow, M. G. Panthani, C. Steinhagen, T. B. Harvey, C. J. Stolle, and B. A. Korgel, "Colloidal CIGS and CZTS nanocrystals: A precursor route to printed photovoltaics," *Journal of Solid State Chemistry*, vol. 189, pp. 2–12, 2012.

[3] C. Steinhagen, M. G. Panthani, V. Akhavan, B. Goodfellow, B. Koo, and B. A. Korgel, "Synthesis of Cu2ZnSnS4 Nanocrystals for Use in Low-Cost Photovoltaics," *Journal of the American Chemical Society*, vol. 131, no. 35, pp. 12554–12555, 2009.

[4] S. A. (), K. H. K. (), J. H. Y. (), and K. H. Y. (), "Effects of selenization conditions on densification of Cu(In,Ga)Se2 (CIGS) thin films prepared by spray deposition of CIGS nanoparticles," *Journal of Applied Physics*, vol. 105, no. 11, pp. –, 2009.

[5] D. L. Schulz, C. J. Curtis, A. Cram, J. L. Alleman, A. Mason, R. J. Matson, J. D. Perkins, and D. S. Ginley, "CIGS films via nanoparticle spray deposition: attempts at densifying a porous precursor," in *Photovoltaic Specialists Conference, 1997., Conference Record of the Twenty-Sixth IEEE*, pp. 483–486, IEEE, 1997.

[6] M. Drndić, M. V. Jarosz, N. Y. Morgan, M. A. Kastner, and M. G. Bawendi, "Transport properties of annealed CdSe colloidal nanocrystal solids," *Journal of applied physics*, vol. 92, no. 12, pp. 7498–7503, 2002.

[7] M. G. Panthani, V. Akhavan, B. Goodfellow, J. P. Schmidtke, L. Dunn, A. Dodabalapur, P. F. Barbara, and B. A. Korgel, "Synthesis of CuInS2, CuInSe2, and Cu (In x Ga1-x) Se2 (CIGS) Nanocrystal Inks for Printable Photovoltaics," *Journal of the American Chemical Society*, vol. 130, no. 49, pp. 16770–16777, 2008.

[8] R. Dierick, B. Capon, H. Damm, S. Flamee, P. Arickx, E. Bruneel, D. Van Genechten, M. Van Bael, A. Hardy, C. Detavernier, and Z. Hens, "Annealing of sulfide stabilized colloidal semiconductor nanocrystals," *J. Mater. Chem. C*, vol. 2, no. 1, pp. 178–183, 2014.

[9] M. Kaelin, D. Rudmann, and A. N. Tiwari, "Low cost processing of CIGS thin film solar cells," *Solar Energy*, vol. 77, no. 6, pp. 749–756, 2004.

[10] C. Guillen and J. Herrero, "Effects of thermal and chemical treatments on the composition and structure of electrodeposited CuInSe2 thin films," *Journal of The Electrochemical Society*, vol. 141, no. 1, pp. 225–230, 1994.

[11] Y. Cao, M. S. Denny, J. V. Caspar, W. E. Farneth, Q. Guo, A. S. Ionkin, L. K. Johnson, M. Lu, I. Malajovich, D. Radu, H. D. Rosenfeld, K. R. Choudhury, and W. Wu, "High-Efficiency Solution-Processed Cu2ZnSn(S,Se)4 Thin-Film Solar Cells Prepared from Binary and Ternary Nanoparticles," *Journal of the American Chemical Society*, vol. 134, no. 38, pp. 15644–15647, 2012.

[12] Q. Guo, G. M. Ford, W.-C. Yang, B. C. Walker, E. A. Stach, H. W. Hillhouse, and R. Agrawal, "Fabrication of 7.2% Efficient CZTSSe Solar Cells Using CZTS Nanocrystals," *Journal of the American Chemical Society*, vol. 132, no. 49, pp. 17384–17386, 2010.

[13] M. Kaelin, D. Rudmann, F. Kurdesau, H. Zogg, T. Meyer, and A. N. Tiwari, "Low-cost {CIGS} solar cells by paste coating and selenization," *Thin Solid Films*, vol. 480481, no. 0, pp. 486–490, 2005.

[14] W. Wang, Y.-W. Su, and C.-h. Chang, "Inkjet printed chalcopyrite CuInxGa1xSe2 thin film solar cells," *Solar Energy Materials and Solar Cells*, vol. 95, no. 9, pp. 2616–2620, 2011.

[15] D. B. Mitzi, O. Gunawan, T. K. Todorov, K. Wang, and S. Guha, "The path towards a high-performance solution-processed kesterite solar cell," *Solar Energy Materials and Solar Cells*, vol. 95, no. 6, pp. 1421–1436, 2011.

[16] D. M. Berg, A. Crossay, J. Guillot, V. Izquierdo-Roca, A. Pérez-Rodriguez, S. Ahmed, H. Deligianni, S. Siebentritt, and P. J. Dale, "Simplified formation process for Cu2ZnSnS4-based solar cells," *Thin Solid Films*, vol. 573, no. 0, pp. 148–158, 2014.

[17] J. J. Scragg, T. Ericson, T. Kubart, M. Edoff, and C. Platzer-Björkman, "Chemical Insights into the Instability of Cu2ZnSnS4 Films during Annealing," *Chemistry of Materials*, vol. 23, no. 20, pp. 4625–4633, 2011.

[18] P. A. Fernandes, P. M. P. Salomé, and A. F. Da Cunha, "Growth and Raman scattering characterization of Cu¡ sub¿ 2¡/sub¿ ZnSnS¡ sub¿ 4¡/sub¿ thin films," *Thin solid films*, vol. 517, no. 7, pp. 2519–2523, 2009.

[19] A. Fairbrother, E. García-Hemme, V. Izquierdo-Roca, X. Fontane, F. A. Pulgarin-Agudelo, O. Vigil-Galan, A. Perez-Rodriguez, and E. Saucedo, "Development of a selective chemical etch to improve the conversion efficiency of Zn-rich Cu2ZnSnS4 solar cells," *Journal of the American Chemical Society*, vol. 134, no. 19, pp. 8018–8021, 2012.

[20] S. V. Baryshev and E. Thimsen, "Enthalpy of formation for Cu-Zn-Sn-S (CZTS)," Mar. 2014.

[21] H. H. Farrell and C. D. Van Siclen, "Binding energy, vapor pressure, and melting point of semiconductor nanoparticles," *Journal of Vacuum Science & Technology B*, vol. 25, no. 4, pp. 1441–1447, 2007.

[22] G. Brammertz, M. Buffiere, Y. Mevel, Y. Ren, A. E. Zaghi, N. Lenaers, Y. Mols, C. Koeble, J. Vleugels, M. Meuris, and Others, "Correlation between physical, electrical, and optical properties of Cu2ZnSnSe4 based solar cells," *Applied Physics Letters*, vol. 102, no. 1, p. 13902, 2013.

12

General Conclusions and Prospects

12.1 General Summary of the Research

This thesis elaborated on the synthesis of colloidal nanocrystals and their application in thin film photovoltaics. In a first part, we focused on a more economical method to form colloidal metal selenide nanocrystals, while preserving their high quality properties. In a first step, a fast and cheap method was introduced for the formation of CdSe nanocrystals or quantum dots, which has become a typical model system in the field. Consecutively, this method was extended to the formation of various nanocrsytals from the CZTS family. In the second part we studied the surface chemistry of the nanocrystals thus formed and its relation to the stability of nanocrystals dispersions or inks. The insights gained were used to develop stable inks that could be used to form crack free nanocrystal films. In the third part of this thesis, we studied the transformation of nanocrystal films in dense crystalline CZTS(e) films. We found recurring links between the nanocrystal surface termination – organic ligands or carbon-free inorganic moieties – and the sintering and densification of the layer. Even if this could not be used to form highly efficient CZTS(e) solar cells, this lead us to propose inks based on a mixture of copper tin sulfide/selenide and zinc sulfide/selenide nanocrystals stabilized by sulfide ions as a solution to avoid carbon contamination while promoting reactive sintering and grain growth.

12.2 Main Conclusions

12.2.1 Nanocrystal Synthesis

Concerning NC synthesis we have demonstrated that the injection of selenium powder dispersed in octadecene in a reaction mixture, containing either cadmium or zinc carboxylates dissolved in octadecene and an excess of carboxylic acid, initiates the formation of CdSe and ZnSe NCs. The reaction is fast, running to completion within 5-10 minutes, shows a high yield even for small NCs and leads to high quality NCs with low size dispersions. Moreover, in the case of CdSe, the final size of the NCs can be tuned by changing the reaction conditions, where shorter chain carboxylic acids yield larger NCs. The reactions can be executed under air and with solid loadings as high as 50 g/L. Importantly, the absence of a protective atmosphere during synthesis does not compromise the quality of the end product. In the case of CdSe, the surface chemistry of the NCs is identical to what has been reported in the literature, and they can be used as cores to grow CdSe/CdS core/shell NCs with photoluminescence quantum yields exceeding 40%. We argue that the combination of a fast and tunable, high yield reaction with atmospheric conditions and high solid loadings make the approach highly suited for the low cost, high volume production of colloidal metal selenide NCs. This conclusion is stressed by demonstrating the reproducible synthesis of CdSe NCs using the heterogeneous precursor by an automated liquid handler.

This method was transferred to the synthesis of binary, ternary and quaternary NCs suitable for the preparation of CZTS(e) layers for photovoltaic applications, showing the versatility of this method. However, due to the need for stable and Zn rich NCs, to obtain the p-type characteristics preferable for CZTS(e) solar cells, not all NCs are useful for the CZTS(e) layer formation. A first viable option to obtain the CZTS thin film absorber layers are the quaternary CZTS NCs. These NCs are tunable, the yield is high and show the desired crystal structure. Furthermore, the solid loading of the synthesis is as high as 50 g of NCs for 1 liter of solvent, almost double compared to literature. CZTSe, on the other hand, seems less viable since these NCs are Zn poor. Combinations of binary and ternary NCs is preferably formed using CuSnS - ZnS or CuSnSe - ZnS. The syntheses of these NCs have a high yield and are easily optimized. The Cu:Sn ratio can be set at 2:1 and the Zn can be tuned as desired since the Zn is introduced through the addition of separate NCs that can be added in a desired amount, in contrast to CZTSe NCs. A combination of the binary NCs SnS - CuS - ZnS could be possible, only if the SnS is optimized and higher yields of stable SnS could be obtained. Other combinations have downsides from a synthesis point of view and are not optimal to achieve the right stoichiometry.

12.2.2 Nanocrystal Inks

In order to realize the cost reduction promised by solution based processing, an applicable ink containing the synthesized nanocrystals should be formed. This means that the ink must comprise the elements needed in the final film under a form that enables smooth and crack-free nanocrystal films to be deposited. As we showed, this requires a colloidally stable dispersion of the synthesized NCs. In this respect, we used the fact that the synthetic approach chosen yields sterically stabilized nanocrystals to our advantage. We studied the effect of the original steric stabilizer (OLA) and were able to exchange the steric stabilizers for shorter chained ligands and charge stabilizing sulfide anions. We could identify and study the effects of the exchange using ^{1}H-NMR and link the results towards ink stability and flocculation. We showed that CZTS NCs gradually evolve towards an equilibrium situation between the ligands on the NCs and the OLA ligands in the solvent. Ligand loss on the surface can lead to destabilization and flocculation of the ink. Further research showed that a coordinating solvent (octanethiol) can solve this long term stability problem. Finally, carbon-free inks were created by replacing the organic ligands on the NC surface with sulfide anions, leading to a stable but clustered ink of sulfide stabilized CZTS.

So, three different inks were suitable for layer formation: OLA, octanethiol and carbon-free based NC inks. Upon drop casting, OLA based inks readily formed 1.5 μm thick films in a single deposition step, in which drying and heat treatment posed no problem. We had to take into account that OLA forms a dynamic equilibrium with the solvent, meaning that the ink must contain a large excess of OLA to ensure long term stability or it must be deposited quickly after a purification step (removing the excess OLA). Using an ink with excess OLA caused small cracks and craters in the surface due to the removal of the large amount of OLA upon heat treatment. In addition, we found that the final layer contained nearly 20% of carbon, which can be seen as an undesired contamination. When removing the excess of OLA, but leaving the nanocrystals with at least 80% of their capping, crack-free single deposited layers can be formed. This is higher than the theoretical maximum of 400 nm for 25 nm NCs, which is probably due to the OLA ligands acting as a binder and thus reducing the stress in the film. However, the final film still contained up to 7.5% of carbon. If octanethiol was used as a coordinating solvent a layer of 1.5 μm could be deposited in first instance. However, when removing the thiol by heating above its boiling point, which increases the normal stress on the film, cracks formed in the deposited layer that even peels off the substrate. This could be circumvented by multilayer deposition of 300-400 nm thin films via inkjet printing. Intermediate removal of excess thiol via a heat treatment was required to prevent redispersion in the next deposited layer. So, again crack-free layers of 1.5 μm could be produced. The use of carbon-free stabilized inks did not involve any binder in the dispersion, yet due to the nature of the exchange, the inks formed

contained nanocrystal clusters of up to 600 nm in diameter rather than individual nanocrystals. These clusters still made possible the deposition of 1.5 μm thick layers in one deposition. When dried carefully a crack-free and carbon-free layer could thus be deposited although the layer appears more porous, containing small voids compared to the inks stabilized by organic ligands. So, the three different inks were found suitable for depositing a film of 1.5 μm. We were also able to apply our formulation and deposition methods towards the CTS + ZS NC system, indicating that the gained knowledge on ink formulation and film deposition can be transferred to other NC systems.

12.2.3 Film Transformation

To obtain a suitable CZTS(e) solar cell, the fabricated NC films were thermally annealed to induce densification in the film via grain growth to avoid excessive recombination and carrier scattering from the boundaries between the nanocrystals. Since the nanocrystals already contained the right stoichiometry, a thermal annealing process could be enough to form a dense CZTS(e) film. We treated a CZTSe carbon-free nanocrystal layer up to 450 °C and found that crystal growth improved using forming gas instead of an inert atmosphere. This was explained by the reduction of surface sulfoxides, which resulted from exposure of the nanocrystal film to air or the decomposition of residual solvent during annealing. Nevertheless, also under a reducing atmosphere, the layers remained nanocrystalline with multiple grain-boundaries. Therefore, we switched to thermal annealing under a sulfur of selenium-rich atmosphere (sulfurization and selenization). When performing selenization and sulfurization of CZTS NC layers, we discovered that the presence of carbon induces crystal growth, yet this transformation also resulted in a double layered structure with large sized stoichiometric CZTS(e) on top and a carbon containing granular layer below. Although largely similar, the sintering effects differed in their details depending on the organic ligand used. OLA based layers exhibited a rough top layer, probably since the volume reduction during the densification process was larger as compared to thiol based layers for which the surface remained smooth. This effect was translated in a better cell efficiency for the thiol based cells (2.3%) compared to the OLA based cells (1.5%). Carbon-free CZTS layers retained their nanocrystalline character after selenization or sulfurization and showed no conversion efficiency.

Since carbon-free CZTS did not shown grain growth, we annealed a composite nanocrystal layer containing copper tin sulfide and zinc sulfide nanocrystals as an alternative. CZTS has a lower free energy of formation compared to these composites, which implies that the combination should thermodynamically favor the formation of CZTS. The carbon-free CTS NCs showed the formation of large Cu_2SnS_3 crystals with a diameter larger than 2 μm upon sulfurization and sel-

enization. Thus we combined C-free CTS with C-free ZS to form a stoichiometric NC layer. When sulfurizing the layer, CZTS was formed throughout the layer, but grain growth still was limited as from 12 nm to 38 nm according to XRD. On SEM the grained structure clearly disappeared, however a large grained structure did not arise.
Selenization of the by literature preferred Zn-rich Cu-poor composition resulted in a limited grain growth leading to small crystals and the formation of a granular Zn-rich residue. Selenization on a stoichiometric layer on the other hand showed optimal grain growth. However for the stoichiometric layer the starting layer was slightly porous, which resulted in cracking after densification due to volume reduction, making it impossible to fabricate a working solar cell.

12.3 Future Prospects

12.3.1 Economical Feasibility Of Nanocrystal Synthesis

A first question that comes to mind regarding the future and possible applications of this work is whether NC synthesis on a large scale is economical feasible and if upscaling is achievable. The synthesis method we developed for Se NCs in general has the advantage of using cheap synthesis conditions (atmospheric conditions), and is applicable using cheap synthesis precursors. We have shown that we have the highest solid loading in or synthesis (mg NC/L solvent) compared to available syntheses in literature and a high conversion yield. Combining these facts with the reproducibility of the synthesis, demonstrated using an automated liquid handler, and the high quality of the final product obtained, it appears that the developed approach is ideal for upscaling. The exact method of upscaling will depend on the application that requires the NCs.

Preferably for industial production a flow reaction synthesis is designed. However, upscaling for luminescent quantum dots or applications in which the size of the nanocrystals plays an important role, batch to batch reactions are still preferred. The use of batch to batch reactions allows us to synthesize NC with a predefined size and a relatively narrow size distribution within each bath and also allows the production of different sizes within one production setup. Particles with a monodisperse size (up to 10% in size distribution) can subsequently be purified and processed. Increasing synthesis volume and the effect on the quality is one of the parameters that should be explored, as is their use in large scale applications.

But whenever the synthesis on NC would require higher throughput and thus larger amounts of NC for applications. A flow production van have a significant advantage over batch to batch reactions. Flow reactions require less downtime, are more cost efficient on full scale productions. However, a flow reactor is mostly

limited towards a single output product. For instance in thin film solar cells, in which the final size of the particles has less importance, but high throughput can be important, flow reaction modules have been discussed in literature [1]. They can provide an alternative for the batch to batch based hot injection synthesis as discussed in this work.

12.3.2 Processability of Nanocrystals

In this work we have shown that NC can be processed to form thin films from wet deposition techniques. Numerous applications demand high quality inks (stable and few contaminants) to be processed into dense and crack-free thin films [2]. In first instance, the knowledge gained on the NC surface chemistry and its relation to ink stability and layer contamination can be transferred towards similar NC dispersions. When starting from our developed synthesis we have the advantage that the NCs already form a stable dispersion, a basis for a processable ink. To develop an effective ink the principle of ligand exchange can be used in different situations to fabricate a desired ink. Of course the desired ink will depend on the applications.

When a dense film of approximately 2 μm needs to be developed which can contain organics but need a dense structure, the use of OLA as a surface ligand and the use of dodecane as a solvent has proven to be a successful ink formulation for CZTS particles. However, for the fabrication of dense carbon-poor films and the formulation of a long term stable ink, the use of thiol based inks has proven to give an edge. The only disadvantage being that for films thicker then 500 nm a multilayer deposition approach is required.

In a broader perspective we can transfer the gained knowledge on the fabrication of thin films for sterically stabilized NC using short chained molecules such as oleic acid or stearic acid using NCs up to 25 nm. This allows QD films to be deposited using ink jet deposition and replace the use of multilayer spin coating [3], which could reduce fabrication cost and fasten the process due to large scale applicability.

We have also shown that using a ligand exchange towards carbon-free stabilization allows us to deposit a NC thin film containing very few contaminants. However the formation of a thin film resulted in a porous structure, which cracked upon densification. The processing of carbon-free inks could therefore require other deposition techniques such as spray coating to form a denser thin films. An other possibility could be the ligand removal upon a deposited film.

12.3.3 Towards Absorber Layers for Thin Film Photovoltaics

Even if the fabricated solar cells lack the efficiency to be economically viable, promising results in terms of phase transformation and densification have been shown. We can first conclude that for the use of inks stabilized by organic ligands, we typically obtain a 500 nm thick dense top layer after selenization or sulfurization. Possible applications could be the fabrication of transparent solar cells in which case a 500 nm thick CZTS would suffice to generate low power devices. An other possibility could be multilayer deposition and stepwise annealing of a thiol based film. Therefore every 500 nm deposited film is immediately annealed up to 3 times to form a 1.5 μm thick film. This could result in a film containing solely large crystallites and a better conversion efficiency. A second promising factor is the use of C-free CTS as a fluxing agent. We have shown that the use of C-free CTS and C-free ZnS in a stoichiometric combination leads towards a clear densification in the film. However the success of densification lead to a cracked film. If in the processing step we would be able to deposit a dense C-free film, in which the volume reduction upon densification is limited, a large grained CZTS layer could be fabricated.

References

[1] A. Shavel, D. Cadavid, M. Ibanez, A. Carrete, and A. Cabot, "Continuous production of cu2znsns4 nanocrystals in a flow reactor," *Journal of the American Chemical Society*, vol. 134, no. 3, pp. 1438–1441, 2012.

[2] D. V. Talapin, J.-S. Lee, M. V. Kovalenko, and E. V. Shevchenko, "Prospects of colloidal nanocrystals for electronic and optoelectronic applications," *Chemical reviews*, vol. 110, no. 1, pp. 389–458, 2009.

[3] S. Coe-Sullivan, J. S. Steckel, L. Kim, M. G. Bawendi, and V. Bulovic, "Method for fabrication of saturated rgb quantum dot light-emitting devices," in *Integrated Optoelectronic Devices 2005*, pp. 108–115, International Society for Optics and Photonics, 2005.